VNIVERSIDAD NACIONAL AVTPNOMA DE MEXICO

UNIVERSIDAD NACIONAL AUTÓNOMA DE MÉXICO

PROGRAMA DE MAESTRÍA Y DOCTORADO EN INGENIERÍA

FACULTAD DE INGENIERÍA

RESPUESTA AL DESBALANCE Y ESTABILIDAD DE UN ROTOR FLEXIBLE EQUIPADO CON UN DISPOSITIVO DE AUTOBALANCE TIPO LEBLANC

T E S I S

QUE PARA OPTAR POR EL GRADO DE:

DOCTOR EN INGENIERÍA

ING. MECÁNICA – DISEÑO MECÁNICO

P R E S E N T A :

LEONARDO URBIOLA SOTO

TUTOR:

DR. MARCELO LÓPEZ PARRA

2011

JURADO ASIGNADO:

Presidente:	Dr. Víctor Javier González Villela
Secretario:	Dr. Alberto Caballero Ruiz
1er Vocal:	Dr. Marcelo López Parra
2do vocal:	Dr. Alejandro Ramírez Reivich
3er vocal:	Dr. Francisco Cuenca Jiménez

Posgrado de Ingeniería, Ciudad Universitaria, México D.F.

TUTOR DE TESIS:

Dr. Marcelo López Parra

_____

FIRMA

Thoughts…

Para mirar, hay que ver dos veces
Para apreciar el detalle, hay que aprender a mirar

If you are to innovate, challenge and tear down the
current paradigms, and then create new ones

"UNBALANCE RESPONSE AND STABILITY OF A FLEXIBLE ROTOR EQUIPPED WITH A LEBLANC SELF-BALANCING DEVICE"

A Dissertation

by

LEONARDO URBIOLA SOTO

Submitted to the Office of Graduate Studies of the Faculty of Engineering at
Universidad Nacional Autonoma de Mexico
in partial fulfillment of the requirements for the degree of

DOCTOR OF ENGINEERING

October, 2011

Major Subject: Mechanical Engineering
Field: Mechanical Design

UNBALANCE RESPONSE AND STABILITY OF A FLEXIBLE ROTOR EQUIPPED WITH A LEBLANC SELF-BALANCING DEVICE

A Dissertation

by

LEONARDO URBIOLA SOTO

Submitted to the Office of Graduate Studies of the Faculty of Engineering at
Universidad Nacional Autonoma de Mexico
in partial fulfillment of the requirements for the degree of

DOCTOR OF ENGINEERING

Approved as to style and content by:

Chair of Committee,	Dr. Victor Javier Gonzalez-Villela
Committee Members,	Dr. Alberto Caballero-Ruiz
	Dr. Marcelo Lopez-Parra
	Dr. Francisco Cuenca-Jimenez
Graduate Studies Coordinator,	Dr. Alejandro Ramirez-Reivich

October, 2011

Major Subject: Mechanical Engineering
Field: Mechanical Design

RESUMEN

Respuesta al Desbalance y Estabilidad de un Rotor Flexible Equipado con un Dispositivo de Autobalance tipo LeBlanc (Octubre 2011)

Aunque el aro de balance de líquido fue introducido casi una centuria atrás por el inventor Francés Maurice LeBlanc, existe poca información disponible acerca del desempeño dinámico de éste tipo de dispositivo. En esta tesis se investigan cuatro tópicos principales; (1) la respuesta al desbalance, (2) las características de estabilidad, (3) la curvatura de las aletas para modificar la interacción fluido-sólido y mejorar el desempeño dinámico, y (4) un sistema híbrido de balance en dos planos para reducción de las fuerzas dinámicas del rotor, momentos y esfuerzos en los soportes de una lavadora de eje vertical. Los resultados experimentales indican que la interacción fluido-sólido arroja modos de vibración del fluido de tipo circunferencial y axial. Este complejo flujo tipo hélice se compone de dos olas inerciales una de las cuales es síncrona con el movimiento de cuerpo rígido, mientras que la otra es una ola de fluido que viaja en sentido opuesto, mejorando así la capacidad de amortiguamiento del sistema. Se introduce un modelo analítico de la respuesta al desbalance, el cual se correlaciona con

visualización de flujo y mediciones de vibración. Se muestra que un rotor flexible que emplea un balanceador tipo LeBlanc experimenta un considerable aumento en su umbral de estabilidad para un acoplamiento cruzado tipo aerodinámico y fricción interna del rotor. Se realiza experimentación más extensa en un aro de balance variando la cantidad de aletas y también la curvatura de las mismas. Posteriormente, se derivan y resuelven las ecuaciones de movimiento para una partícula de fluido para arribar a una curvatura óptima. Este novedoso diseño permite al rotor de la lavadora alcanzar altas velocidades para reducir el tiempo de secado al incrementar la fuerza centrífuga aplicada. Finalmente, además del aro de balance de líquido convencional colocado en la parte superior de la canasta, se adecua un aro de balance de bolas en la parte inferior de ésta, tal que se obtiene un sistema de balance en dos planos por la combinación de ambos tipos de dispositivos. Las ventajas de incluir un segundo aro de balance son principalmente, el mínimo espacio axial requerido para alojarlo en el fondo de la canasta, efectividad vs costo y buen desempeño dinámico por la reducción de las fuerzas de desbalance, momentos y esfuerzos en los soportes presentes en el sistema dinámico.

ABSTRACT

Unbalance Response and Stability of a Flexible Rotor Equipped with a LeBlanc Self-Balancing Device (October 2011)

Although the liquid balancer has nearly a century of having been introduced by the French inventor Maurice LeBlanc, little information is available on the dynamic performance of this kind of device. Four main topics are investigated in this dissertation; (1) the unbalance response, (2) the stability characteristics, (3) the baffles curvature to modify the fluid-solid interaction and improve the dynamic performance, and (4) a hybrid two-plane balancing system for reduction of rotor dynamic forces, moments and support stresses in a vertical-axis washing machine. Experimental results indicate that the baffle-liquid interaction renders fluid modes of vibration of circumferential and axial type. This complex swirl flow is comprised of two inertial waves; one of such waves is synchronous with the rigid body motion, while the other is a fluid backward traveling wave, thus enhancing the system damping capability. An analytical dynamic model of the unbalanced response is derived and correlated with fluid flow visualization experiments and vibration measurements. It is shown that a flexible rotor employing a

LeBlanc balancer has remarkable increase in the threshold speed of instability for aerodynamic cross-coupling and rotor internal friction damping. Further experiments are performed on a balance ring for washing machines varying the amount of baffles and also with curved baffles or “blades” to modify the fluid-solid interaction. Dynamic equations of motion for a fluid particle are introduced and solved to arrive to and optimum curvature. This novel design enables the washing machine drum to run at higher speeds, and reducing the centrifugal cycle while increasing the centrifugal force applied to the objects being washed. Finally, besides the conventional liquid balance ring placed on top of the rotating basket, a ball-balance ring was fitted to the lower part of such basket, such that a two-plane balancing is achieved by the combination of both types of devices. The advantages of including a second lower balance ring are mainly, the minimum space required to house it into the basket bottom, cost-effectiveness, and good dynamic performance achieved by reducing the unbalance forces, moments, and support stresses present on the rotating system.

DISCLAIMER

This dissertation is written in the English language for convenience to the author, and in agreement with the advisory committee. The aforesaid because the products of this research, namely; technical papers and patents, have been originally written in English and submitted to ASME[1] Conferences, ASME Journal of Vibration and Acoustics, Journal of Shock and Vibration, and the United States Patent Office with due proof review. Although every effort has been made in writing well this thesis, the author is not a native English speaker, therefore he apologizes for any typographical errors, misspellings, incorrect phrasings, or just plain wrong use of the English language. The author also believes that in writing this thesis in English, it will also be worldwide more accessible and helpful in disseminating its contents.

[1] American Society of Mechanical Engineers.

DEDICATION

To my beloved Rosalba,

soul-mate, girlfriend, lover and wife,

who supported me in all possible ways to accomplish this project,

and always kept the home fires burning,

while I was immersed in science, machines, and technology.

Rose:

You are the loveliest thing that ever happened in my life,

Your existence in this world is my prize,

You make a lovely place wherever you are,

In my eyes you are a star

You make home…

The best is yet to come…

always

ACKNOWLEDGEMENTS

My first and foremost acknowledgement in completing this intellectually challenging project that culminated in my Doctorate dissertation goes to my friend and advisor Dr. Marcelo Lopez-Parra. I am grateful to him for believing I was up to the task, and guide me throughout my three years as UNAM graduate student. Along the way, his warm personality provided me unconditional technical and moral support, and for that, I will always be thankful. My sincere appreciation is for my committee members; Drs. Alejandro Ramirez-Reivich, Victor Javier Gonzalez-Villela, Francisco Cuenca-Jimenez, and Alberto Caballero-Ruiz, for their encouragement and continuous interest in my research work. Their review definitely contributed to make my work of better quality.

Many thanks to mabe Company for granting permission for the publication of this work. In this thesis, figures showing Computer Aided Design (CAD) 3D models are mabe proprietary information, therefore captioned as "courtesy of *mabe S.A. de C.V.*". Thank you also to Universidad Nacional Autonoma de Mexico (UNAM) and Consejo Nacional de Ciencia y Tecnologia (Proyecto SEP-CONACYT-Ciencia Basica No.

83239) for granting the financial support that allowed me to present portions of this investigation abroad in the format of technical papers at Conferences of the American Society of Mechanical Engineers (ASME). Thanks to Martin Ortega, Donato Reyes, Shair Mendoza, Alfonso Thompson, and Claudio Zenteno, engineers at mabe, for their help in conducting the measurements and recording the digital movies as part of the technology development strategy of the Dynamics Group under my direction from 2005 to 2008. In this doctoral thesis, I am filling the theoretical blanks left on the way during the work we developed together. This is an effort to explain the things we could not understand in those years, first because of the lack of theoretical background on the subject, and second because the day-to-day rush to meet projects deadlines. I am indebted to Hugo Velasco (mabe's intelectutal property attorney), and Victor Gonzalez (Manager of Clothe's Care Technology), for reviewing, approving, and releasing my dissertation. My appreciation goes to Victor for hiring me six years back to begin the understanding of the mabe washer dynamics. He trusted me in accomplishing the technical challenges imposed by the washing machine vibration and acoustics. Thank you very much to Salvador Cossio (former Manager of Dryers Technology, now Manager of Ranges Technology), who was my boss over two thirds of the time I was

pursuing my PhD. I enjoyed a big deal the time working with him while I was Leader of New Technology Introduction for dryers. I learned from Salvador “Chava” how to define, focus, execute, and implement down-to-earth useful and meaningful research and development projects. Chava is probably the best boss I have ever had. He was very kind and supportive in granting me the necessary days-off to attend to the doctoral examinations at Ciudad Universitaria of UNAM, and allowed me the time as needed for fulfillment of the requirements for the degree. Thank you also to Drs. Carlos Perez-Lopez and Bernardino Barrientos-Garcia at CIO for helping with technical insight and discussions in the high-speed camera and Particle Image Velocimetry (PIV) experiments. My gratitude goes to my friends at mabe, Dario Martinez-Ramirez, Pablo Soto, Giancarlo Paez, Manuel Martinez Pineda and Carlos Galindo for their encouragement. I want to especially thank Dario, for helping me tremendously along the way in my doctorate. I do not have enough words to thank my dear friend Dario for his selfless help. Last, but not least, many thanks to my wife for being the companion of my life, she patiently supported all the privations we had to endure during my Ph.D. studies. This is the accomplishment of both of us, who are one.

I am thankful to all of you.

NOMENCLATURE

ω	Frequency rate, rad/s
m,n	Circumferential and lateral modes of vibration
x,y	Cartesian coordinates, m
F	Force, N
a	Rotor mean orbit radius or eccentricity, m
v	Balance ring volume, m^3
$\mathbf{z} = x + jy$	Complex rotor motion or eccentricity, m
$\mathbf{z_1} = x_1 + jy_1$	Complex tub and complex journal whirling motion, m
ϕ	Angular coordinate, rad
β	Unbalance response phase angle, rad
c	Damping, N·s/m
$d = z\, r_f^2 /(r_o^2 - r_f^2)$	Distance from **C** to **F**, m
k	Stiffness, N/m
h	Balance ring height, m
$f = \omega/\omega_{cr}$	Frequency ratio, dimensionless

$j = \sqrt{-1}$	Imaginary unit, dimensionless
m	Mass, kg
r	radius, m
t	Fluid film thickness, m
x,y	Cartesian coordinates, m
$\bar{z} = z\, r_o^2 /(r_o^2 - r_f^2)$	Distance from **O** to **F**, m
C	Disc center
F	Fluid center of gravity
M	Disc center of gravity
O	Bearing center
$q = c_i \omega$	Aerodynamic cross-coupling coefficient, N/m
$K = k_1/k_r$	Stiffness ratio, dimensionless
$M = m_f/m_r$	Total fluid mass ratio, dimensionless
$M_b = m_b/m_r$	Backward traveling wave mass ratio, dimensionless
β	Unbalance response phase angle, rad
$\xi = c/2\, m_r \omega_{cr}$	Damping ratio, dimensionless
ρ	Fluid density kg/ m^3

r,θ	Polar rotating coordinate system, m, rad
R,Θ	Polar fixed coordinate system, m, rad
L	Trajectory, dimensionless
N	Normal Force, N
P	Point particle
t	Time, s
v	Velocity, m/s or rad/s
a	Acceleration, m/s^2 or rad/s^2

Subscripts

1	Bearing property
b	Fluid traveling backwards property
cr	Rotor critical speed on rigid supports, rad/s
d	Whirl frequency, rad/s
e	Effective property
f	Fluid property
i	Rotor internal property
i	Inner

m	Maximum value
o	Outer
op	Optimum value
r	Rotor property
s	Straight line
a	Angular or spiral curve
t	Tub property
u	Unbalance property
unif	Uniform

TABLE OF CONTENTS

LIST OF FIGURES

LIST OF TABLES

CHAPTER I

INTRODUCTION[2]

Strategy for Literature review

There are three important components for achieving a washing machine design with good dynamic performance, namely; the suspension, the autobalancing devices, and the cabinet structure. Depending on the passive mechanism employed, the autobalancing devices can be classified into the liquid and ball-balance ring type. The balance ring vastly used in modern automatic washing machines is of LeBlanc type [1]. It basically consists on a hollow ring equipped with a number of pockets formed by radial baffle boards and partially filled with liquid, mainly a brine solution. The radial baffle boards are equiangularly spaced within the cavity. With regard to their location on the drum rotor, also called rotating basket, the autobalancing also known as self-balancing devices can be divided into top balance ring, if it is placed on the upper part of the basket and bottom balance ring, when situated on the lower part of the basket. Liquid may be in the interior of a rotor by design, as in the case of centrifuges, certain blade cooling systems, or in balance ring devices employed in washing machines. Also, liquids can be contained in rotating bodies by accident, as in the case of restarting turbines with trapped condensate inside. As strategy, the literature review will be divided into three main areas of research: (1) liquid balance rings employed for controlling the vibration of washing machines, (2) internal rotor friction damping and trapped fluids in hollow rotors, and (3) ball-balance ring devices for washing machines.

---

[2] This thesis follows the style and format of *ASME Journal of Vibration and Acoustics*.

Liquid Balance Rings

The limited information on the liquid balance ring made public can be found on a number of patents and a few technical papers and thesis work. Back in 1914, a French inventor named Maurice Leblanc [1] first introduced a passive dynamic balancing device for turbine rotors consisting of an annular cavity partially filled with mercury or a liquid of high viscosity as shown on Fig. 1. However, this kind of device has not received much attention for practical use in turbomachiney since then.

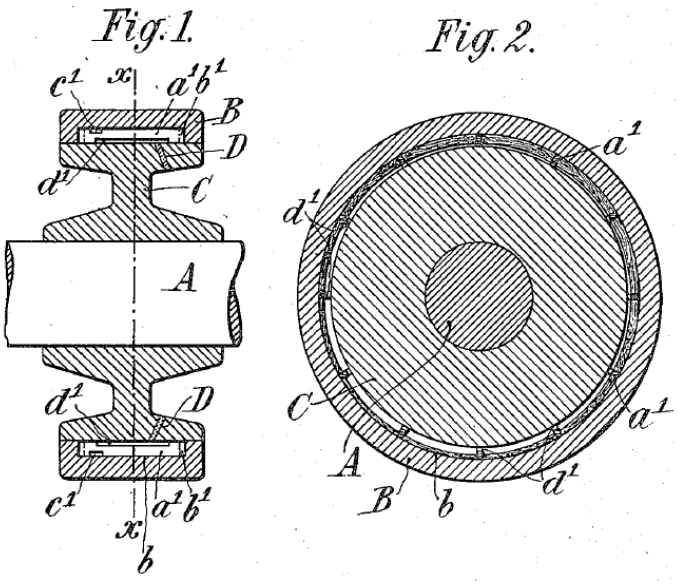

Figure 1. Automatic balancer for rotating bodies, from LeBlanc [1].

It is believed that the first balance ring device employing water and adapted into a washing machine, was introduced in 1945 as patented by Dyer [2]. Figure 2 shows the array suggested by Dyer with two balance rings placed on the bottom of the rotating basket.

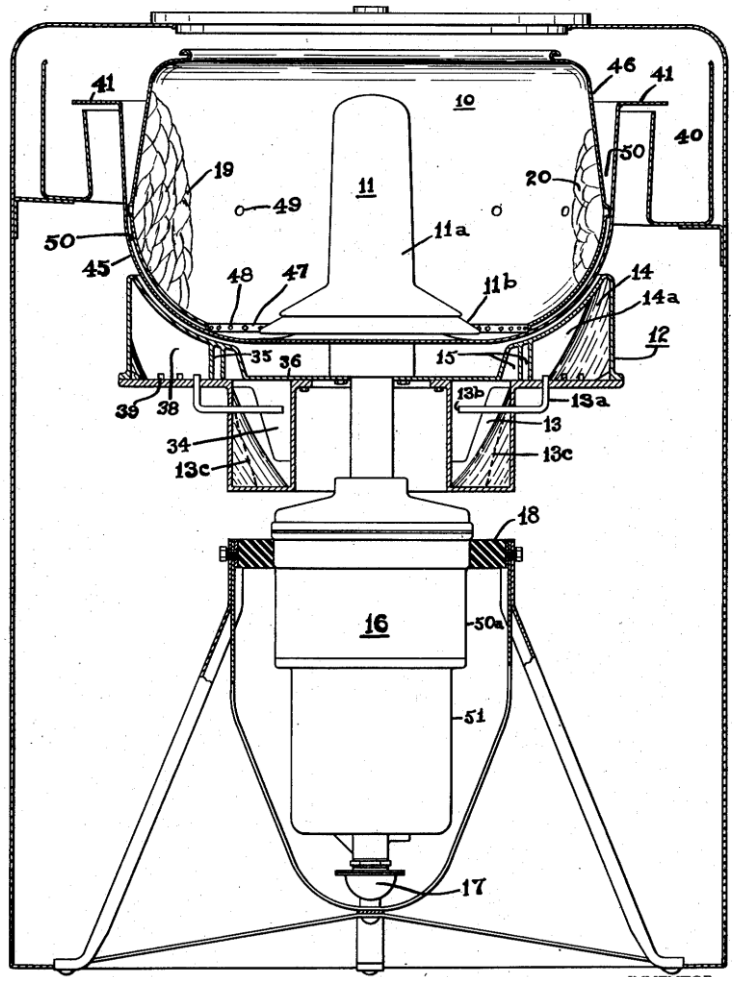

Figure 2. Liquid balance ring in a washing machine, from Dyer [2].

A plurality of nested separated and concentric rings was patented by De Remer [3] for most efficient balancing action. Vankirk and Burmeister in 1976 [4] present a balance ring which filled chambers on the peripheral of the washing machine with water during the spin cycle. In 1977, Hayashi *et al.* [5] explains means for feasible manufacturing of the balance ring made out of plastic halves welded by the use of hot plate technology. This is the modern version of this device as mounted on the top of the rotating basket of vertical-axis washing machines. Fig. 3 illustrates this concept.

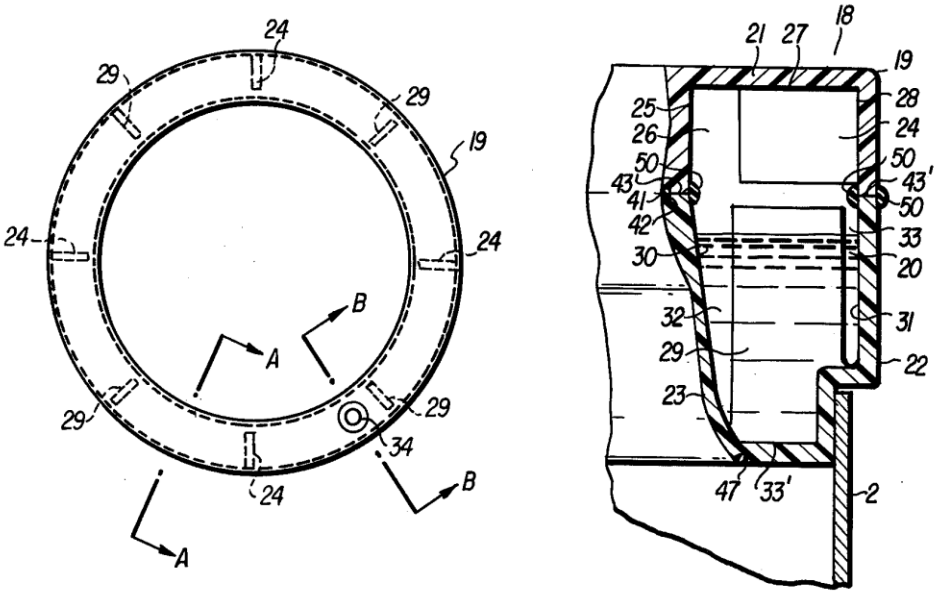

Figure 3. Modern liquid balance ring in a washing machine, from Hayashi [5].

Later, Conrad [6] analyzed a multichambered balance ring with successive concentric annular cavities to increase the balancing capability of fluid. Hoon *et al.* [7] developed a numerical model of the washing machine representing the liquid balancer as lumped masses. The lumped masses were linked to the center line of the spinning basket with revolute joints and rotational spring-dampers, which were deliberately tuned to correlate numerical data with experimental displacement measurements. Morio *et al.* [8] used Eq. (1) for the balance ring force:

$$F_f = \pi \; h \; \rho \; r_o^2 \; z \; \omega^2 \tag{1}$$

Where the guess value for *z* is obtained with a finite element model made using commercial software. The resulting force is analogous to a feedback control system. The model is then solved for frequency response. This equation overestimates the fluid balancing force in some important measure, this can be seen in Morio's experimental strain value for the rotating structures, which are consistently low compared to the finite element solution. Bae *et al.* [9], established the differential equations of motion of a modern vertical-axis washing machine. However, the whirling tub and the rotating basket were modeled as two rigid bodies with rigid connection, hence limiting the tub-basket relative motion. Bae *et al.* found the fluid center of mass by integrating the top view area covered by the liquid inside the cavity under a prescribed eccentric condition, and then he calculated the fluid force, which was validated with experimental measurements. This force was later input into his model to solve for the steady-state unbalance response. He arrived to a similar equation found previously by Conrad [6]. Urbiola [10] without having had access to Conrad's and Bae's work also reported the balance fluid force to be:

$$F_f = \left[fill \ \left(\mathrm{r}_o^2 - \mathrm{r}_i^2 \right) \ h \ \rho \right] \left(\frac{-z \ \mathrm{r}_f^2}{\mathrm{r}_f^2 - \mathrm{r}_o^2} \right) \omega^2 \tag{2}$$

Where the fluid inner surface radius is given by

$$r_f = \left[fill \ \left(r_i^2 - r_o^2 \right) + r_o^2 \right]^{0.5} \tag{3}$$

Jung *et al.* [11] proposes the installation of a middle plate accounting with a number of holes to avoid fluid sloshing. A Computational Fluid Dynamics (CFD) method was employed to verify its effectiveness. He used the balance ring force model from Bae [9]. Recently, Urbiola *et al.* [12] introduced the first balance ring design with non-straight baffles. Urbiola's design comprises alternatively disposed positive and negative curved blades, as well as positive curved and straight blades, that in combination with blades of different heights, reduce the time and the amplitude of the vibrations of the transient-state. Also, this novel design enables the drum to spin at higher spin velocities. The inconvenience of previous research efforts lies on the fact that the eccentricity in steady-state needs to be known a priori, usually by displacement measurements, subsequently the fluid force can be estimated and input into a dynamic model to predict the unbalance response at the rated speed. Predictions of the unbalance response across a frequency range are not reported until now. The assumed physical principle followed by this balancing device is that, an elastically mounted rotor will displace 180^{o} out of phase of the applied unbalance above its first critical speed. However, this is not necessarily true due to fluid damping effects.

A major disadvantage of liquid balancing devices is to add mass to the unbalance while operating below the first critical speed [6]. Hence, any system being considered for this type of balancing needs to have a relatively low resonant frequency. In the author's experience, for moderate unbalance load, this problem may be alleviated by inducing a fast ramp up as is the common practice of home appliance manufacturers.

The start-up ramps should specifically minimize the time required to pass through all resonances. Most washing machines have their first bouncing and rocking natural frequencies in the range from 200-250 rpm, while the fluid, as will be shown later, attaches to the outer wall at 150 rpm. Then, the fluid really does not have much opportunity to add considerable unbalance at low speeds. Actually, the natural frequency is traversed in the first 2 to 3 seconds, while the drum rotor barely completes 6 to 10 turns, so the machine is not allowed to dwell within the bandwidth of the system resonance. However, for large unbalance loads, the ramp up is often not enough to attain a smooth start-up and a fluid balance ring with better performance for the transient-state is desired to avoid tub-cabinet collision.

Internal rotor damping and trapped fluids in hollow rotors

There has been considerable work in the area of the dynamics of rotors with internal damping that is well-documented in the literature, particularly with regard to internal friction arising from micro-slip at shrink-fit interconnections of built-up rotors. Newkirk [13] pointed that internal rotor damping created by shrink fits of impellers and spacers is a predominant cause of whirl instability. Kimball [14] by means of deriving the equations of motion showed that the internal friction force tends to put the shaft motion in an ever-increasing spiral path. Gunter [15] developed a linear rotordynamic model in which internal friction was modeled as a cross-coupled force. He demonstrated that if external damping is added, the threshold speed could be greatly improved. He also showed that foundation asymmetry without foundation damping can cause a large

increase of the onset speed of instability. Black [16] investigated a variety of models (viscous, Coulomb and hysteretic) for internal friction and differentiated between various models in reference to their ability to accurately predict the onset of instability. Lund [17] also investigated internal friction models, specifically due to micro-slip at axial splines and shrink fit joints. Srinivasan [18] showed that at some values of low interference fit, the system became unstable at high speeds, while no instability was noted for tighter fits. Damping for the low interference fit was higher than for the high interference. The aforementioned is due to the fact that when the fit is tight, slipping at the interference between the disc and the shaft is reduced. In most cases, the whirl instability can be suppressed with hardware fixes such as changing the bearings to softer supports with asymmetric stiffness, adding more damping in the bearings or tightening the interference fits. This research work proposes an alternative mechanism for improving rotor stability by using a LeBlanc balancer in turbomachinery applications.

It has extensively been demonstrated that when a flexible rotor is partially filled with liquid, the motion is unstable over some operating range. The subject called first the attention in the instability problem caused by the trapped rotational fluid in hollow rotors, such phenomenon has been reported in a liquid-cooled gas turbine by Kollmann [19], a jet engine by Ehrich [20] and in a high-speed gear-type coupling by Kirk *et al*. [21]. The extent of this operating range depends on various system parameters such as rotor damping, stiffness, fluid viscosity, the amount of fluid present, etc. However, when the cavity of a hollow rotor filled with liquid is provided with a number of radial baffle

boards, such that it resembles a LeBlanc balancer, the unstable behavior changes dramatically. Thus, the LeBlanc Balancer may help the rotating system achieve higher stable operating speeds.

Ball-balance ring systems for washing machines

In 1932, Thearle [22] introduced a balancing device consisting of an annular track equipped with a couple of free rolling balls. This device was aimed to be located in the balancing plane of a statically unbalanced rotor. Similar to the fluid behavior of a liquid balance ring, the balls find equilibrium at an opposed location of the unbalance. A viscous fluid, usually some kind of lubricating oil, is employed to drag the balls and diminish the noise emitted by the rolling action of the balls within the track. The scientific literature on this kind of device is much more abundant than their liquid balancing devices counterpart, and the subjacent phenomena on its unbalance response and stability is well understood [23-27]. The uses of the ball-balancing device range from blood centrifuges, optical disc readers, and spindles of high precision machine tools, whereas, the application of the ball-balancing device for appliance products is yet very limited and only seen in the market on front load washing machines. One of the goals of the doctoral work is to introduce a combined balancing system that includes both, the liquid balancing and the ball-balancing devices. The literature review of the ball balancing device will therefore be focused on a patent search for vertical-axis washing machines. Tatsumi [28], in 1984, patented a vertical-axis washing machine accounting a ball-balancing device on top of the basket, see Fig. 4.

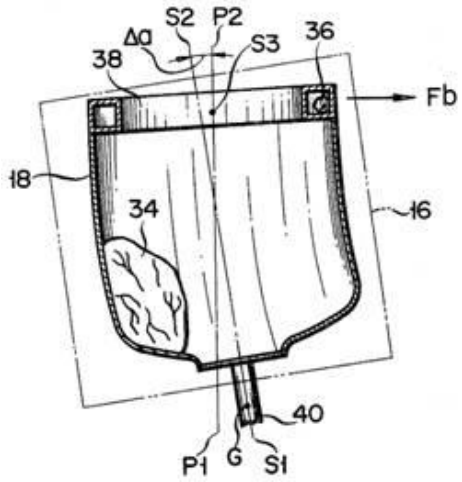

Figure 4. Vertical-axis washing machine with ball-balancer, from Tatsumi [28].

Tatsumi also details a very creative mechanism for controlling the balls random motion during the transient-state at the machine start-up. He claims a track with internal radial boards that hold in place the balls to avoid collision between them. As the speed increases, the centrifugal effect makes the balls climb on the sloped outer wall of the track to reach a window on the radial wall that connects to a free-circulatory annular cavity. This device is shown on Fig. 5.

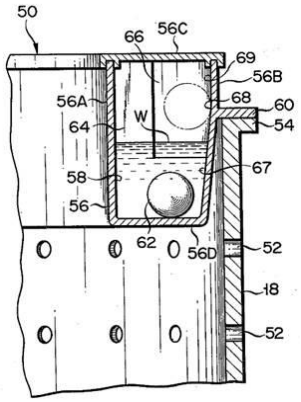

Figure 5. Ball-balance ring with radial boards and free-circulatory annular channel, from Tatsumi [28].

The Brazilian patent of Lee *et. al.* [29] claims the tandem array of a couple of balance ring devices placed on top of the rotating basket as shown on Fig. 6.

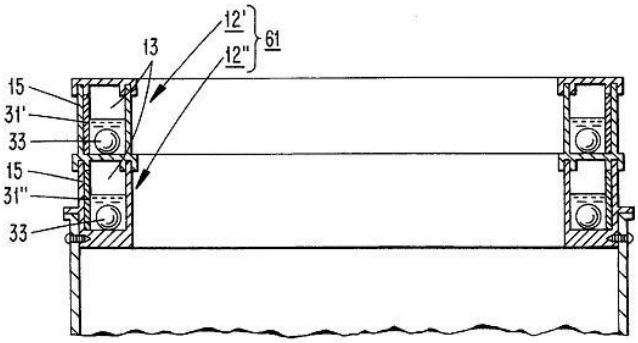

Figure 6. Tandem array of a ball-balance system on top of the basket, from Lee [29].

More recently Southworth [30], introduced a multiple balance ring array as shown on Fig. 7 for installation on the upper part of the basket. This concept consists on a balance ring with two annular cavities and comprised of three different mechanisms; (1) spheric balls of steel on the top cavity, (2) a high viscosity liquid that also provides balancing while dragging the balls superior, and (3) a low viscosity fluid contained in a lower cavity that resembles a liquid balance ring. On the front load horizontal-axis washing machine, Kim [31] was the first to claim the idea of using a couple of ball-balance rings, each of these mounted at the ends. He further introduces a tandem array of ball-balance rings also at both ends of the drum as depicted on Fig. 8.

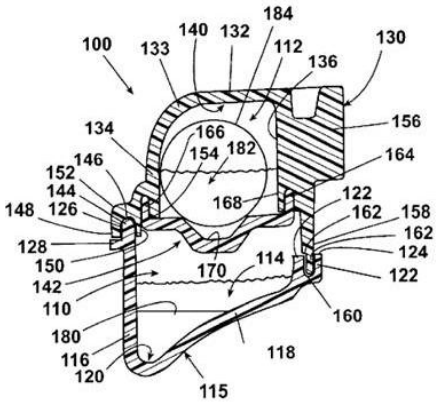

Figure 7. Multiple balance ring, from Southworth [30].

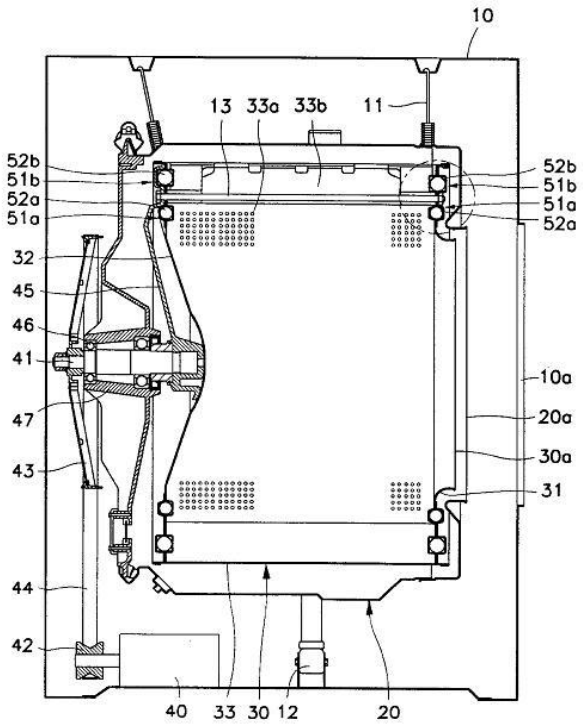

Figure 8. Ball-balance ring, from Kim [31].

Assessment of research needs

A summary of the literature review on the studied subjects, namely; liquid balance rings, trapped fluids in hollow rotors, and ball-balancers is presented in Table 1 as a literature mapping. Main topics pertaining to each subject as related to flexible rotors are color mapped in green to show where the research is abundant. In contrast, yellow areas help identify current research needs. As shown, there is pertinence of research in understanding the unbalance response, fluid-solid interaction to improve rotor stability, and more effective balancing mechanisms in flexible rotors from an

analytical approach. Although there is also a need for a numerical approach, it will not be pursued in this thesis.

Table 1. Literature mapping.

	Liquid balance rings			**Trapped fluids in hollow rotors**		**Ball-balancers**	
Reference	Experimental	Numerical	Analytical	Instability	Fluid-solid interaction	One plane	Two-Planes
1	■						
2	■						
3	■						
4	■						
5	■						
6	■		■				
7	■	■					
8	■	■					
9	■		■				
10			■				
11	■		■				
12	■						
13				■			
14				■			
15				■			
16				■			
17				■			
18				■			
19				■			
20				■			
21				■			
22	■						
23						■	
24						■	
25						■	
26						■	
27						■	
28						■	
29						■	
30						■	
31							■

CHAPTER II

OBJECTIVES AND METHODS

Dissertation objectives

As explained in the preceding paragraphs, the balance ring is placed on top of a rotating drum that contains a randomly distributed wet cloths load within, such that as the drum spins the fluid moves to the opposite side of the load acting as a passive self-balancing mechanism. A fairly well-designed balance ring gives a relatively smooth motion of the machine over a wide range of unbalanced loads and running speeds. However, little or no research has been published to understand the interactions of the fluid and baffles, the way the balancing mechanism takes place remains unclear. Furthermore, a mathematical model to understand the unbalance response and stability of this device is missing, such that an improved design can be achieved. Given the above, the main objectives of this research work are as follows:

1. To understand the fluid-solid interaction between the baffles and the liquid contained in the balance ring cavity.
2. To develop a mathematical model to predict the unbalanced response and vibration transmissibility across the frequency range for different liquid fill ratios and correlate with experiments.
3. To explain the stability enhancing capabilities of the LeBlanc balancer.

4. To arrive to and improved balance ring design by developing a dynamic model of the fluid-solid interaction and using it to redesign the balance ring.

Research methodology

The research is divided into experimental and theoretical studies. The methodology for the research in each of the two areas is described as follows:

Experimental study

A modern washing machine with balance ring is a complicated system. Rather than modeling the complete system, simplified models were developed for various components. Thus, several approaches were taken to gain a better understanding of the dynamics of a washing machine. The four main approaches were.

1. Individual components dynamic characterization to integrate adequate equations of motion. Components to characterize are suspension stiffness and damping, rotor stiffness, natural frequency and vibration due to unbalanced load.
2. Experimental work to observe the fluid waves in the balance ring and build fluid velocity maps. The test bench consisting of a washing machine provided with a transparent balance ring to enable using a high-speed camera for fluid flow visualization and Particle Image Velocimetry (PIV) for quantifying the fluid velocity map.

3. Further experiments varying the liquid-cavity fill ratio, amount of baffles and also with curved baffles or “blades” to modify the fluid-solid interaction and arrive to an improved design.
4. Combination of a ball-balance ring device on the bottom of the basket with the conventional liquid balance ring on top of the rotor to assess the impact on the rotor moments and support stresses.

Theoretical study

1. Introduction of a dynamic model of a flexible rotor equipped with a balance ring. This model to include 4 degrees of freedom (dof) of a washing machine, accounting suspension, rotor stiffness, unbalanced load and the fluid balance ring force, correlated with vibration measurements and examined for different balance ring liquid fill ratios.
2. Modify dynamic model by introducing rotor internal friction damping and aerodynamic cross-coupling to the model to prove the stability characteristics of a LeBlanc balancer. The stability improvements were explained using industrial turbomachinery rotors.
3. To develop dynamic equations of motion of a fluid particle and solve for optimum baffle curvature.
4. To establish a simplified static approach to explain de advantages of introducing an advanced two-plane hybrid balancing system in a vertical-axis washing machine.

CHAPTER III

EXPERIMENTAL TEST FACILITY

Test rig

The image on Fig. 9(a) represents a cut-away view of a modern vertical-axis washing machine, which comprises a tub that contains a washing basket, the later capped by a liquid balance ring. An unbalance mass is placed in the basket to simulate its unbalanced condition imposed by the garments being washed, since they do not settle uniformly on the bottom of the basket after the washing cycle has finished. Figure 9(b) shows the lower half of the balance ring with the molded baffles, and Fig. 9(c) illustrates a cross-section view of the balance ring assembly with the upper part commonly welded using hot-plate technology. Figure 10 shows a top view of a washing machine with a typical unbalanced load distribution within the basket. In order to dry efficiently the objects being washed, centrifugal movement at high angular velocities is required. However, as the velocity increases the excitation frequencies might create greater amplitude of vibration, which would cause knocking between the tub and the cabinet structure, either making the washing machine to "walk" or causing other subsequent damages to the machine and/or user annoyance due to vibration and noise. The washing unit is mounted on a rigid steel frame for performing the vibration experiments. The orthogonal components of the vibration were measured at the balance ring and tub using Banner LG® series laser short-range precision displacement transducers with a resolution of 10 μm, which are mounted on a surrounding nylamid structure as shown on Fig. 11(a). Suitable openings on the tub were practiced for direct measurement of the balance

ring vibration, as it can be seen in Fig. 11(b). A schematic of the coordinate system is shown on Fig. 11(c).

For the unbalance response experiments, the system was operated at a speed of 78.5 rad/s (750 rpm) by a variable frequency motor that could drive the rotor at any given acceleration rate or maintain any steady rotational speed up to 104.7 rad/s (1000 rpm). A different washing unit was used for fluid flow visualization and PIV experiments; such that the side view was clear for video recording, see Fig. 12. The balance ring employed mainly consists of an annular cavity of 3.709E–03 m^3 accounting a number of eight radial baffles equiangularly spaced.

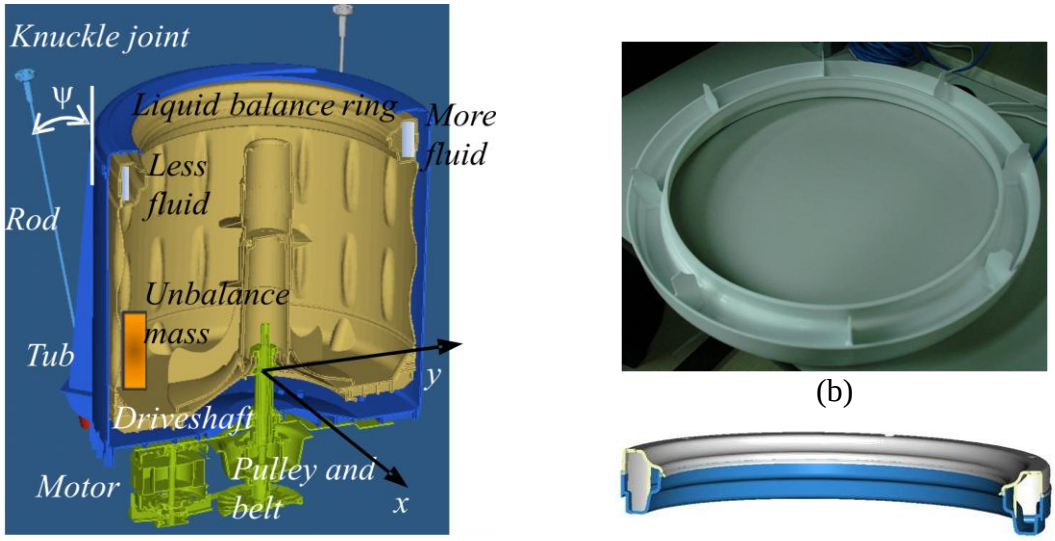

Figure 9. Washing machine; (a) cut-away view, (b) balance ring lower part with molded baffles, and (c) balance ring assembly cross-section view (courtesy of *mabe S.A. de C.V.*).

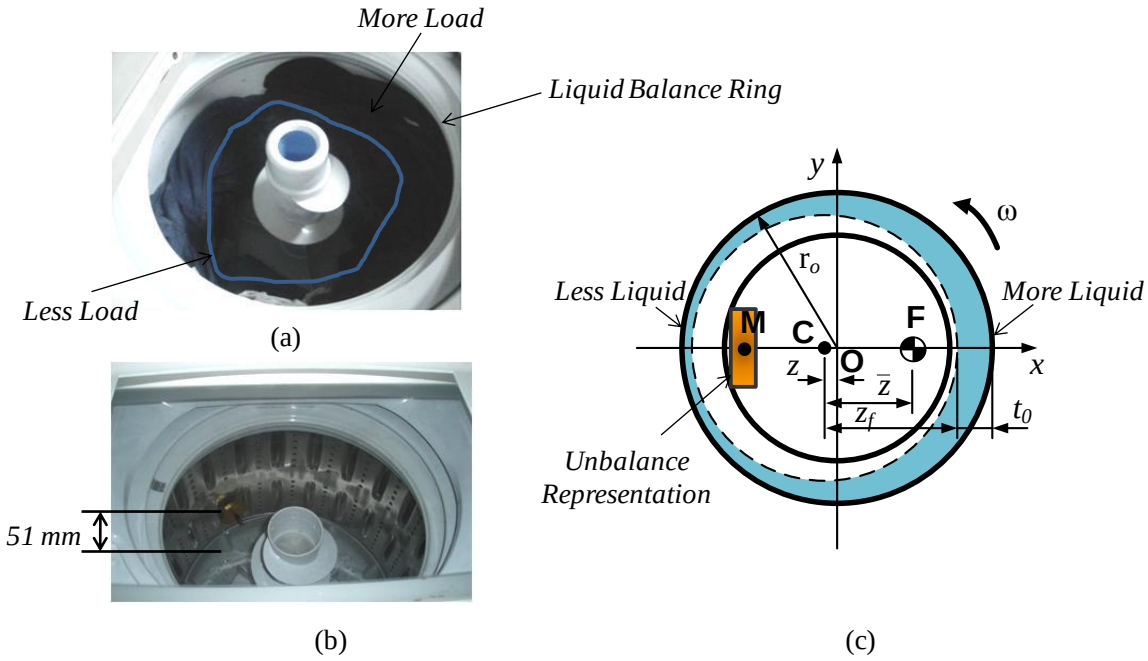

Figure 10. Washing machine top view; (a) Typical unbalanced load, (b) unbalance representation using a brass disc of 2.5lb placed at 51 mm from the basket bottom, and (c) assumed fluid distribution.

A benchmark study indicates that the liquid volume fraction of many washing machines balance ring approaches 50 to 80% of the total ring volume. During the experiments a fill ratio of 80% by sodium chloride with a density of 1300 kg/m^3 was employed. Figure 13 shows the balance ring under study consisting of a thermoformed Polyethylene Terephthalate (PET) ring assembled by two parts. The bottom part houses the baffles, which are put in place by being inserted in machined guiding grooves. The upper part works as a top cover bolted to the bottom portion. In between, there is an open cell gasket aimed to prevent fluid leakage. The balance ring assembly is rigidly mounted on top of the rotating basket through a set of brackets.

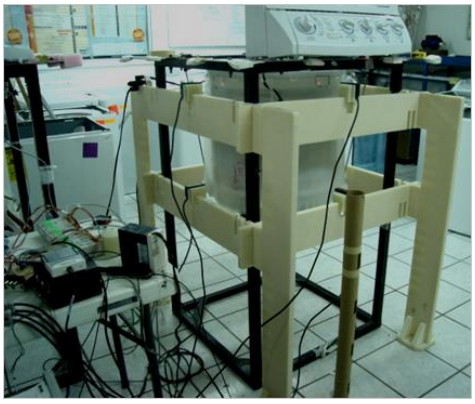

(a)

(b)

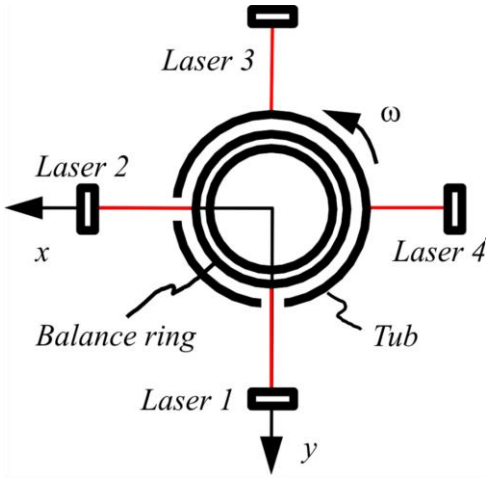

(c)

Figure 11. Vibration measurements; (a) rigid steel frame, (b) detail of laser displacement transducer, and (c) laser transducers coordinate system array.

Figure 12. Washing unit for fluid flow visualization and PIV experiments.

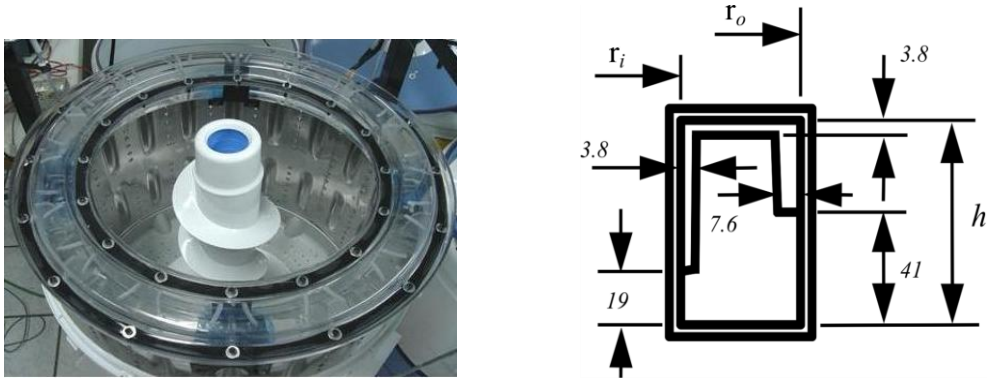

(a) (b)

Figure 13. Transparent balance ring; (a) top view, and (b) radial baffle, dimensions in mm.

Components dynamic characterization

Impact testing technique was used to measure natural frequency of rotor in the *x* and *y* directions with the following results. Figure 14 shows the experimental array.

- 1st natural frequency in the x axis (ω_{crx}) = 812 cpm
- 1st natural frequency in the y axis (ω_{cry}) = 979 cpm
- Average natural frequency (ω_{cr}) = 900 cpm

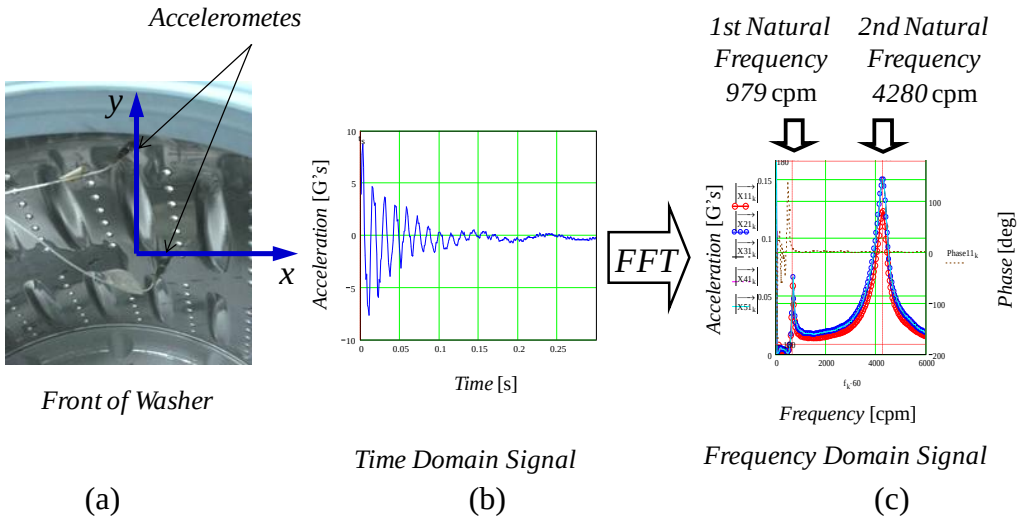

Figure 14. Measurement of natural frequency of rotor; (a) washer basket instrumented with accelerometers, (b) time domain signal, and (c) frequency domain signal.

Rotor stiffness (*k*) measurements were performed applying static loads through a dynamometer and recording the associated deflection indicated by a dial gage as illustrated on Fig. 15. Suspension coil spring stiffness (*rate*) measurements were done with the aim of a dynamometer test stand, see Fig. 16. Owing to the closely vertical orientation of the suspension, the only appreciable damping (c_1) in the *x*-*y* plane comes from grease lubricated knuckle joints at both ends of the supporting rods. The damping (c_1) was measured using the washing unit pendular motion and measuring the

logarithmic decrement response using a similar impact testing technique as in Fig. 14. The natural frequency (ω_n) of the system was determined following the same impact technique. A set of 15 experiments were made to determine all the aforementioned variables, Table 2 reports the average of each one. The angle (ψ) between rod suspension rod and the vertical was obtained using mabe's PRO-E® software databases. Finally the unbalance mass (m_u) was chosen as a representative amount of unbalance representing average uneven distribution of garments in the field according to manufacturer experience.

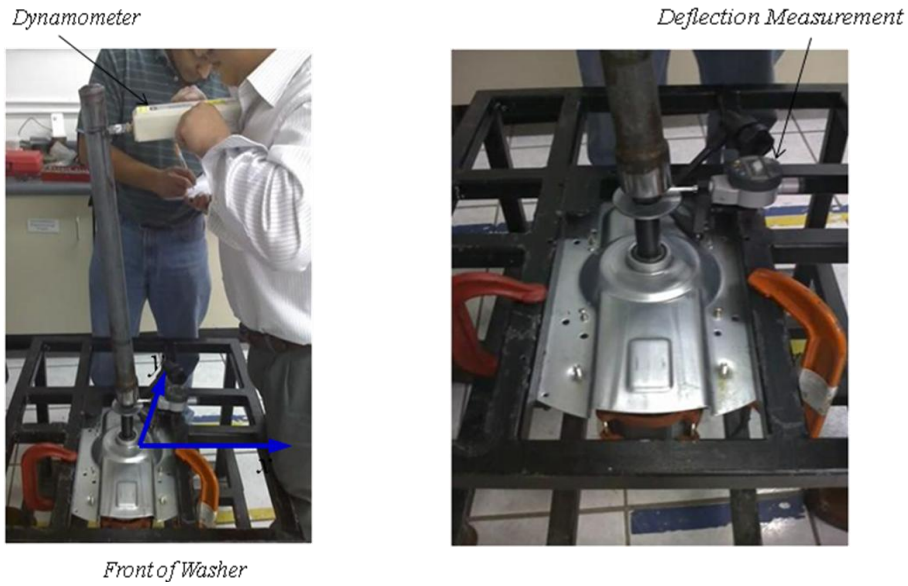

Figure 15. Rotor stiffness measurement; (a) applied force through a dynamometer, and (b) detail of dial gage.

Figure 16. Suspension coil spring stiffness measurement.

Table 2 reports the experimental parameters of the individual components dynamic characterization. An unbalance of 1.134 kg was employed during the experiments. A high-speed camera at 1000 frames/s and a set of white light sources of Xenon lamps type were used for direct fluid flow visualization. It was observed that the fluid attaches to the outer wall at 15.7 rad/s (150 rpm) and that a portion of fluid travels backwards relative to the rigid body motion. PIV is an optical method of fluid visualization. It is used to obtain instantaneous velocity measurements and related properties in fluids. The fluid is seeded with tracer particles which, for the purposes of PIV, are generally assumed to follow the flow dynamics. The particle concentration must be such that it is possible to identify individual particles in an image. It is the motion of these seeding particles that is used to calculate velocity information of the flow being studied.

Table 2. Experimental system parameters.

Parameter	Description	Amount	Units/Characteristics
r_o	Outer ring radius	0.259	m
r_i	Inner ring radius	0.215	m
h	Ring height	0.074	m
fill	Cavity fluid fill ratio	0.8	Dimensionless
Baffles	Radial ribs	8	Straight equiangularly distributed
ρ	Fluid density	1300	kg/m^3 (sodium chloride)
m_f	Fluid mass	3.857	kg
ω_{cr}	Mean critical speed of rotor assembly	94.25	rad/s
k	Rotor stiffness	$29.5e^3$	N/m
rate	Suspension stiffness	43431	N/m
ψ	Angle between rod suspension and the vertical	80	deg
c_1	Suspension pendular damping	85.2	N·s/m
ω_n	Suspended washing unit natural frequency	20.74	rad/s
m_u	Unbalance mass	1.134	kg

A detailed discussion on PIV and its historical development is provided by Adrian [32]. The PIV technique employed permitted the visualization and quantification of bidimensional velocity fields of the fluid through the seed of particles of alumina whose diameter ranges from 5 y 50 μm. Figure 17 shows the experimental array. The flow was lightened through a laser beam of Yttrium Aluminum Garnet doped with Neodymium (Nd:YAG). The light spread by the particles reaches a Charge Coupled Device (CCD) image sensor camera, which in turn generates consecutive images of the flow. Since the laser beam is of very high frequency nature (pulses of 5 ns), it is possible to "freeze" two consecutive fluid motion frames and from them, build the velocity

vectors. The plant view of the balance ring was made on an area of 90x65 mm, while for the lateral view an area of 240x170 mm was employed.

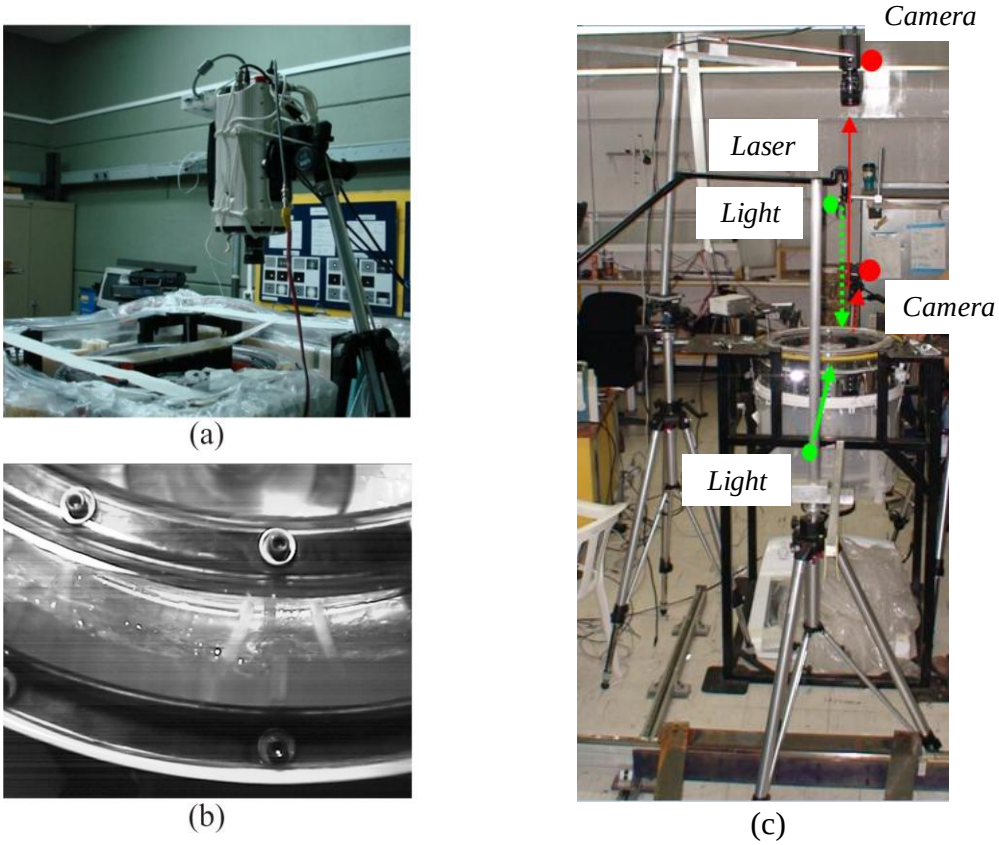

Figure 17. Fluid flow visualization; (a) high-speed camera top view, (b) fluid flow attached to outer wall at 15.7 rad/s (150 rpm), and (c) PIV experimental array.

Due to limitations of the prototype for fluid flow visualization, the maximum attained speed for testing was 51.3 rad/s (490 rpm) since above this speed imminent rubbing between the rotor and tub occurred. The associated maximum tangential velocity of fluid was then 13.2 m/s. The aforementioned shortcoming mainly arose

because of the consequent tub lose of rigidity when its upper part was cut to allow the transparent balance ring side view. Therefore, two different washing units where used. One for fluid flow visualization and PIV, and another for unbalance response measurements. Although the tested 490 rpm speed for fluid flow visualization is lower than the actual operating speed of 670 rpm for the particular vertical-axis washing machine model used in the test bench, some other models employ a balance ring of similar dimensions and characteristics and have a spin velocity of 490 rpm. Then, the data obtained from the experiments is still very useful to understand the fluid-solid interaction of the balance ring device. Furthermore, the fluid flow behavior was observed to be quite similar at both speeds; therefore the findings, analysis and conclusions are considered to be valid enough. Experimental array for plant and side views are represented by dotted and solid lines, respectively. The green lines indicate the light direction, whereas the red lines show the direction of the camera. The red and green circles indicate the position of the camera and light, respectively. The laser beam was orthogonally oriented with respect to the direction of the observing camera by using an articulated arm system.

CHAPTER IV

FLUID FLOW VISUALIZATION AND PIV RESULTS

Experiments without baffles

Experiments were performed in the test rig with an unbalanced rotor [33]. This was not unstable in the absence of fluid in the ring cavity, but it underwent large vibrations due to the synchronous unbalance response. When tested with fluid filling the ring cavity at ratios of 0.5 and 0.8, the unbalance response was synchronous and greatly reduced due to the balancing action of the fluid. However, regardless of the fill ratio, the removal of baffles inside the ring rendered a partially wetted cavity as shown on Fig. 18. A strong unstable vibration occurred at speeds as low as 200 rpm, dwelling in the system natural frequency in the first 2 to 3 seconds after the start up, while the drum rotor barely completed 6 to 10 turns. This almost leaded to destruction of the rig and impended experimental vibration measurements. However, video recording was managed to be taken to observe the rotor excursions, which never reached steady-state. This behavior is similar to trapped fluids (e.g., oil from bearing sumps, steam condensate, etc.) in the internal cavity of high-speed hollow rotors [20]. As explained by [34], the fluid does not remain in simple radial orientation. The spinning surface of the cavity drags the fluid (which has some finite viscosity) in the direction of rotation. This fluid shear stress results in a tangential force in the direction of rotation as illustrated on Fig. 19. This force is called follower force and is the fundamental condition for instability [15].

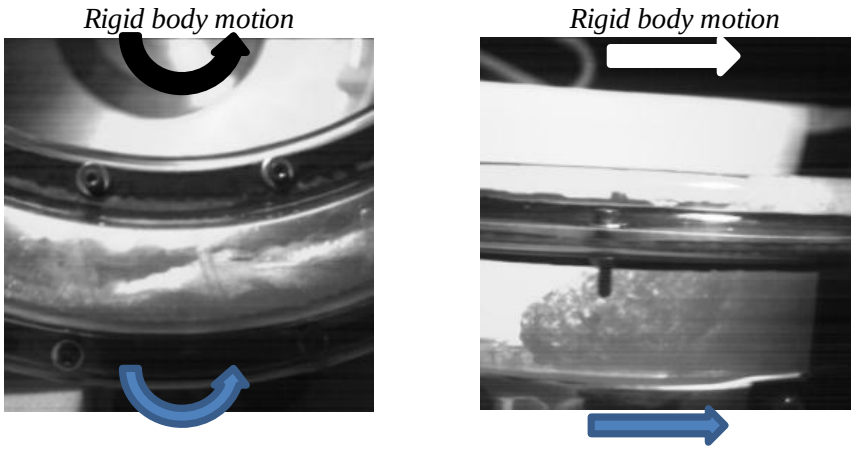

Figure 18. Fluid bulk-flow in a ring with no baffles; (a) top view, and (b) side view.

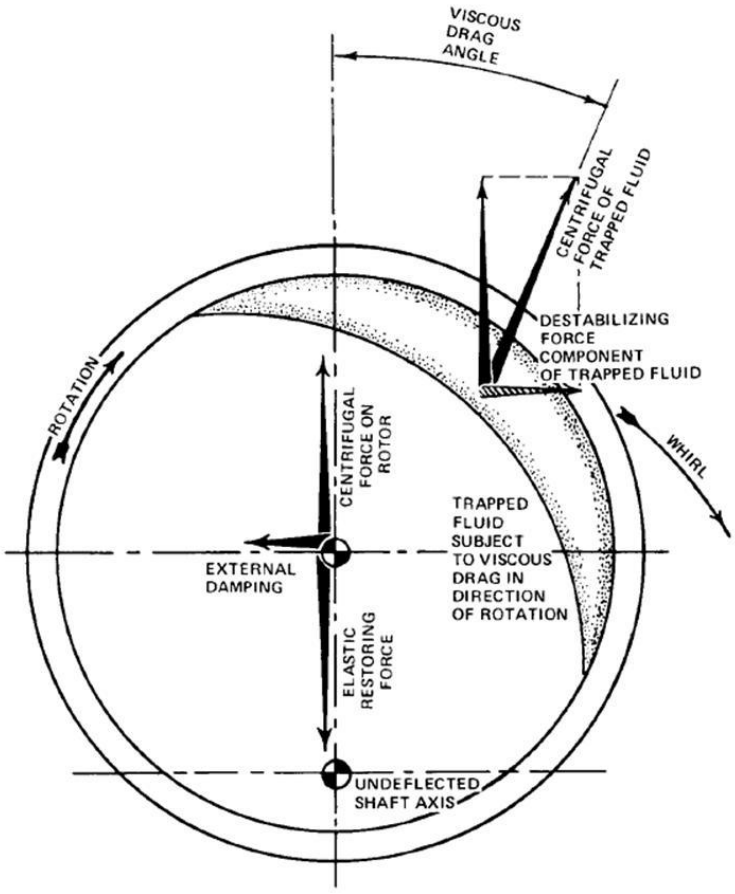

Figure 19. Whirl due to trapped fluid in a rotor, from [20].

Experiments with baseline design (eight baffles)

As shown on Fig. 3 and 9(b), the traditional balance ring design accounts with a number of eight baffles, this number was chosen as a starting point for testing. The addition of eight baffles increased the natural frequency of the fluid and induced a complex fluid mode of vibration as shown on Fig. 20.

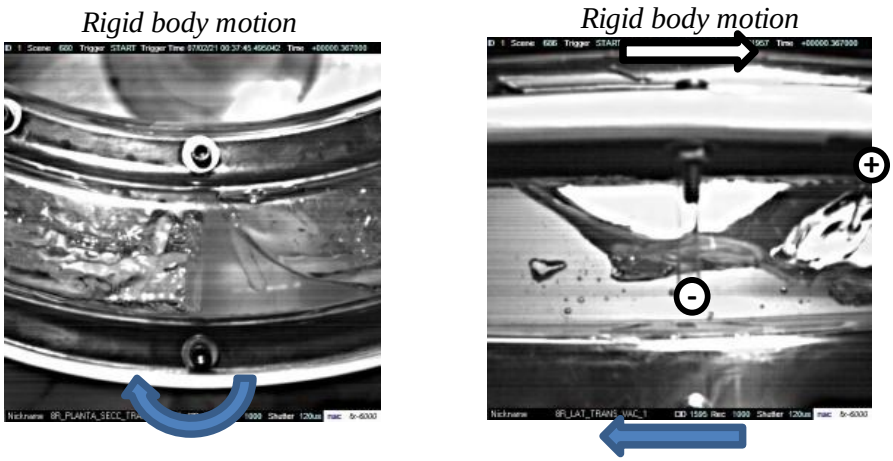

Figure 20. Backward traveling wave; (a) top view, and (b) side view, (+) and (-) indicate a crest and valley, respectively.

At low speed, the fluid force acting on the ring consists of two components, one of which is in phase with the unbalance response, and the other is out of phase by 90^o with it, such that when the rotor is vibrating, the later component has a phase lag of 90^o with the unbalance response. This tangential force is due to the fluid wave traveling backwards relative to the rigid body motion. However, at high speed, there is a balancing

fluid force reacting to the displacement and opposed by an angle about 180^{o} to it. There is also a tangential force 90^{o} phase lagged with respect to the unbalance response due to fluid natural frequency showing as a backward wave, see Fig. 20. Establishing an analogy with the circumferential modes of vibration of a ring with m-modes [36], it can be seen from Fig. 21 that the fourth mode is comparable to the fluid waves induced by the baffle-fluid interaction in the circumferential direction [33]. Furthermore, a comparison with the lateral modes of vibration of a string for the n-modes [36] leads to ascertain that the eighth lateral mode of vibration makes a parallel with the axial wave induced by the baffle-fluid interaction [33].

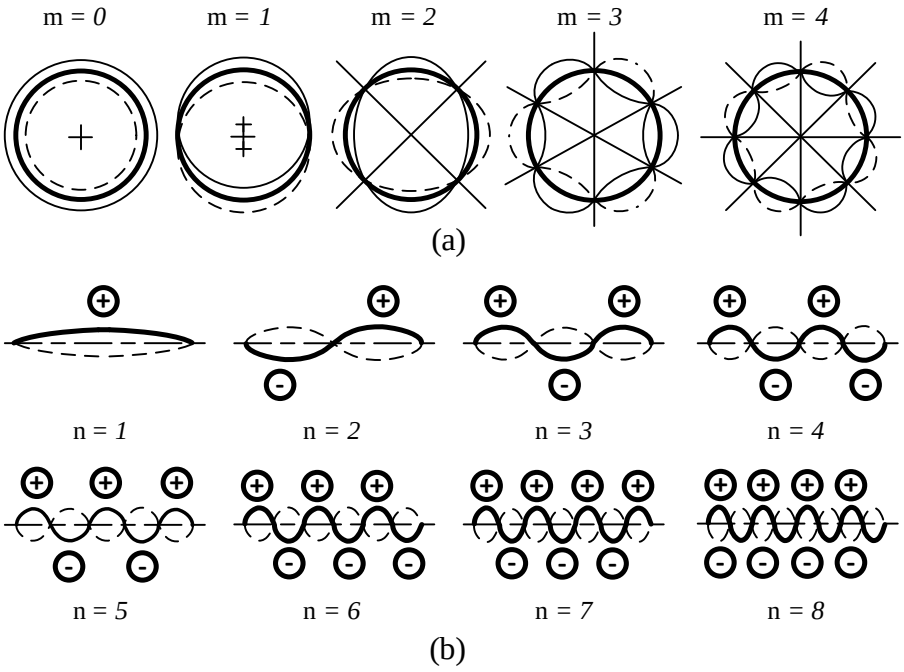

Figure 21. Modes of vibration; (a) circumferential modes of vibration of a thin wall ring, and (b) lateral mode shapes of a string, from [36].

Coupling the fourth circumferential mode of vibration of a ring with the eighth lateral mode of vibration of a string, a complex 3D wave shown schematically on Fig. 22(a) is obtained.

The experimental work showed that the fluid is not stationary relative to the rigid body [33]. The motion in the rotating body is transmitted to the contacting liquid by shear stress. This suggests that waves are occurring in the fluid. Since the spin axis does not coincide with the angular momentum vector, the drum rotor appears to oscillate about its transverse *x* and *y* axes. This oscillation or whirling causes the liquid in the ring to move relative to the rigid body. If the drum rotor spins about a major moment-of-inertia axis, the liquid motions tend to damp the whirling. The energy dissipated by the oscillatory motions is extremely large when the whirling motion excites the liquid into resonance. For that reason, the natural frequencies of a liquid in a spinning rigid body are of much interest. This motion does not relate to free surface sloshing. In fact, the motion occurs throughout the liquid interior and is thus called an internal wave or inertia oscillation. The theory shows that there are many inertia wave modes. The liquid motion associated with these modes does not decay exponentially with depth below the free surface, as would a free surface sloshing mode, but persists all the way through the liquid volume. These are inertia modes and they can occur only for a spinning tank according to Miles and Troesch [35].

Miles and Troesch considered the three-dimensional oscillations of the rotating tank system partially filled with fluid, and with its mth and nth excited natural frequencies. They showed that the disturbed motion of the fluid free surface could not remain irrotational due to a vertical gradient of velocity that necessarily generates vorticity. They have outlined an approach for determining the slosh frequencies in spinning cylinders partially filled with liquid. The natural frequency of the free surface can be obtained from numerical solution of the frequency Eq. (4a) for $\varpi^2 < 1$ and Eq. (4b) for $\varpi^2 > 1$.

$$\begin{vmatrix} \kappa r_o I'_{\mathrm{m}}(\kappa r_o) + \mathrm{m}\varpi I_{\mathrm{m}}(\kappa r_o) & \kappa r_o K'_{\mathrm{m}}(\kappa r_o) + \mathrm{m}\varpi K_{\mathrm{m}}(\kappa r_o) \\ \varpi^2 \kappa r_i I'_{\mathrm{m}}(\kappa r_i) + \left[4(1-\varpi^2) + \mathrm{m}\varpi^3\right] I_{\mathrm{m}}(\kappa r_i) & \varpi^2 \kappa r_i K'_m(\kappa r_i) + \left[4(1-\varpi^2) + \mathrm{m}\varpi^3\right] K_{\mathrm{m}}(\kappa r_i) \end{vmatrix} = 0 \qquad (4a)$$

$$\begin{vmatrix} \bar{\kappa} r_o J'_{\mathrm{m}}(\bar{\kappa} r_o) + \mathrm{m}\varpi J_{\mathrm{m}}(\bar{\kappa} r_o) & \bar{\kappa} r_o Y'_{\mathrm{m}}(\kappa r_o) + \mathrm{m}\varpi Y_{\mathrm{m}}(\bar{\kappa} r_o) \\ \varpi^2 \bar{\kappa} r_i J'_{\mathrm{m}}(\bar{\kappa} r_i) + \left[4(1-\varpi^2) + \mathrm{m}\varpi^3\right] J_{\mathrm{m}}(\bar{\kappa} r_i) & \varpi^2 \bar{\kappa} r_i Y'_m(\bar{\kappa} r_i) + \left[4(1-\varpi^2) + \mathrm{m}\varpi^3\right] Y_{\mathrm{m}}(\bar{\kappa} r_i) \end{vmatrix} = 0 \qquad (4b)$$

Where $\varpi^2 = 2\omega/\omega_f$, I_{m} and K_{m} are the well-known modified Bessel functions of the first and second kind respectively, J_{m} and Y_{m} are Bessel functions of the first and second kind, respectively, $\kappa = (n\pi/h)\sqrt{(1-\varpi^2)}$ and $\bar{\kappa} = (n\pi/h)\sqrt{(\varpi^2-1)}$. Miles and Troesch did not explain however means to achieve higher order fluid modes of vibration other than increasing speed. The present fluid flow visualization allows concluding that an

affordable mechanism consists in placing precisely the baffle boards inside the ring cavity. Solution of the determinant renders the pair of fluid natural frequencies as depicted on Fig. 22(b), one frequency is positive and greater than the rotor angular velocity (fast wave) and the other is negative, i.e. traveling backwards relative to the rigid body, and is slower than the rotor speed (slow wave). Imaginary solutions are found below 20.7 rad/s (198 rpm), this can be related to the fluid transient-state from horizontal to vertical free-surface. PIV and unbalanced response tests evidenced the fast wave not to be present as will be discussed following. Only the slow negative wave turned out to be of importance. The fluid theoretical natural frequency was computed to be an average of $0.983 \times \omega_r$, i.e. very much synchronous with the running speed.

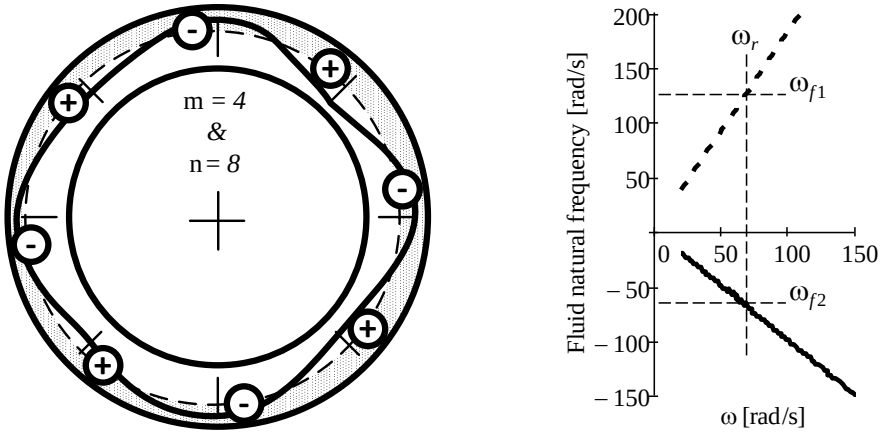

(a) (b)

Figure 22. Complex 3D wave; (a) side view with crest and valley, and (b) coupled vibrating modes; m = *4* and n = *8*.

The fluid relative velocity map was built by superposition of PIV frames for different portions or the balance ring as illustrated on Fig. 23. On the other hand, histogram of fluid velocity on Fig. 23 indicates the solid tangential velocities as 13 m/s, while the fluid average tangential velocity being 12 m/s. Furthermore, waterfall plots of balance ring vibration, shown on Fig. 25, evidence strong synchronous motion with ω_r and almost inexistent asynchronous activity.

The effective mass (m_b) traveling backwards is then a fraction of the total fluid mass given by Eq. (5)

$$15° \times 8 \;\; High\,Re\,lative \;\; Velocity \;\; Zones = 120° = \frac{1}{3} Circumference \tag{5}$$

Therefore, the effective "fluid damping mass" is one third of the total fluid mass

$$m_b = 0.33 \; m_f \tag{6}$$

This mass induces a tangential force 90^o phase lagged with the solid body motion, thus behaving as a damping effect [33].

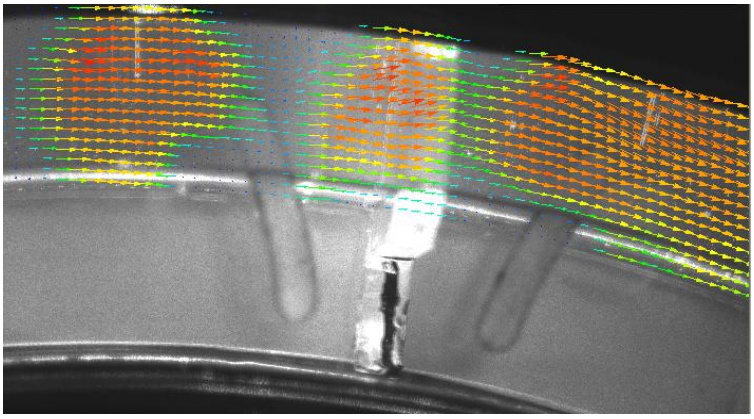

(a)

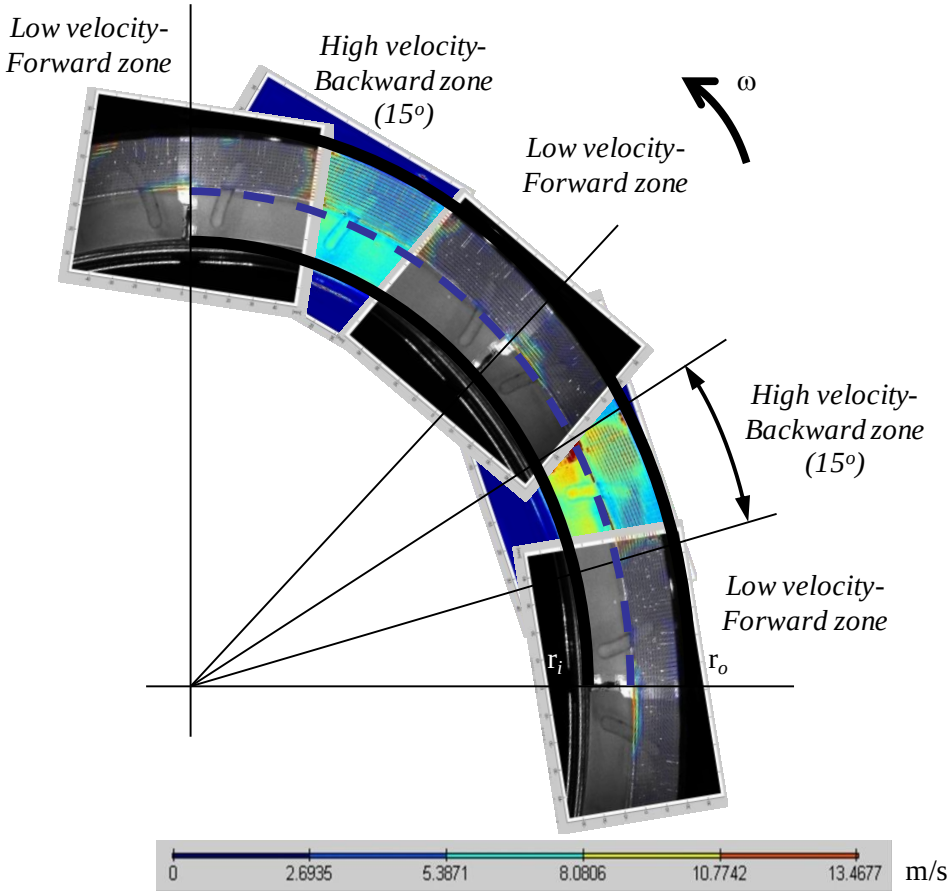

(b)

Figure 23. Balance ring relative velocity map; (a) snapshot at high-velocity zone, and (b) assembled velocity map of one-quarter of ring.

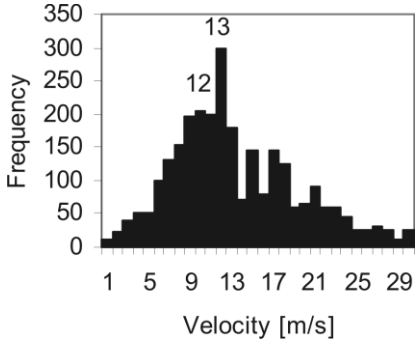

Figure 24. Velocity histogram.

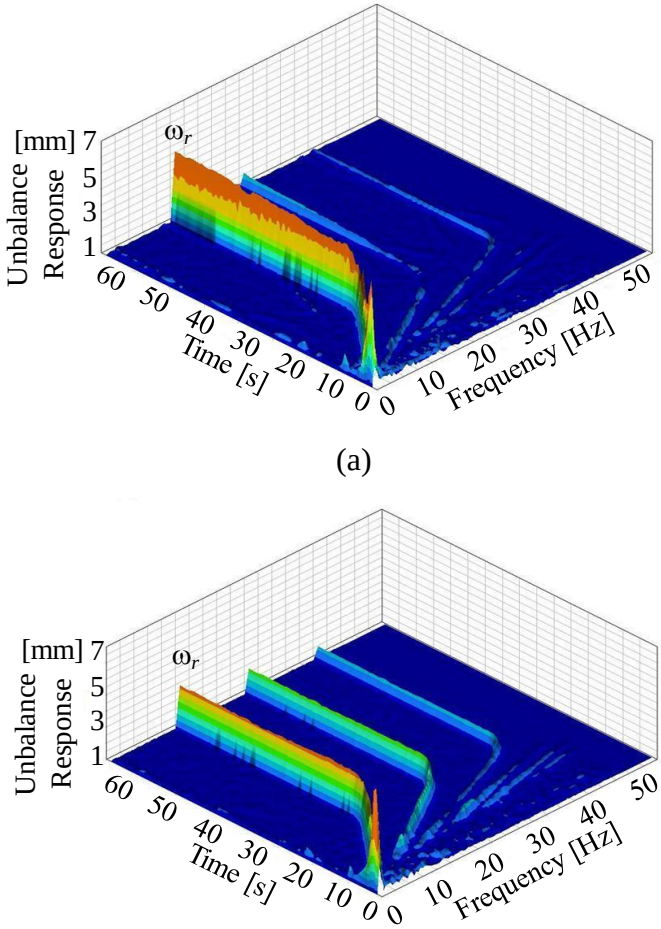

Figure 25. Waterfall vibration plot of balance ring vibration; (a) *x*-axis, and (b) *y*-axis.

CHAPTER V

FLUID FILM DISTRIBUTION

Five cases of study

Based on observation of the experimental results [33], five cases can be identified about the fluid distribution inside the balance ring cavity as illustrated on Fig. 26. Case I corresponds to cero *z* eccentricity and uniform fluid distribution inside the cavity, thus conforming a fluid doughnut with constant fluid film (t_{unif}) and with zero net balancing force. This case is an ideal situation where there is no unbalanced load inside the basket, and therefore unlikely to occur in practice. The center of Mass **M**, center of rotation **C**, center of whirling **O** and fluid center of mass **F** are all coincident as shown on Fig. 26(a). Case II takes place whenever a non-zero unbalance loading conditions exists, the center of mass **M** locates at an offset u_e from the center of rotation **C** and an angle β from the *x*-axis, whereas the fluid center of mass **F** is placed on the *x*-axis at a distance *d* from the center of whirling **O**. A non-zero eccentricity *z* develops and the fluid distributes unevenly around the ring cavity, having a film thickness t_0 at $\phi = 0^o$. Case II is the more recurrent fluid distribution condition, see Fig.26(b). Case III happens under large unbalance conditions, when the fluid film thickness around the ring equates to $r_o - r_i$ at $\phi = 0^o$ and amounts to 0 at $\phi = 180^o$ as shown on Fig. 26(c). The eccentricity in such case is given by Eq. (7) and is the maximum rotor motion the liquid balance ring can effectively compensate for, as shown on Fig. 26(f). The maximum available balancing force from the fluid is then predicted by Eq. (8).

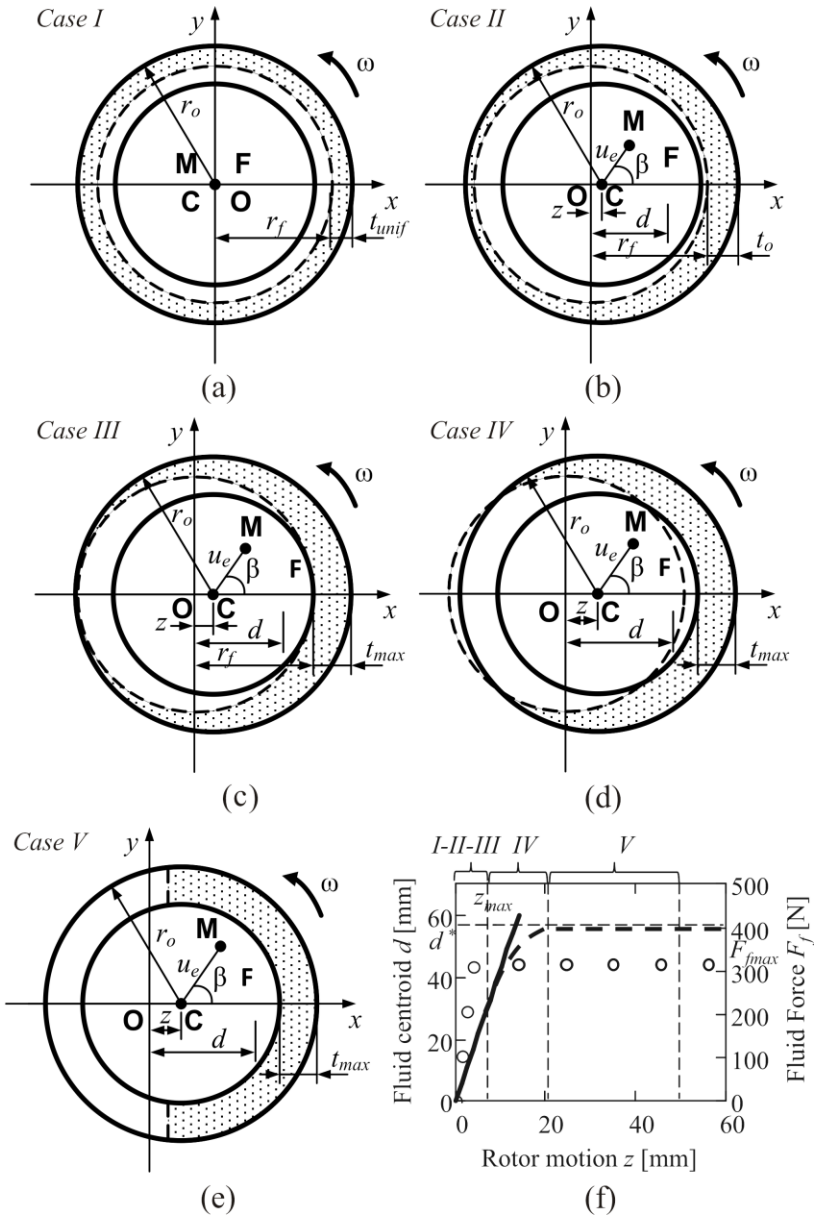

Figure 26. Fluid distribution; (a) case I, (b) case II, (c) case III, (d) case IV, (e) case V, and (f) fluid center of mass location (— and --) and fluid force (o's).

$$z_{max} = \frac{r_o - r_i}{2} \tag{7}$$

$$F_{f\,max} = \left[fill \;\; \left(r_o^2 - r_i^2 \right) \; h \; \rho \right] \left(\frac{r_o - r_i}{2} \right) \omega^2 \tag{8}$$

Any rotor motion beyond z_{max} induced by a very large unbalanced load would show a fluid distribution similar to case IV on Fig. 26(d), where the fluid film no longer wets the entire ring cavity. Case V may develop under extremely large unbalanced conditions, where the fluid is totally plastered at one side of the balance ring cavity as depicted on Fig. 26(e). Experimental fluid flow visualization shown on picture of Fig. 18 resembles this case, where a clear free-surface front wave can be appreciated. The fluid moved like a bulk attached to the ring outer wall. The unbalanced basket experiments without baffles in the ring evidenced a very dangerous rotor motion, because at low speed, the unbalanced load placed inside the basket, increased by the added fluid mass in the ring, thus inducing violent vibration. The driving motor was stopped to avoid destruction of the test rig. However, the addition of baffles in the ring, prevented from violent liquid sloshing and throughout all experiments performed, the fluid distribution was always seen to be similar to cases I to III, a typical case is shown on Fig. 26(b).

Unbalance and fluid-solid interaction

Cases I to III were observed whenever baffles where used for moderate to high unbalance. Case IV was present with baffles provided in the ring at very high unbalance. On the other hand, Case V was only seen without baffles in the cavity for any amount of unbalance. Therefore, baffles play an important role in the fluid distribution allowing

wetting the entire cavity under moderate to large unbalance. The distance from the fluid center of mass to the center of whirling is given by Eq. (9)

$$d^* = \frac{\int_0^{fill\ \pi}\int_{r_i}^{r_o} r^2 \cos\theta\ dr d\theta}{\int_0^{fill\ \pi}\int_{r_i}^{r_o} r\ dr d\theta} = \frac{2}{3}\frac{sin(fill\ \pi)}{fill\ \pi}\left(\mathrm{r}_i + \frac{\mathrm{r}_o^2}{\mathrm{r}_i + \mathrm{r}_o}\right) \tag{9}$$

In all events, due to the presence of the baffles, the fluid center of mass location may be predicted as linearly dependant on the rotor motion according to Eq. (10). Appendix A shows how the parameter *d* is obtained.

$$d = \frac{z\mathrm{r}_f^2}{\mathrm{r}_o^2 - \mathrm{r}_f^2} \tag{10}$$

On the other hand, the ring fill ratio to maximize the balancing force is given by Eq. (11), which for the balance ring under study is about 52%.

$$fill_{opt} = \frac{\pi\left[\mathrm{r}_o^2 - (\mathrm{r}_i + z_{max})^2\right]}{\pi(\mathrm{r}_o - \mathrm{r}_i)^2} \tag{11}$$

CHAPTER VI

DYNAMIC MODEL OF A WASHING MACHINE

4-dof dynamic model

Although the system bounces vertically and also describes a planar motion, it is accurate enough to address only the governing planar motion, which is usually 3 to 5 and 6 to 8 times larger than the vertical one in the transient-state and steady-state, respectively. Following this rationale, Figure 27 provides a 4-dof dynamic model of the washing machine.

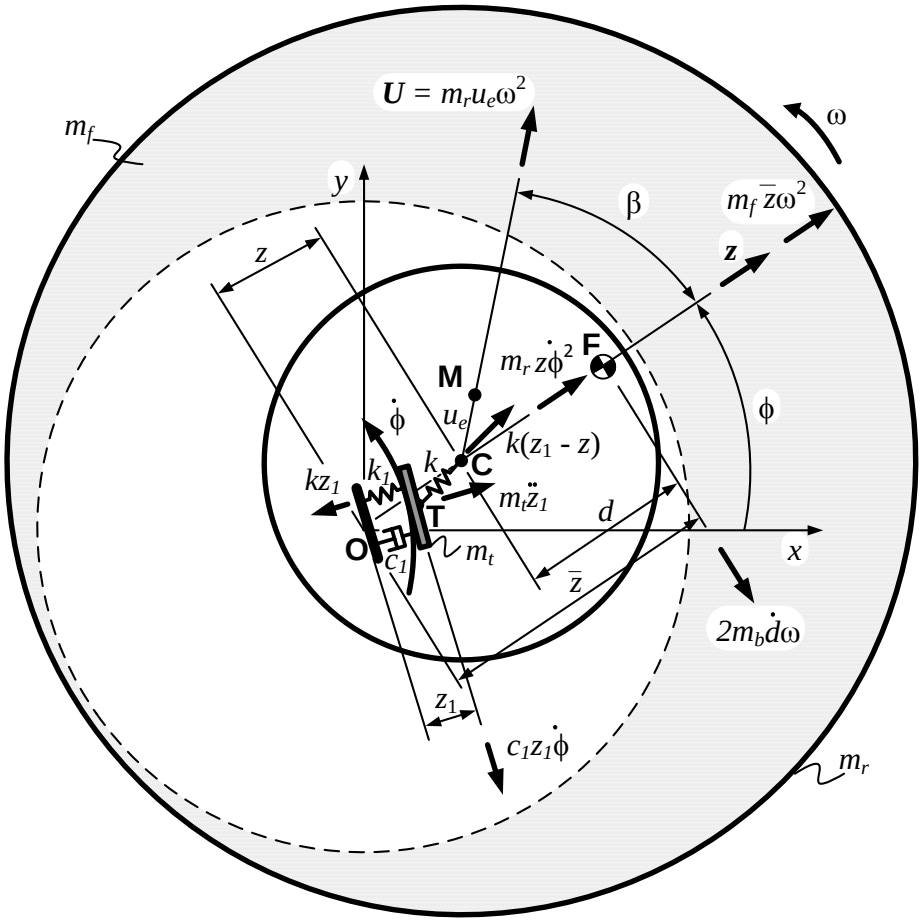

Figure 27. Dynamic model; displacement vector and force diagram.

Using complex notation, $\boldsymbol{z}$ and $\boldsymbol{z}_1$ can be expressed as general complex functions.

$$\boldsymbol{z} = x + iy \tag{12}$$

$$\boldsymbol{z}_1 = x + iy \tag{13}$$

PIV measurements and fluid natural frequency analysis allow assuming synchronous motion, i.e. $\dot{\phi} = \omega$ with enough accuracy. Then, the $\boldsymbol{z}$-equation of motion of the drum rotor is given by [37]

$$m_r\ddot{\boldsymbol{z}} + k(\boldsymbol{z} - \boldsymbol{z}_1) + m_f\bar{\boldsymbol{z}}\omega^2 + m_b\dot{\boldsymbol{d}}\omega = mu_e\omega^2 e^{i\omega t} \tag{14}$$

Where $\boldsymbol{d}$ and $\bar{\boldsymbol{z}}$ useful substitutions provided in Appendix A, such that Eq. (14) becomes a second order linear differential equation with constant coefficients and can have a closed form solution. Note that a damping term $2m_b\dot{\boldsymbol{d}}\omega$ has been added, which can be thought mainly due to viscous dissipation in the bulk-flow. Otherwise stated, this additional damping is due to the mass fraction moving backwards relative to the rigid body, which wave frequency is synchronous with ω. On the other hand, the $\boldsymbol{z}_1$-equation of motion of the whirling tub is defined as [37]

$$m_t\ddot{\boldsymbol{z}}_1 + k_1\boldsymbol{z}_1 + k(\boldsymbol{z}_1 - \boldsymbol{z}) + c_1\dot{\boldsymbol{z}}_1 = 0 \tag{15}$$

Let's assume a solution of the form $\boldsymbol{z} = ze^{i\omega t}$ and $\boldsymbol{z}_1 = z_1 e^{i\omega t}$ and define the stiffness, stiffness ratio, damping ratio, mass ratio, and frequency ratio as Eqs. (16-20), respectively

$$k_1 = 4 \cdot rate \cdot cos(\psi) \tag{16}$$

$$\mathrm{K} = \frac{k_1}{k} \tag{17}$$

$$\xi_1 = \frac{c_1}{2m_r \omega_{cr}} \tag{18}$$

$$\mathrm{M} = \frac{m_t}{m_r} \tag{19}$$

$$\mathrm{f} = \frac{\omega}{\omega_{cr}} \tag{20}$$

After some manipulation, *z* is given by

$$z = \frac{u_e}{\left[\left(\frac{\Omega^2}{\omega^2} - 1 + \frac{\rho \pi \mathrm{r}_o^2 h}{m_r}\right)^2 + \left(2\frac{\omega}{\omega_{cr}}\xi_e + \frac{2m_b}{m_r}\left(\frac{\mathrm{r}_f^2}{\mathrm{r}_o^2 - \mathrm{r}_f^2}\right)\right)^2\right]^{1/2}} \tag{21}$$

Where

$$u_e = \frac{m_u \mathrm{r}_o}{m_r + m_u} \tag{22}$$

$$\Omega^2 = \omega_{cr}^2 \left[\frac{\mathrm{D} - (\mathrm{K}+1) + \mathrm{Mf}^2}{\mathrm{D}} \right] \tag{23}$$

$$\mathrm{D} = \left[(\mathrm{K}+1)^2 + (2\xi_1 \mathrm{f})^2 + \mathrm{Mf}^2 (\mathrm{Mf}^2 - 2\mathrm{K} - 2) \right] \tag{24}$$

$$\xi_e = \frac{\xi_1}{\mathrm{D}} \tag{25}$$

$$\bar{z} = \frac{z \mathrm{r}_o^2}{(\mathrm{r}_o^2 - \mathrm{r}_i^2)} \tag{26}$$

The phase lag is given by

$$\beta = \tan^{-1} \left[\frac{2 \frac{\omega}{\omega_{cr}} \xi_e + \frac{m_b}{m_r} \left(\frac{\mathrm{r}_f^2}{\mathrm{r}_o^2 - \mathrm{r}_f^2} \right)}{\frac{\Omega^2}{\omega^2} - 1 + \frac{\rho \pi \mathrm{r}_o^2 h}{m_r}} \right] \tag{27}$$

Then, solution for z_1 is given by

$$z_1 = \frac{z}{\left[(\mathrm{K} + 1 - \mathrm{Mf}^2)^2 + (2\xi_1 \mathrm{f})^2 \right]^{1/2}} \tag{28}$$

Finally, having defined ξ_e, the transmissibility ratio to the structure is as follows

$$\mathrm{TR} = \left[\frac{1 + 4\xi_e \omega^2 \left(\frac{\omega}{\omega_n} \right)^2}{\left(1 - \left(\frac{\omega}{\omega_n} \right)^2 \right)^2 + 4\xi_e \omega^2 \left(\frac{\omega}{\omega_n} \right)^2} \right] \tag{29}$$

Where ω_n is the natural frequency of the tub-suspension assembly, given by

$$\omega_n = \left[\frac{4 \cdot rate}{m_r + m_t} \right]^{1/2} \tag{30}$$

From Eq. (21), it can be appreciated that the equivalent mass of the balance ring is the full disc, not the fluid annulus actually present.

Correlation

Eqs. (21, and 27-29) are graphed for examination on Fig. 28. Model correlates very well for the transient and steady-state throughout the frequency range tested [37]. Furthermore, solution for β indicates that an angle of 153^o between the unbalance and maximum displacement location exist, which can be confirmed on Fig. 29 by the 30^o angle between the unbalance vector and the thinnest fluid zone. Owing to the fact that, the fluid center of mass is aligned with the displacement vector, then there is a complementary angle of 150^o between the unbalance and the fluid center of mass. Put differently, the unbalance vector ***U*** is not exactly opposed by the fluid balancing force vector $\boldsymbol{F_f}$, but by a fraction of it, computed as $F_f \cos(30^o)$. Experimental visualization of

the unbalance mass and fluid distribution allows good model correlation. Note that a major disadvantage of the liquid balancer is to add mass to the unbalance while operating below the first natural frequency. Hence, any system being considered for this type of balancing needs to have a relatively low resonant frequency, as is the case of the washing machine.

Figure 30 depicts the unbalance response of a washing machine without fluid balance ring. It can be observed that the vibration at low frequency is greatly reduced. On the other hand, vibration at steady-state approximately doubles due to absence of the balancing force from the liquid. Furthermore, the vibration transmissibility undergoes two sharp peaks, being the second one of major concern, since it locates in the high frequency zone, where the exciting unbalance forces are of great magnitude due to centrifugal effect. Vibration transmitted to the cabinet structure is magnified leading to cabinet shaking and imminent walking. A balance ring fill ratio of 0.5 is considered on Fig. 31. Under this situation, the unbalance response across the frequency range is lower than that of the 0.8 fill ratio case. However, the transmissibility ratio finds an undesirable peak at the running frequency due to the reduced fluid mass. Therefore, indicating either, the need of the added mass provided by the 0.8 fill ratio case or added mass to the suspended washing unit on the form of a dead load. The former is more affordable due to low cost, whereas the later is usually much more expensive since concrete or steel counterweights need to be employed.

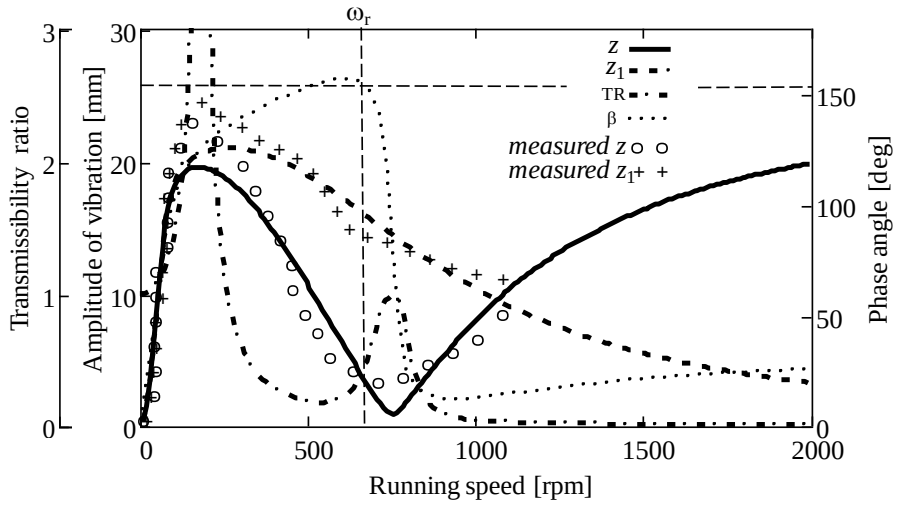

Figure 28. Washing machine dynamic unbalanced response at a fill ratio of 0.8.

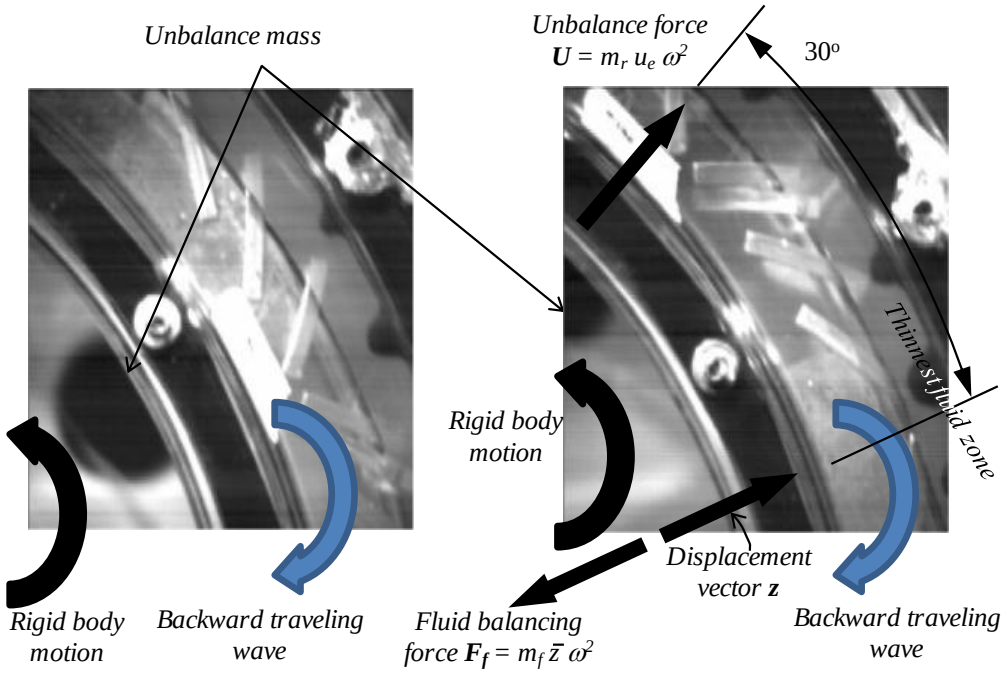

Figure 29. Fluid distribution relative to unbalance mass location; (a) unbalance mass location, (b) relative location of thinnest fluid zone to unbalance mass location.

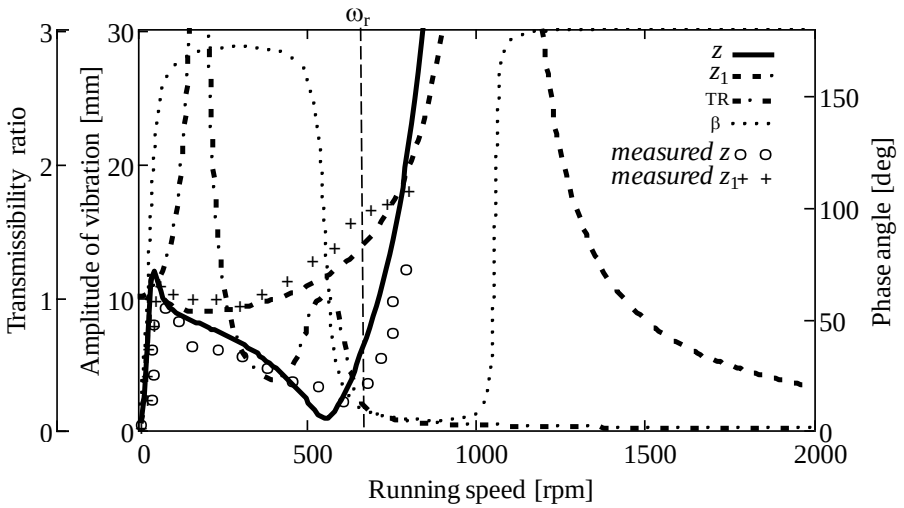

Figure 30. Washing machine dynamic unbalanced response at a fill ratio of 0.

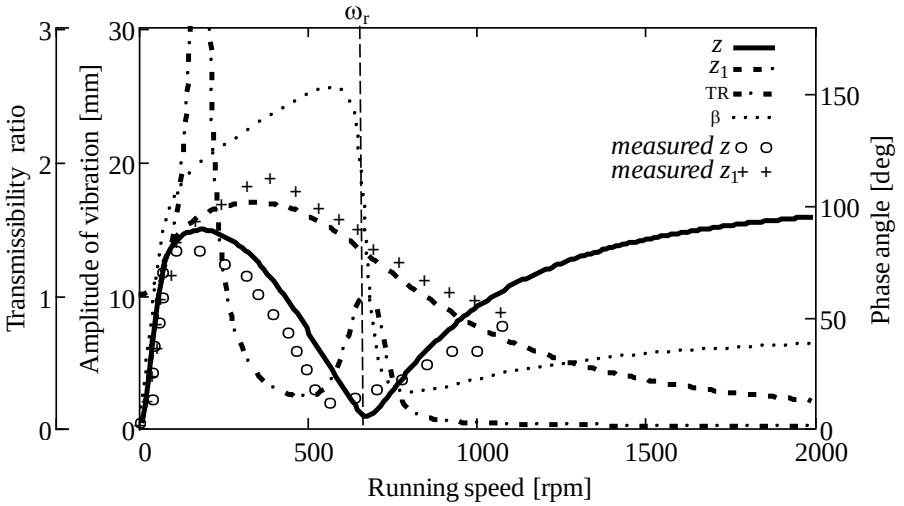

Figure 31. Washing machine dynamic unbalanced response at a fill ratio of 0.5.

CHAPTER VII

UNBALANCE RESPONSE OF A FLEXIBLE ROTOR MOUNTED ON FLEXIBLE SUPPORTS

Turbomachinery flexible rotor

Figure 32 provides a 4-dof dynamic model of a flexible rotor in flexible symmetric damped bearings and with a liquid balance ring. It has been assumed that the bearings cross-coupled stiffness and damping coefficients are negligible as might be the case of tilting pad journal bearings and squeeze film dampers employed in many turbomachinery rotors. Thus bearings are not considered to be a source of instability in this analysis. Moreover, for the sake of simplicity, the bearings are assumed to be essentially identical and symmetric.

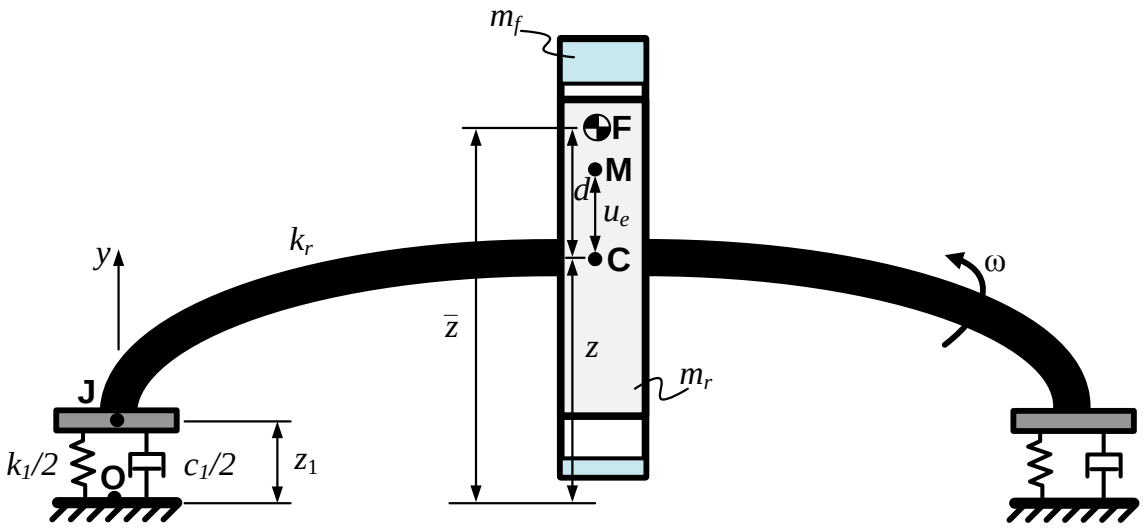

Figure 32. Dynamic model of a flexible rotor with a liquid balance ring.

Then, for the flexible rotor, the differential equations of motion of the rotor are given by [38]

$$m_r\ddot{\boldsymbol{z}} + k_r\left(\boldsymbol{z} - \boldsymbol{z}_1\right) + m_f\,\bar{\boldsymbol{z}}\omega^2 + 2m_b\dot{\boldsymbol{d}}\omega = m_r u_e \omega^2 e^{j\omega t} \tag{31}$$

$$k_1\boldsymbol{z}_1 + k_r\left(\boldsymbol{z}_1 - \boldsymbol{z}\right) + c_1\dot{\boldsymbol{z}}_1 = 0 \tag{32}$$

Figure 33 provides a side view of a 4-dof model of a flexible rotor on flexible supports.

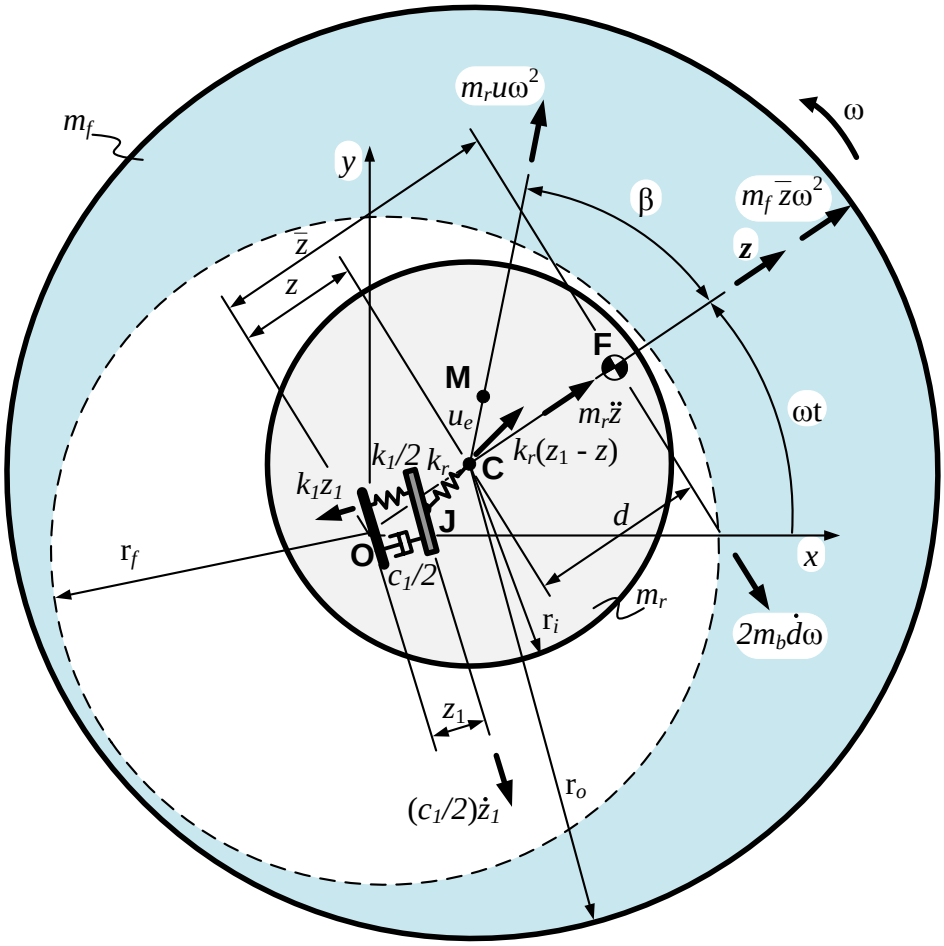

Figure 33. Side view of flexible rotor with a liquid balance ring.

Eqs. (3) and (4) are combined to give

$$\ddot{\boldsymbol{z}} + 2\omega_{cr}\xi_e\dot{\boldsymbol{z}} + 2\mathrm{M}_b\dot{\boldsymbol{d}}\omega + \Omega^2\boldsymbol{z} + \mathrm{M}\bar{\boldsymbol{z}}\omega^2 = u_e\omega^2 e^{j\omega t} \tag{33}$$

Note that a damping term $2m_b\boldsymbol{d}^{\cdot}\omega$ has been added, which can be thought mainly as viscous dissipation in the bulk-flow. In other words, this additional damping is due to the mass fraction moving backwards relative to the rigid body. The acceleration of the backward traveling wave, which mass is m_b, has no radial component and only possesses tangential or Coriolis acceleration given by $2\boldsymbol{d}^{\cdot}\omega$. Therefore, its tangential force is defined by the term $2m_b\boldsymbol{d}^{\cdot}\omega$, where the wave frequency is synchronous with ω. Solution of Eqs. (31) and (32) is detailed in Appendix B and renders

$$z = \frac{u_e}{\left[\left(\frac{\Omega^2}{\omega^2} - 1 + \frac{\rho\pi r_o^2 h}{m_r}\right)^2 + \left(2\frac{\omega}{\omega_{cr}}\xi_e + 2\mathrm{M}_b\left(\frac{\mathrm{r}_f^2}{\mathrm{r}_o^2 - \mathrm{r}_f^2}\right)\right)^2\right]^{1/2}} \tag{34}$$

$$z_1 = \frac{z}{\left[\left(\mathrm{K} + 1 - \mathrm{M}\mathrm{f}^2\right)^2 + \left(2\xi_1\mathrm{f}\right)^2\right]^{1/2}} \tag{35}$$

The phase lag is given by

$$\beta = \tan^{-1}\left[\frac{2\frac{\omega}{\omega_{cr}}\xi_e + 2M_b\left(\frac{r_f^2}{r_o^2 - r_f^2}\right)}{\frac{\Omega^2}{\omega^2} - 1 + \frac{\rho\pi r_o^2 h}{m_r}}\right] \tag{36}$$

Where

$$\Omega^2 = \omega_{cr}^2\left[\frac{K(K+1) + (2f\xi_1)^2}{(K+1)^2 + (2f\xi_1)^2}\right] \tag{37}$$

Note that Ω is the rotor critical speed on flexible supports.

$$\xi_e = \frac{\xi_1}{(K+1)^2 + (2\xi_1 f)^2} \tag{38}$$

Optimum damping

Gunter *et. al.* [39] has shown that the effective damping can be maximized with respect to the bearing damping by finding the value of ξ_1 which satisfies $\partial\xi_e/\partial\xi_1 = 0$.

Let f = 1

$$\frac{\partial\xi_e}{\partial\xi_1} = \frac{(1+K)^2 - 4\xi_1^2}{\left[(1+K)^2 + 4\xi_1^2\right]^2} \tag{39}$$

Because $\xi_1 \geq 0$ Eq. (39) is equal to 0 if

$$\xi_1 = \xi_{1op} = \frac{\mathrm{K}+1}{2} \tag{40}$$

With $\xi_1 = \xi_{1op}$

$$\xi_e = \xi_{em} = \frac{1}{4(\mathrm{K}+1)} \tag{41}$$

$$\xi_{1op} = \frac{\mathrm{K}+1}{2} \tag{42}$$

The effects of aerodynamic cross-coupling and rotor internal damping will be considered in the following chapter.

CHAPTER VIII

STABILITY WITH OPTIMUM DAMPING

Stability with optimum damping and a LeBlanc balancer

Rotor bearing systems are frequently subjected to self-excited instabilities mechanisms including bearings, seals, aerodynamic effects, and internal rotor friction damping. Appendix C explains these destabilizing mechanisms. For free damped vibrations with aerodynamic cross-coupling and optimum bearing damping, Eq. (33) becomes [38]

$$\ddot{\boldsymbol{z}} + 2\omega_{cr}\xi_{em}\dot{\boldsymbol{z}} + 2\mathrm{M}_b\dot{\boldsymbol{d}}\omega + (\Omega^2 - j\mathrm{Q})\boldsymbol{z} + \mathrm{M}\bar{\boldsymbol{z}}\omega^2 = u_e\omega^2 e^{j\omega t} \tag{43}$$

Where ξ_{em} is given by Eq. (41) and $\mathrm{Q} = q/m_r$

$$\Omega_{op}^2 = \omega_{cr}^2\left[\frac{2\mathrm{K}+1}{2(\mathrm{K}+1)}\right] \tag{44}$$

With viscous internal friction damping Eq. (33) becomes [38]

$$\ddot{\boldsymbol{z}} + 2\omega_{cr}(\xi_{em} + \xi_{\mathrm{i}})\dot{\boldsymbol{z}} + 2\mathrm{M}_b\dot{\boldsymbol{d}}\omega + \Omega^2\boldsymbol{z} + \mathrm{M}\bar{\boldsymbol{z}}\omega^2 = u_e\omega^2 e^{j\omega t} \tag{45}$$

Assuming an exponential function of the form $\boldsymbol{z} = ze^{st}$, the characteristic equation is of the form

$$m_r s^2 + \left[c_{em} + c_{\mathrm{i}} + 2m_b \omega \left(\frac{\mathrm{r}_f^2}{\mathrm{r}_o^2 - \mathrm{r}_f^2} \right) \right] s + \frac{\mathrm{K}(2\mathrm{K}+1)}{2(\mathrm{K}+1)} + m_f \left(\frac{\mathrm{r}_o^2}{\mathrm{r}_o^2 - \mathrm{r}_f^2} \right) \omega^2 = 0 \qquad (46)$$

The values of s satisfying Eq. (45) are the system eigenvalues. Since s is complex, Eq. (46) represents a complex function. In order to be zero, both the real and imaginary parts must be simultaneously zero. Substituting $s = \lambda + j\omega_d$ into Eq. (16) and equating individually the real and imaginary part to zero results in a pair or polynomial with real coefficients, which need to be solved simultaneously. A rather simple solution for which the rotor becomes unstable can be found by substituting $\lambda = 0$ to deliver

$$\omega_{d\,op} = \left[\omega_{cr}^2 \left(\frac{2\mathrm{K}+1}{2(\mathrm{K}+1)} \right) + 2\omega^2 \mathrm{M}_b \left(\frac{\mathrm{r}_f^2}{\mathrm{r}_o^2 - \mathrm{r}_f^2} \right) \right]^{1/2} \qquad (47)$$

Whereas with viscous internal friction damping, the rotor will only be stable if the operating speed is

$$\omega < \Omega_{op} \left[1 + \frac{1}{4(1+\mathrm{K})\xi_{\mathrm{i}}} + \mathrm{M}_b \frac{\mathrm{f}}{\xi_{\mathrm{i}}} \left(\frac{\mathrm{r}_f^2}{\mathrm{r}_o^2 - \mathrm{r}_f^2} \right) \right]^{1/2} \qquad (48)$$

According to Eq. (47), when the rotor is unstable, it whirls at the undamped natural frequency plus the rising term depending on the traveling backwards mass of the LeBlanc balancer and its geometrical properties as well. On the other hand, Eq. (48) shows that for the rotor to be unstable due to internal friction damping, the rotational speed must exceed the undamped natural frequency plus a destabilizing term depending on the internal friction damping, plus a rising term depending on the traveling backward mass of the LeBlanc balancer and its geometrical properties.

While the maximum permissible aerodynamic cross-coupling with optimum damping is

$$q_{mop} = 2m_r \omega_{cr} \omega_d \left[\xi_{em} + \mathrm{M}_b \frac{\mathrm{f}}{2} \left(\frac{\mathrm{r}_f^2}{\mathrm{r}_o^2 - \mathrm{r}_f^2} \right) \right]^{1/2} \tag{49}$$

Industrial rotor examples

Industrial rotor cases will be taken form reference [39] to analyze the effect of the LeBlanc balancer to improve their stability. The internal damping for those rotors is unknown a priori. Some guessed values for the internal damping will be assumed for two conditions, namely loose and tight fit. The first example is a ten-stage centrifugal compressor, designated in the following as the “light-rotor”. The unit is nearly symmetrical and the rotor is supported in two five-pad tilting pad bearings. A second example, considers the seven-stage centrifugal compressor, designated from now on as

the ‘heavy rotor”. This is a rotor mounted on very rigid pressure dam journal bearings with different stiffness values on the horizontal and vertical directions. The third example deals with an eight-stage centrifugal compressor supported on tilting pad journal bearings mounted in series with squeeze film dampers, where the stiffness values on the horizontal and vertical direction differ greatly from each other. The final example is the Space Shuttle Main Engine-High Pressure Fuel Turbopump (SSME-HPFTP). The HPFTP consists of a three-stage centrifugal pump section and a two-stage turbine section as shown in Fig. 34. Details of the pump configuration are given in reference [40]. The rotating assembly is supported in flexible mounted ball bearings and is acted on by aerodynamic cross-coupling forces in the turbine section.

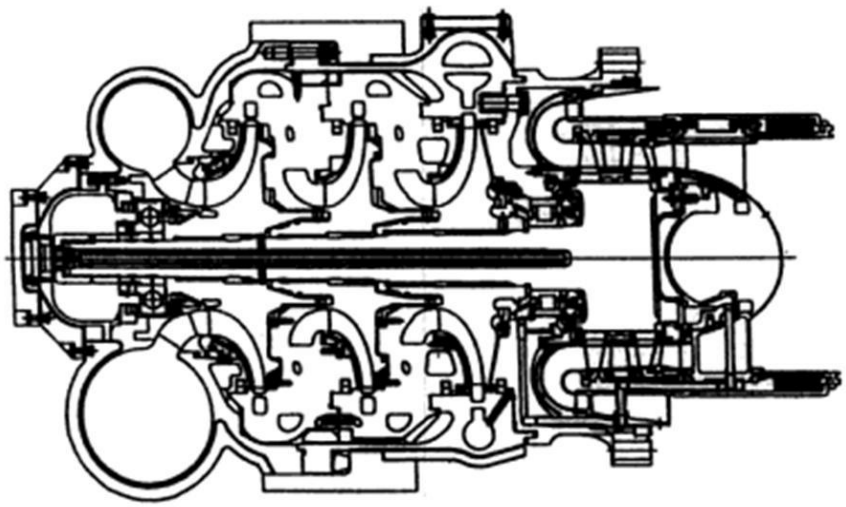

Figure 34. Space Shuttle Main Engine-High Pressure Fuel Turbopump (SSME-HPFTP), from Childs [40].

For the purpose of analyzing the stabilizing effect of the LeBlanc balancer, it will be assumed that little damping is provided to the rotor from the bearings, supports and seals. The supports will be considered symmetric and isotropic. Different bearing stiffness values will be considered. A balance ring with dimensions r_o = 0.102 m (4 in), r_i = 0.076 m (3 in), h = 0.076 m (3 in), filled with a liquid density of ρ = 1300 kg/m^3 at ratio of 0.5 as recommend by [6] to maximize the balancing capabilities of the trapped fluid in the cavity. The fluid free surface radius r_f is given by Eq. (50). Table 3 summarizes the threshold speed of instability and maximum aerodynamic cross-coupling improvements for all the example rotors.

$$r_f = \left[0.5\ \left(r_i^2 - r_o^2\right) + r_o^2\right]^{0.5} \tag{50}$$

Table 3. Summary of stability results of industrial example rotors employing a LeBlanc Balancer.

								Rotor Internal		Threshold speed of instability [rpm] Loose		Tight			
Rotor	Direction	Operating speed [rpm]	Balance ring	K	Modal mass [kg]	Critical Speed [rpm]	Whirl frequency [cpm]	Loose	Tight	ωd op [rpm]	% of increase	ωd op [rpm]	% of increase	qm op [N/cm]	% of increase
Light rotor	Horizontal	Above critical	Without	3.4	215	5100	3735	0.059	0.0313	5148	4	6398	6	21390	12
			With				3776			5377		6794		24244	
	Vertical		Without	5.9			4912	0.059	0.0313	7928	5	10597	7	42749	11
			With				4990			8381		11382		48056	
Heavy rotor	Symmetrical	Above critical	Without	29.2	2524	2540	2519	0.059	0.0313	2872	1	3185	1	29320	4
			With				2522			2890		3216		30521	
8-stage compressor	Horizontal	10,000	Without	10.2	306	3821	3735	0.059	0.0313	5148	4	6398	6	21390	12
			With				3776			5377		6794		24244	
	Vertical		Without	0.36			3038	0.059	0.0313	12505	3	20883	3	143313	3
			With				3088			12853		21494		147815	
SSME-HPFTP	Symmetrical	28000	Without	0.71	29	16500	13880	0.118	0.0626	31076	21	46295	23	213187	27
			With				15903			39450		60290		291923	
			Without	2.02			15072	0.118	0.0626	25646	22	35004	26	131085	34
			With				16954			32946		47099		198260	
			Without	4.04			15660	0.118	0.0626	22243	23	28069	29	81610	43
			With				17478			29051		39293		143471	

Discussion

The optimum bearing damping for all the rotors exemplified was determined and used as an input in the analysis. Despite of the optimization of the external damping and the relatively high internal rotor damping values employed significant improvements in the threshold speed of instability and maximum aerodynamic cross-coupling were obtained. However for the "heavy rotor" case, with the extremely stiff bearings, the flexible bearing critical speed is very close to the rigid bearing critical speed and even the external damping provided by the balance ring has little stabilizing effect since the bearing amplitudes are very small. The 8-stage centrifugal compressor with K = 0.36 in the vertical direction is another situation where the balance ring does not contribute much to the stability characteristics. In this case, the bearing supports flexibility is so large, that the external damping provided by the tilting pad journal bearings in series with the squeeze film dampers, is successful to provide enough damping to move forward the threshold speed of instability. The balance ring is of great help in the case of the SSME-HPFTP rotor, the internal rotor damping values used in this example are twice those for the other cases though. The apparent benefit is due to the high operating speed. This will need further experimental verification to ascertain whether the fluid behaves entirely as a solid at such high speed and confirm if the fluid backward traveling wave that provide the damping effect persists or vanishes. The added mass of the balance ring was only 1.845 kg, the dimensions of the ring are feasible and relatively easy to fit in the rotors design with some engineering work. This kind of devices can be particularly attractive for using in hollow rotors. Note that the balance ring will show

even better stability improvements in rotors that by design do not have optimum external damping. The analysis can be further extended to consider asymmetric and orthotropic supports and other models for internal damping available in the literature.

CHAPTER IX

BALANCE RING WITH CURVED BAFFLES (BLADES)

Fluid particle differential equation of motion

Nowadays, in regard to the shape of the baffles boards employed in liquid balance ring devices, the use of straight baffles (L_s) is the standard practice. However, as the fluid is subjected to rotation, it makes sense to believe that there should be an optimal baffle curvature (L_a) to enhance the fluid-solid interaction and improve the balance ring dynamic performance. This chapter introduces for the first time, a liquid balance ring with non-straight baffles to improve its dynamic response in the transient-state as well as the steady-state. This novel bladed concept will be used in designing a liquid balance ring for high-speed performance as filed as a patent application in [12].

Suppose a rotating disc, as shown on Fig. 35, of radius r_o with a particle of fluid **P** with perfect slip on its surface, i.e. the fluid particle does not wet the disc surface. The liquid drop **P** is released at time t = 0 from the position r = r_i in contact with the straight and smooth board attached to the disc, and with no relative velocity to it. The later is driven at a constant angular velocity ω about its vertical axis. Although in actuality the drum rotor oscillates about its transverse *x* and *y* axes, that orbiting planar motion will be neglected in this study since it is very small compared to the radial motion *r* described by the fluid particle **P** from its resting point to its final radial position. Furthermore, for the sake of simplicity, the axial motion of the fluid particle **P** will also be neglected.

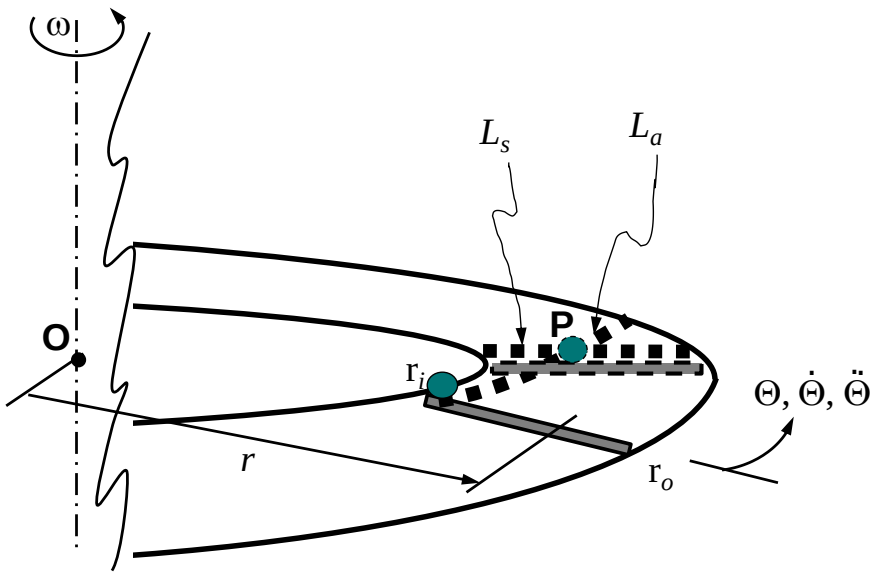

Figure 35. Rotating disc with a fluid particle on its surface and straight smooth board.

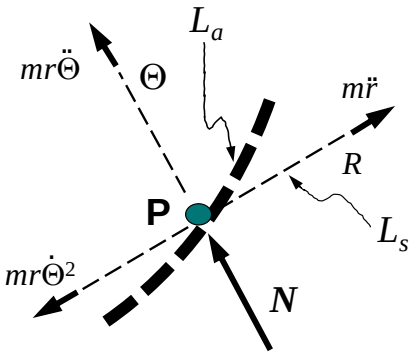

Figure 36. Free-body diagram of a fluid particle.

Problem formulation calls to establish the free-body diagram as depicted on Fig. 36. The molecule **P** departs from its resting point just at the onset of the curve L_a, where it intersects the circumference of radius r_i. As the motion begins, the particle **P** describes a curved absolute trajectory L_a to the outer ring wall, having at any given moment a

radial coordinate *R*, and an angular coordinate Θ, which will define its position at all times. On the other hand, ***N*** is defined as the normal force exerted by the baffle on the fluid particle **P**, which facilitates the relative trajectory of said particle along the baffle board until it reaches r_o. Finally, $\ddot{\Theta}$ is the transverse acceleration the rotor undergoes at the start-up until it reaches its steady-state condition. Let's now apply the second law of Newton to Fig. 36.

Second law of Newton applied in the *R*-coordinate lets arrive to

$$\Sigma F_r = 0 = m\mathrm{a}_r = m(\ddot{r} - r\dot{\Theta}^2) \tag{51}$$

This further reduces to

$$\ddot{r} = r\dot{\Theta}^2 = r\omega^2 \tag{52}$$

The solution of this differential equation in terms of hyperbolic sine and cosine is readily available in any book of differential equations [41]

$$r = A\sinh(\omega_r \mathrm{t}) + B\cosh(\omega_r \mathrm{t}) \tag{53}$$

The constants *A* and *B* are found from the initial conditions. These conditions are $r = r_i$ and $\dot{r} = 0$ at t = 0. The second condition comes from the fact that the particle has no

initial velocity relative to the board. Before evaluating this condition, r must be first differentiated with respect to time t.

$$\dot{r} = A\omega\cosh(\omega t) + B\omega\sinh(\omega t) \tag{54}$$

$$r(t = 0) = r_i = A\sinh(0) + B\cosh(0) = B \tag{55}$$

$$\dot{r}(t = 0) = 0 = A\omega\cosh(0) + B\omega\sinh(0) = A\omega \tag{56}$$

From the above, $B = r_i$ and $A = 0$. Hence,

$$r = r_i\cosh(\omega t) \tag{57}$$

The radial and transverse velocities and accelerations are found to be

$$v_R = \dot{r} = r_i\omega\sinh(\omega t) \tag{58}$$

$$v_\Theta = r\dot{\Theta} = r_i\omega\cosh(\omega t) \tag{59}$$

$$a_R = \ddot{r} = r\dot{\Theta}^2 = r_i\omega^2\cosh(\omega t) \tag{60}$$

$$a_\Theta = r\ddot{\Theta} + 2\dot{r}\dot{\Theta} = r_i\ddot{\Theta} + 2r_i\omega^2\sinh(\omega t) \tag{61}$$

The absolute path L_a of the particle is graphed using polar plotting on Fig. 37. For this r is needed as a function of Θ, since $\Theta = \omega t$, the angular trajectory r is equated to L_a, $r_i = 0.215$ m and $\omega = 70.162$ rad/s (670 rpm).

$$L_a = \mathrm{r}_i \cosh\Theta \tag{62}$$

On the other hand, the angle when the particle reaches r_o is given by

$$\Theta_o = \operatorname{acosh}\left(\frac{\mathrm{r}_o}{\mathrm{r}_i}\right) = \operatorname{acosh}\left(\frac{0.259\ \mathrm{m}}{0.215\ \mathrm{m}}\right) = 0.63\ \mathrm{rad} = 36\ \mathrm{deg} \tag{63}$$

Consequently, the acceleration in the *R*-direction of the particle **P** when it begins its motion and at Θ_o is calculated according to Eq. (64) and Eq. (65), respectively

$$\mathrm{a}_{Ri} = \mathrm{r}_i \omega^2 \cosh(\Theta_i) = 0.215\,\mathrm{m} \cdot (70.162\,\mathrm{rad/s})^2 \cosh(0\,\mathrm{rad}) = 1058\ \mathrm{m/s^2} \tag{64}$$

$$\mathrm{a}_{Ro} = -2\mathrm{r}_i \omega^2 \cosh(\Theta_o) = -2 \cdot 0.259\,\mathrm{m} \cdot (70.162\,\mathrm{rad/s})^2 \cosh(0.63\,\mathrm{rad}) = 1275\ \mathrm{m/s^2} \tag{65}$$

And the acceleration in the Θ-direction is

$$\begin{aligned} \mathrm{a}_{\Theta i} &= \mathrm{r}_i \ddot{\Theta} + 2\mathrm{r}_i \omega^2 \sinh(\Theta_i) = \\ &= 0.215\,\mathrm{m} \cdot 2.8\,\mathrm{rad/s^2} + 2 \cdot 0.215\,\mathrm{m} \cdot (70.162\,\mathrm{rad/s})^2 \sinh(0\,\mathrm{rad}) = 0.62\ \mathrm{m/s^2} \end{aligned} \tag{66}$$

$$\mathrm{a}_{\Theta o} = 2\mathrm{r}_i \omega^2 \sinh(\Theta_o) = -2 \cdot 0.259\,\mathrm{m} \cdot (70.162\,\mathrm{rad/s})^2 \sinh(0.63\,\mathrm{rad}) = 1424\ \mathrm{m/s^2} \tag{67}$$

Where the typical time for the basket rotor to reach its final steady-state speed (ω = 70.162 rad/s) is 25 s. Therefore, the rotor transverse acceleration at the machine

start-up is $\ddot{\Theta} = 2.8$ rad/s^2. Consequently, the transverse acceleration at the beginning of the particle motion ($a_{\Theta i}$) is due only to the motor start-up $r_i\ddot{\Theta}$. On the other hand, despite that the disc possesses a small angular acceleration ($\ddot{\Theta} = 2.8$ rad/s^2) at the start-up, the acceleration attained when the particle **P** reaches the ring outer wall amounts to 1424 m/s^2. This is because the baffle board makes the particle follow a curved absolute trajectory. Yet, the particle has no angular acceleration relative to the rotating disc.

The force of the particle **P** of mass m_p when it begins its motion and when it reaches r_o are given by Eq. (68) and Eq. (69), respectively

$$F_{si} = m_p a_{Ri} = 1058 \text{ m/s}^2 \text{ } m_p \tag{68}$$

$$F_{so} = m_p a_{Ro} = 1275 \text{ m/s}^2 \text{ } m_p \tag{69}$$

Equation (62) leads to confirm that although the path of the particle relative to the straight board is purely radial due to the normal force ***N***, the absolute trajectory for a fluid particle from rest to r_o is a curved one as described by L_a. Otherwise stated, the observed path followed by the particle **P**, as seen by a static observer, between the resting point of said particle and the outer wall of its container is not a straight line L_s, but a curve L_a. Figure 38 displays the radial and transverse velocities, the absolute magnitude of v_R is indicated in between bars to ease the curves comparison. Note that the fluid particle transverse velocity v_Θ increases linearly as the particle gets away from

the center **O**, whereas the radial velocity has a much smaller value, but a faster rate of increment though. Figure 39 in turn depicts the radial and transverse accelerations. The radial acceleration relates to the balancing capability of the fluid because it is directly proportional to the force the fluid exerts on the balance ring to oppose the rotor imbalance. Conversely, the transverse acceleration gives rise to the backward traveling wave discussed in Chapter IV.

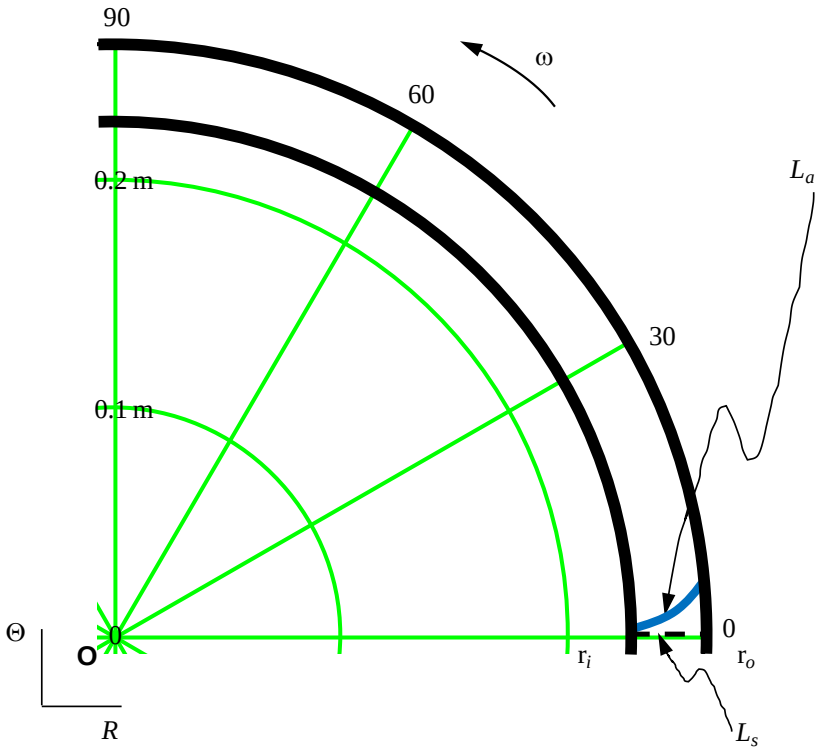

Figure 37. Polar plotting of the absolute path of a fluid particle.

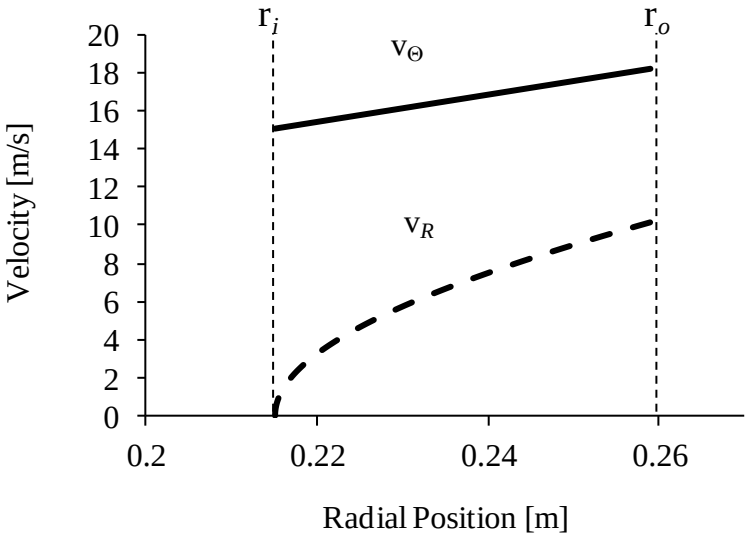

Figure 38. Radial and transverse velocities.

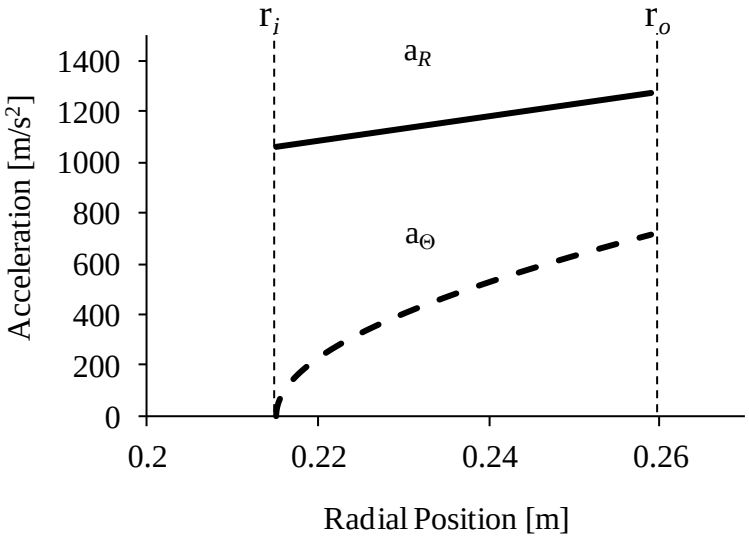

Figure 39. Radial and transverse accelerations.

Forward Blade Analysis

As has been demonstrated in the previous section, the absolute trajectory described by particle **P** when impelled by a straight baffle is a curve. In the light of the

above statement, it makes sense to believe that a possible way to improve the balance ring performance is to modify the straight baffle board to adopt the shape of a forward curved blade, such that the particle **P** acceleration, and in turn its force is modified when it begins its motion, and when it reaches the outer ring wall as well. In this scenario, as the particle **P** is impelled by a curved blade, its motion is observed from a coordinate system that is rotating. Therefore, it is more convenient to describe the motion of the particle **P** relative to a rotating coordinate system r-θ. In order to see how the rotation of the coordinate system affects the description of the motion, let **O'** be a particle on the disc rigid body that is rotating with angular velocity ω as shown on Fig. 40. Thus, the motion (position, velocity and acceleration) can be described at all times by the fixed R-Θ coordinate system. Further suppose that particle **P**, on the other hand, moves in a prescribed manner relative to the rotating disc rigid body. In defining the shape of the blade, the first logic choice is to make it identical to the curvature of the particle absolute trajectory **P** as defined by Eq. (57). Although it is easy to describe the motion of the particle **P** relative to the disc rotating body, it is not easy to describe its motion relative to the fixed R-Θ coordinate system. Instead, let r-θ be a rotating coordinate system that is attached to and rotates with the rigid body. Point **O'** will be chosen for the origin of the rotating coordinate system. The motion of points **O'** and **P** are somehow related but are not equal and are not on the same rigid body. Relative motion is conveniently specified giving the translational and rotational motion of the member containing the blade, the shape (curvature) of the blade, and the rate of travel of the particle **P** along the

blade. Then, in terms of this rotating coordinate system, the differential equation of motion in terms of the relative position angle θ on Fig. 40 is given by [42]

$$\mathbf{a}_{\mathrm{P}} = \mathbf{a}_{\mathrm{O'}} + \dot{\boldsymbol{\omega}} \times \mathbf{r}_{\mathrm{P/O'}} + \boldsymbol{\omega} \times (\boldsymbol{\omega} \times \mathbf{r}_{\mathrm{P/O'}}) + \mathbf{a}_{\mathrm{P\,rel}} + 2\boldsymbol{\omega} \times \mathbf{v}_{\mathrm{P\,rel}} \tag{70}$$

Where $\mathbf{a}_{\mathrm{O'}}$, $\mathbf{a}_{\mathrm{P}}$, $\boldsymbol{\omega}$, and $\dot{\boldsymbol{\omega}}$ are all measured relative to the fixed *R*-Θ coordinate system; $\mathbf{r}_{\mathrm{P/O'}}$, $\mathbf{v}_{\mathrm{Prel}}$, and $\mathbf{a}_{\mathrm{Prel}}$ are measured relative to the rotating *r*-θ coordinate system. The vectors in Eq. (70) must be expressed in a common reference system before the vectors sums and products can be performed. The acceleration of **O'** in the *R*-Θ coordinate system is described by

$$\mathbf{a}_{\mathrm{O'}} = (\mathbf{a}_{\mathrm{O'}})_R + (\mathbf{a}_{\mathrm{O'}})_\Theta = \mathrm{r}_o\omega^2\hat{e}_R + \mathrm{r}_o\dot{\omega}\hat{e}_\Theta \tag{71}$$

Translating $\mathbf{a}_{\mathrm{O'}}$ to the rotating coordinate system *r*-θ in accordance with Fig. 41(a), and knowing that $\dot{\omega} \neq 0$ at the machine start-up

$$\mathbf{a}_{\mathrm{O'}} = \mathrm{r}_o\omega^2(\cos\theta\hat{e}_r - \sin\theta\hat{e}_\theta) - \mathrm{r}_o\dot{\omega}(\sin\theta\hat{e}_r + \cos\theta\hat{e}_\theta) \tag{72}$$

Also

$$\dot{\boldsymbol{\omega}} \times \mathbf{r}_{\mathrm{P/O'}} = \dot{\omega}\hat{e}_k \times \mathrm{r}_p\hat{e}_r = \mathrm{r}_p\dot{\omega}\hat{e}_\theta \tag{73}$$

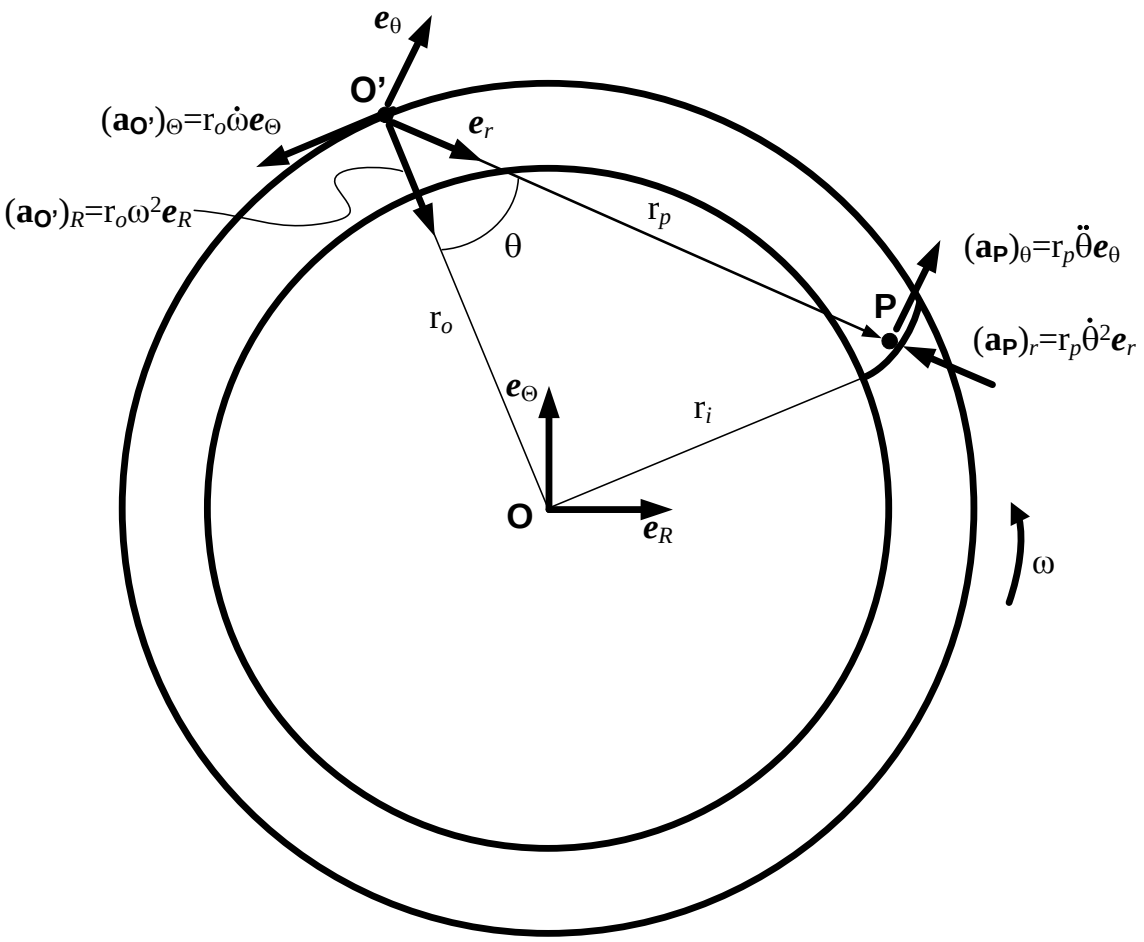

Figure 40. Relative motion diagram of particle **P** impelled by a forward curved blade.

Now the third term of Eq. (70) is

$$\boldsymbol{\omega}\times(\boldsymbol{\omega}\times\mathbf{r}_{P/O'}) = \omega\hat{e}_k\times(\omega\hat{e}_k\times r_p\hat{e}_r)$$

$$\boldsymbol{\omega}\times(\boldsymbol{\omega}\times\mathbf{r}_{P/O'}) = \omega\hat{e}_k\times(r_p\omega\hat{e}_\theta)$$

$$\boldsymbol{\omega}\times(\boldsymbol{\omega}\times\mathbf{r}_{P/O'}) = -r_p\omega^2\hat{e}_r \qquad (74)$$

The relative velocity and acceleration are defined as

$$\mathbf{a}_{\mathrm{P\,rel}} = (\mathbf{a}_{\mathrm{P}})_r + (\mathbf{a}_{\mathrm{P}})_\theta = -\mathrm{r}_p\dot{\theta}^2\hat{e}_r + \mathrm{r}_p\ddot{\theta}\hat{e}_\theta \tag{75}$$

$$\mathbf{v}_{\mathrm{P\,rel}} = \dot{\mathrm{r}}_p\hat{e}_r + \mathrm{r}_p\dot{\theta}\hat{e}_\theta \tag{76}$$

So the fifth term of Eq. (70) is

$$2\boldsymbol{\omega}\times\mathbf{v}_{\mathrm{P\,rel}} = 2\omega\hat{e}_k\times(\dot{\mathrm{r}}_p\hat{e}_r + \mathrm{r}_p\dot{\theta}\hat{e}_\theta)$$

$$2\boldsymbol{\omega}\times\mathbf{v}_{\mathrm{P\,rel}} = 2\dot{\mathrm{r}}_p\omega\hat{e}_\theta - 2\mathrm{r}_p\omega\dot{\theta}\hat{e}_r \tag{77}$$

Substituting Eqs. (72-75) and Eq. (77) into Eq. (71) renders

$$\mathbf{a}_{\mathrm{P}} = (\mathrm{r}_o\omega^2\cos\theta - \mathrm{r}_p\omega^2 - \mathrm{r}_p\dot{\theta}^2 - 2\mathrm{r}_p\omega\dot{\theta} - \mathrm{r}_o\dot{\omega}\sin\theta)\hat{e}_r$$
$$+(\mathrm{r}_p\ddot{\theta} - \mathrm{r}_o\omega^2\sin\theta + 2\dot{\mathrm{r}}_p\omega + \mathrm{r}_p\dot{\omega} - \mathrm{r}_o\dot{\omega}\cos\theta)\hat{e}_\theta \tag{78}$$

Since there is no force in the $\boldsymbol{e}_\theta$-direction $(\mathbf{a}_{\mathrm{P}})_\theta = 0$. Hence

$$\mathrm{r}_p\ddot{\theta} - \mathrm{r}_o\omega^2\sin\theta + 2\dot{\mathrm{r}}_p\omega + \mathrm{r}_p\dot{\omega} - \mathrm{r}_o\dot{\omega}\cos\theta = 0$$

$$\ddot{\theta} = \frac{\mathrm{r}_o}{\mathrm{r}_p}\omega^2\sin\theta - 2\frac{\dot{\mathrm{r}}_p}{\mathrm{r}_p}\omega\mathrm{r}_p - \dot{\omega} + \frac{\mathrm{r}_o}{\mathrm{r}_p}\dot{\omega}\cos\theta \tag{79}$$

Inspection of Fig. 41(b) lets state that at t = 0; θ_i = atan(r_i / r_o), r = r_i, and $\dot{\theta}(\theta_i) = 0$

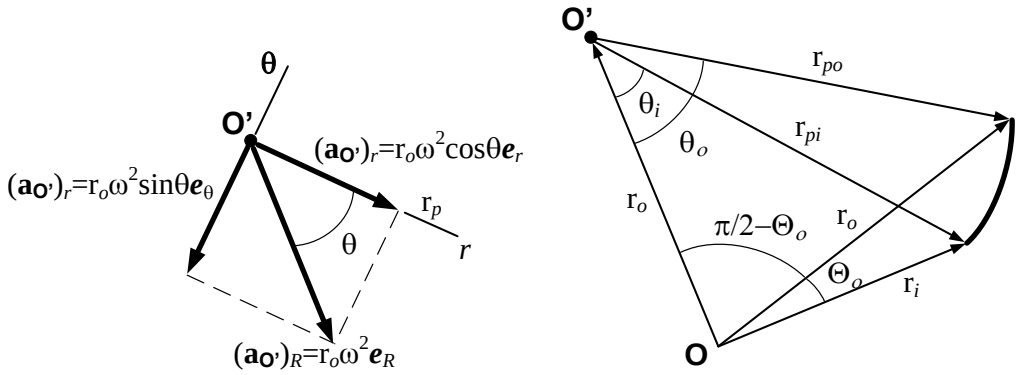

(a) (b)

Figure 41. Transposition to the rotating coordinate system *r*-θ; (a) absolute radial acceleration of **O'**, and (b) radial position of leading and trailing edge of curved blade.

Given that the angular acceleration is known as a function of angular position instead of time, then using the chain rule of differentiation delivers

$$\ddot{\theta}(\theta) = \frac{d\dot{\theta}}{dt} = \frac{d\dot{\theta}}{d\theta}\frac{d\theta}{dt} = \dot{\theta}\frac{d\dot{\theta}}{d\theta}$$

Then, Eq. (79) becomes

$$\ddot{\theta} = \dot{\theta}\frac{d\dot{\theta}}{d\theta} = \frac{r_o}{r_p}\omega^2\sin\theta - 2\frac{\dot{r}_p}{r_p}\omega - \dot{\omega} + \frac{r_o}{r_p}\dot{\omega}\cos\theta$$

Integrating between boundary conditions

$$\int_0^{\dot{\theta}} \dot{\theta} d\theta = \int_{\theta_i}^{\theta} \left[\frac{r_o}{r_p} \omega^2 \sin\theta - 2 \frac{\dot{r}_p}{r_p} \omega - \dot{\omega} + \frac{r_o}{r_p} \dot{\omega} \cos\theta \right] d\theta$$

$$\frac{1}{2} \dot{\theta}^2 = \frac{r_o}{r_p} \omega^2 (\cos\theta_i - \cos\theta) - 2 \frac{\dot{r}_p}{r_p} \omega (\theta_i - \theta) - \dot{\omega} (\theta_i - \theta) + \frac{r_o}{r_p} \dot{\omega} (\sin\theta_i - \sin\theta)$$

$$\cos\theta = \cos\theta_i - \frac{r_p}{r_o \omega^2} \left\{ \frac{1}{2} \dot{\theta}^2 + \left[2\omega \frac{\dot{r}_p}{r_p} + \dot{\omega} \right] (\theta_i - \theta) - \frac{r_o}{r_p} \dot{\omega} (\sin\theta_i - \sin\theta) \right\}$$

But

$$\cos\theta_i = \cos\left(\operatorname{atan} \frac{r_i}{r_o} \right) = \left(\left(\frac{r_i}{r_o} \right)^2 + 1 \right)^{-0.5}$$

Then

$$\cos\theta = \left[\left(\frac{r_i}{r_o} \right)^2 + 1 \right]^{-0.5} - \frac{r_p}{r_o \omega^2} \left\{ \frac{1}{2} \dot{\theta}^2 + \left[2\omega \frac{\dot{r}_p}{r_p} + \dot{\omega} \right] (\theta_i - \theta) - \frac{r_o}{r_p} \dot{\omega} (\sin\theta_i - \sin\theta) \right\}$$

On the other hand, the force F_{fw} of the particle **P** of mass m_p impelled by a forward blade is

$$\mathbf{F}_{fw} = F_r \hat{e}_r = m_p \mathbf{a}_r$$

Taking $\mathbf{a}_r$ from Eq. (78)

$$F_{fw} = m_p a_r = m_p \left[r_o \omega^2 \cos\theta - r_p \omega^2 - r_p \dot{\theta}^2 - 2 r_p \omega \dot{\theta} - r_o \dot{\omega} \sin\theta \right]$$

At $\theta = \theta_i$; $r_p = r_{pi}$, $\dot{\theta} = 0$, and $\dot{\omega} = \ddot{\Theta}$, then

$$\cos\theta_i = \left[\left(\frac{r_i}{r_o}\right)^2 + 1\right]^{-0.5} \tag{80}$$

which leads back to the trigonometric identity, confirming that the initial conditions are well established

On the other hand, at $\theta = \theta_o$; $r_p = r_{po}$, $\dot{\theta} = \omega$, $\dot{\omega} = \ddot{\Theta}$, and $\dot{r}_p = \dot{r}_{po}$. Consequently

$$\cos\theta_o = \left[\left(\frac{r_i}{r_o}\right)^2 + 1\right]^{-0.5} - \left\{\frac{r_{po}}{2r_o} + \left[\frac{2\dot{r}_{po}}{r_o\omega} + \frac{r_{po}}{r_o\omega^2}\ddot{\Theta}\right](\theta_i - \theta_o) - \frac{\ddot{\Theta}}{\omega^2}(\sin\theta_i - \sin\theta_o)\right\} \tag{81}$$

Also, from trigonometric identities

$$\sin\theta_i = \sin\left(\operatorname{atan}\frac{r_i}{r_o}\right) = \frac{r_i}{r_o}\left(\left(\frac{r_i}{r_o}\right)^2 + 1\right)^{-0.5}$$

Therefore

$$F_{fwi} = m_p a_{ri} = -m_p r_i \dot{\omega}\left[\left(\frac{r_i}{r_o}\right)^2 + 1\right]^{-0.5} \tag{82}$$

$$F_{fwo} = m_p a_{ro} = m_p \left\{ r_o \omega^2 \left[\left[\left(\frac{r_i}{r_o} \right)^2 + 1 \right]^{-0.5} - \left[\frac{r_{po}}{2r_o} + \left(\frac{2\dot{r}_{po}}{r_o \omega} + \frac{r_{po}}{r_o \omega^2} \ddot{\Theta} \right) (\theta_i - \theta_o) \right. \right. \right. \quad (83)$$

$$\left. \left. \left. - \frac{\ddot{\Theta}}{\omega^2} (\sin\theta_i - \sin\theta_o) \right] \right] - 4 r_{po} \omega^2 + r_o \ddot{\Theta} \sin\theta_o \right\}$$

Using Fig. 41(b), r_{pi} is easily obtained from Pythagoras theorem, whereas r_{po} is obtained by the law of cosines as follows

$$r_{pi} = \left(r_o^2 - r_i^2 \right)^{0.5} = \left[(0.259\ \text{m})^2 - (0.215\ \text{m})^2 \right]^{0.5} = 0.337\ \text{m} \quad (84)$$

$$r_{po} = \left[2r_o^2 - 2r_o^2 \cos\left(\frac{\pi}{2} - \Theta_o \right) \right]^{0.5} = \left[2(0.259\ \text{m})^2 - 2(0.259\ \text{m})^2 \cos\left(\frac{\pi}{2} - 0.36 \right) \right]^{0.5}$$

$$r_{po} = \left[2r_o^2 - 2r_o^2 \cos\left(\frac{\pi}{2} - \Theta_o \right) \right]^{0.5} = 0.235\ \text{m} \quad (85)$$

Also, the θ_i and θ_o can be computed as

$$\theta_i = \text{atan}\left(\frac{r_i}{r_o} \right) = 0.693\ \text{rad} = 39.7\ \text{deg} \quad (86)$$

$$\theta_o = \text{acos}\left(\frac{r_p^2}{2 r_o r_{po}} \right) = 1.1\ \text{rad} = 63\ \text{deg} \quad (87)$$

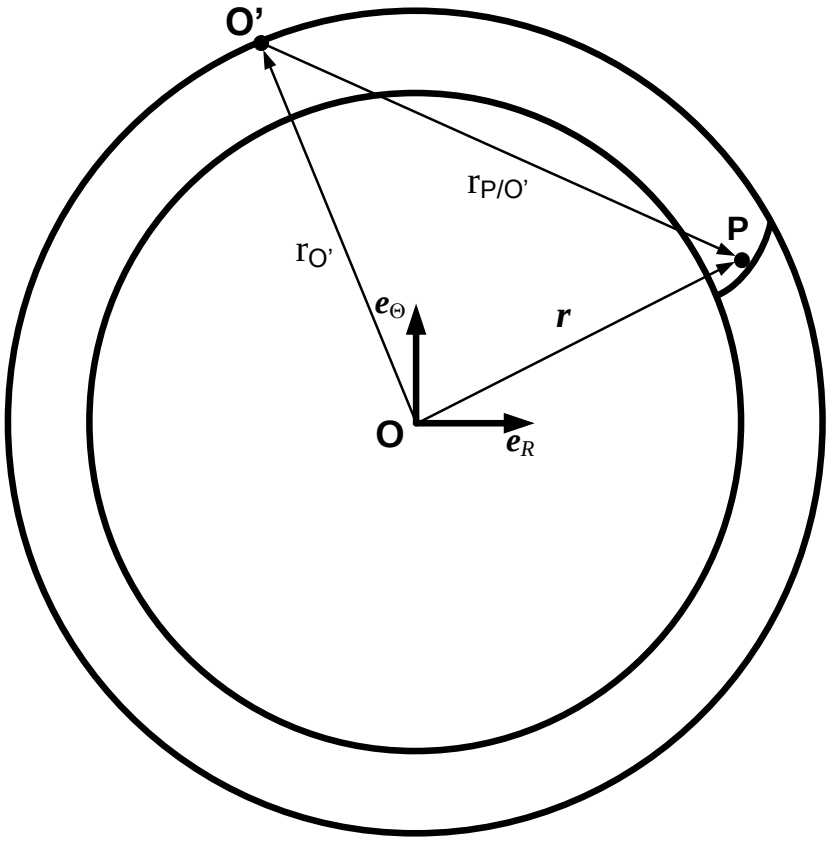

Figure 42. Displacement vectors triangle.

According to Fig. 42, the absolute velocity vectors in the *R*-Θ coordinate system are related by $\dot{r} = \dot{\mathbf{r}}_{O'} + \dot{\mathbf{r}}_{P/O'}$ .Then, at $\theta = \theta_o$; $\dot{\boldsymbol{r}}_o = \dot{\mathbf{r}}_{O'} + \dot{\mathbf{r}}_{po}$, knowing that $\dot{r}_{O'} = 0$, then $\dot{\boldsymbol{r}}_o$ $\dot{\mathbf{r}}_{po} = \dot{\boldsymbol{r}}_o$ when the particle reaches the outer ring wall.

The velocity of the particle **P** at θ_o can be calculated according to Eq. (59) delivering

$$\dot{r}_{\boldsymbol{po}} = r_i \omega \sinh(0) = 0.215 \text{ m} \times 70.162 \text{ rad/s} \times \sinh(0.63) = 10.14 \text{ m/s} \qquad (88)$$

Substituting Eq. (84) into Eq. (82) yields the particle force at the beginning of its motion

$$F_{fwi} = -0.463 \text{ m/s}^2 \text{ m}_p \approx 0 \tag{89}$$

Also, substituting Eqs. (85-88) into Eq. (83) delivers the particle force when it reaches r_o as Eq. (90)

$$F_{fwo} = 3239 \text{ m/s}^2 \text{ m}_p \tag{90}$$

Backward Blade Analysis

As stated by the third law of Newton, in the absence of the straight board and the imposed normal force ***N***, the natural trajectory of the fluid particle would backwards relative to the disc sense of rotation and still following a curved trajectory. Therefore, another important case of study is to introduce a backward blade. In this scenario, the equation of motion Eq. (70) still holds, but to ease the analysis the velocity vector will be inverted in direction as indicated by Eq. (91), such that the blade in Fig. 40 will act backwards with respect to the sense of rotation. Appendix D provides the analysis in detail; the more important equations are discussed following.

$$\boldsymbol{\omega} = -\omega \hat{\boldsymbol{e}}_k \tag{91}$$

The force F_{bw} of the particle **P** of mass m_p impelled by a backward blade is

$$F_{bw} = m_p a_r = m_p \left\{ r_o \omega^2 \left[\frac{r_o}{r_p} \left[\left(\frac{r_i}{r_o} \right)^2 + 1 \right]^{-0.5} - \frac{r_o}{2r_p} \right] \right\} \tag{92}$$

Equation (92) yields the particle force for both, at the beginning of its motion and when it reaches r_o as Eq. (93) and Eq. (94), respectively

$$F_{bwi} = m_p a_{ri} = m_p \left[\left(\frac{r_i}{r_o} \right)^2 + 1 \right]^{-0.5} \left(r_o \omega^2 + r_i \dot{\omega} \right) = 981 \text{ m/s}^2 \ m_p \tag{93}$$

$$F_{bwo} = m_p a_{ro} = m_p \left\{ r_o \omega^2 \left[\left[\left(\frac{r_i}{r_o} \right)^2 + 1 \right]^{-0.5} - \left[\frac{r_{po}}{2r_o} + \left(\frac{2\dot{r}_{po}}{r_o \omega} + \frac{r_{po}}{r_o \omega^2} \ddot{\Theta} \right) (\theta_i - \theta) \right. \right. \right. \tag{94}$$

$$\left. \left. \left. + \frac{\ddot{\Theta}}{\omega^2} (\sin\theta_i - \sin\theta_o) \right] \right]^2 + r_o \ddot{\Theta} \sin\theta_o \right\} = 982 \text{ m/s}^2 \ m_p$$

Discussion

The results of the studied cases are put together in Table 4. The forces at the beginning and at the end of the particle **P** radial motion are deemed as the transient-state force, and steady-state force, respectively. Note that the ratios of the forward and backward blade force cases to the straight baffle force case are included in brackets on Table 4.

Table 4. Straight vs curved blades force.

Case	Transient Force/m_p [ratio]	Steady-State Force/m_p [ratio]	Comments
Straight baffle	2117 [1]	2551 [1]	Baseline
Forward blade	0 [0]	3239 [1.27]	Better for transient-state
Backward blade	981 [0.46]	982 [0.39]	Better for steady-state

Units are (N/kg)

The transient force ratio of the forward blade case amounts to 0 with respect to the baseline case, meaning that this kind of blade cancels the particle **P** acceleration, which in turn causes the transient-state fluid force to be null. In other words, it is expected that the forward blade will exert a much smaller impelling force on the particle **P** at the machine start-up than the straight baffle case, which may be good for the balance ring performance. Since the forward blade force in the transient-state reduces, thus less unbalance load is added below the system natural frequency (only the garments load), in that way improving the washing machine dynamics.

On the other hand, the forward blade increases by 27% the exerted force of the particle **P** on the ring outer wall, this may cause a problem with the system dynamics in the steady-state regime, particularly so because the balance ring adds force on the upper part of the rotating basket, contributing in this way to augment the dynamic moments around the system **C.G.** and therefore increase the displacements on the top part of the basket.

An interesting reduction on the acceleration the backward blade imposes to the particle **P** at the machine start-up is shown. This means that the particle **P** is refrained by the backward blade, which because of its curvature holds back the fluid. This situation may introduce problems in the transient performance making it last longer.

Finally, the backward blade evidences a reduced particle **P** force in the steady-state case, which is very homogeneous with its transient-state counterpart. Furthermore, the experiments indicate that the backward blade has better performance in the steady-state regime showing lower rotating basket displacements, this might be the result of lower dynamic moments in the system.

CHAPTER X

EXPERIMENTS WITH STRAIGHT AND CURVED BLADES

Prototype

Due to convention, the blades that follow the spin direction of ω adopting a curved shape L_a, given by Eq. (62), will be known as forward curved blades. Antagonistically, the backward curved blades follow a negative trajectory of L_a, that is; the equation used to describe the trajectory L_a is multiplied by –1 on the right-hand side. Thus, the curvature is reversed producing a mirror function of L_a. The straight baffle is simply a radial board with neither a forward nor a backward curvature. Figure 43 displays the notation employed for the blades identification.

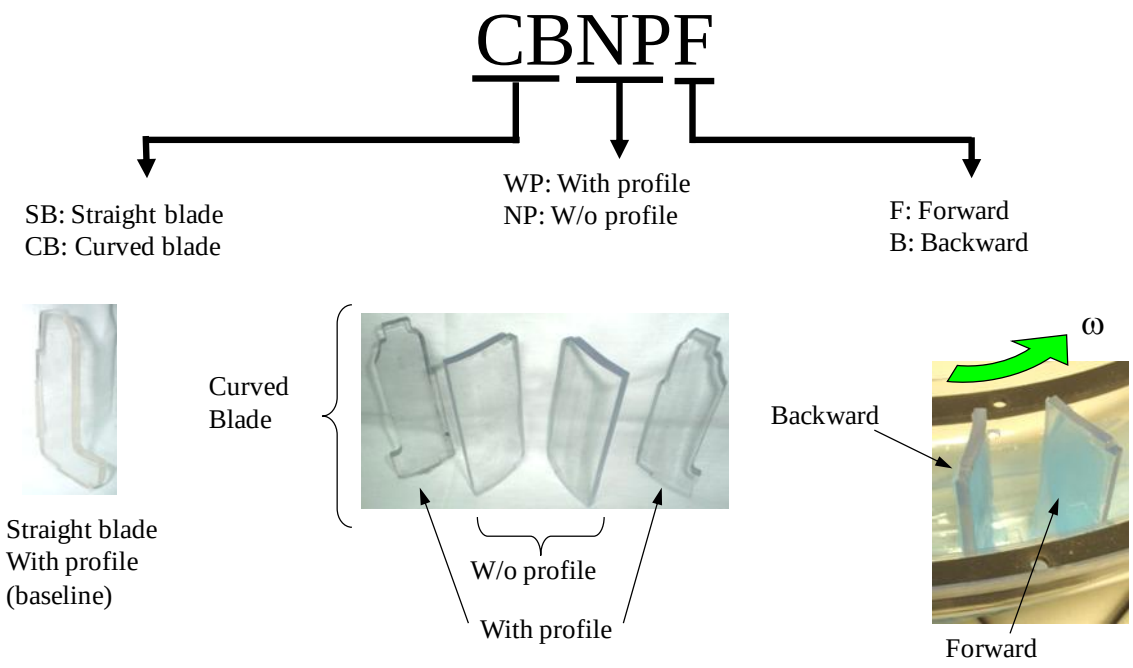

Figure 43. Blades nomenclature.

A versatile prototype made of Polyethylene Terephthalate (PET) was build for testing different types of blades. Fig. 44(a) shows the 3D design of the bladed balance ring, Fig. 44(b) shows a photograph of the mold, and Fig. 44(c) illustrates the experimental ring. The bottom part of the ring houses the baffles, which are put in place by being inserted in machined guiding grooves according to the blade curvature. The upper part works as a top cover bolted to the bottom portion. In between, there is an open cell gasket aimed to prevent fluid leakage. The balance ring assembly is rigidly mounted on top of the rotating basket through a set of brackets.

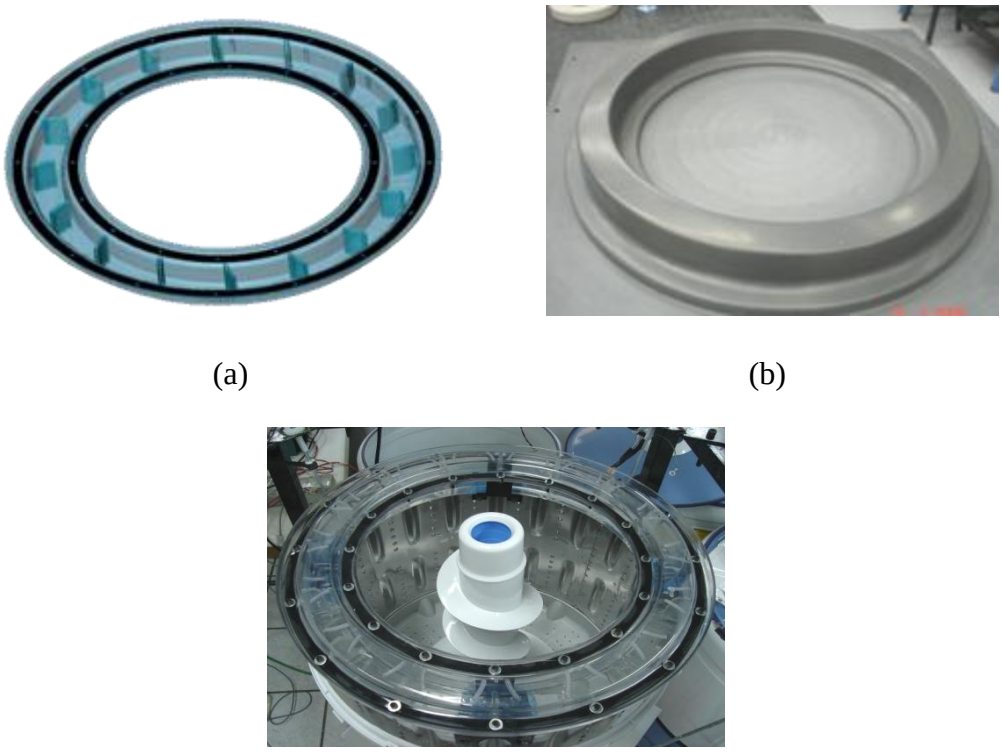

(a) (b)

(c)

Figure 44. Prototype balance ring; (a) Design in 3D, (b) mold, and (c) experimental PET prototype (courtesy of *mabe S.A. de C.V.*).

Measurements of vibration

Vibration measurements were recorded using laser transducers as described on Chapter III running at 490 rpm to avoid basket-tub rubbing. Figure 45 shows the obtained results in colored bars graph format. Experiments were carried out with an unbalance load of 1.5 kg.

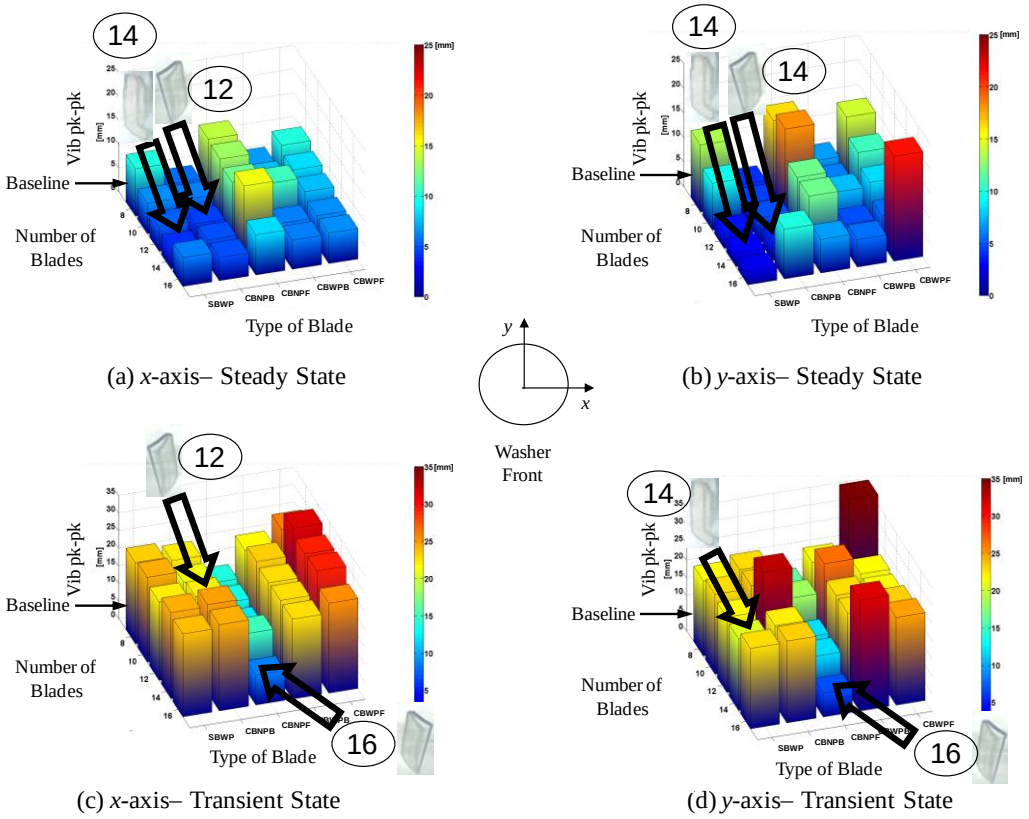

Figure 45. Vibration measurements with bladed balance ring; (a) *x*-axis steady-state, (b) *y*-axis steady-state, (c) *x*-axis transient-state, and (c) y-axis transient-state.

Note that increasing the number of straight blades contribute to improve dynamic performance in the steady-state, but do very little to make the transient-state response better. Best choices as per steady-state performance are obtained for:

- SBWP with 14 baffles (SBWP14).
- CBNPB with 12 blades (CBNPB12).

Although, SBWP14 and CBNPB12 reduce steady-state displacements in between 50 and 60%, respectively, they do nothing to improve displacements in the transient-state. Furthermore, CBNPB12 worsens displacements in the *y*-axis by 40%. Therefore, the best choice as per transient performance is obtained for:

- CBNPF with 16 blades (PCNPF16).

PCNPF16 reduces transient-state displacements around 50%, but does little to improve displacements for the steady-state.

Correlation

The experimental results confirm the analysis presented on Chapter IX, which predicted the forward blades to be suited for the transient-state, meanwhile the backward blades are the preferred choice for the steady-state regime. A simple free-body diagram allows the calculation of the steady-state dynamic moment acting on the **C.G.** of the

wash unit. Figure 46 depicts a cross-section of a vertical-axis washing machine, where x_1 = 0.258 m, x_2 = 0.108 m, F_f is computed from Eq. (2) as 606 N, and finally the unbalance force U is provided in Fig. 29 and amounts to 1381 N. Table 5 reports the theoretical resultant forces and dynamic moments.

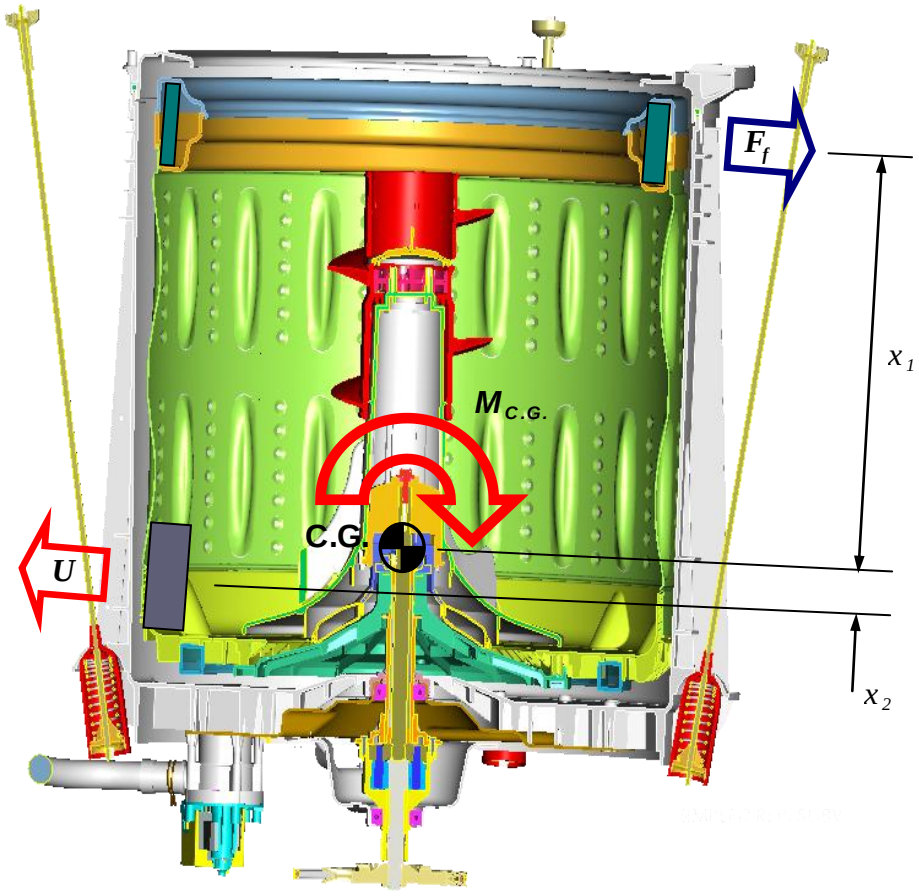

Figure 46. Free-body diagram of a vertical-axis washing machine (courtesy of *mabe S.A. de C.V.*).

Table 5. Straight vs curved blades theoretical resultant forces and dynamic moments.

Case	Steady-State Resultant Force [ratio]	Steady-State Dynamic Moment [ratio]	Comments
Straight baffle	–775 [1]	350 [1]	Baseline
Forward blade	–611 [0.79]	392 [1.12]	Better for transient-state
Backward blade	–1145 [1.48]	255 [0.73]	Better for steady-state

Units are (N and N-m)

Table 6 shows displacement ratios for the CBNPB and CBNPF for a variety of number of blades.

Table 6. Steady-state displacements ratios.

Case	Ratio to SBWP8 *x*-axis	Ratio to SBWP8 *y*-axis	Case	Ratio to SBWP8 *x*-axis	Ratio to SBWP8 *y*-axis
CBNPB8	0.6	0.5	CBNPB8	1.5	1.3
CBNPB10	0.55	0.5	CBNPB10	1.3	1.5
CBNPB12	0.6	0.6	CBNPB12	1.1	1.1
CBNPB14	0.6	0.3	CBNPB14	1.9	1.1
CBNPB16	0.6	0.8	CBNPB16	0.8	0.7
Average	0.6		Average	1.2	

Dimensionless

It is worth mentioning that the average of the measured steady-state displacements for CBNPB (8, 10, 12, 14, and 16 backward blades) has a ratio of 0.6 with respect to baseline (SBWP8) as reported on Table 6, meanwhile the theoretical dynamic moment ratio of the backward blade to the straight baffle case has a value of 0.73 as indicated in Table 5. The causality of vibration on top of the rotating basket as a result of

the dynamic moments allows establishing a fairly good correlation. Conversely, the averaged measured steady-state displacements for CBNPF (8, 10, 12, 14, and 16 forward blades) has a ratio of 1.2 with respect to baseline (SBWP8). While the increased force provided by the forward blades results in a theoretical dynamic moment of 1.12 times the baseline (SBWP8). The agreement again in between predictions and experiments is very good in this situation.

An optimized balance ring design must perform well for transient, as well as the steady-state. It has been theoretically and experimentally demonstrated that the forward blade performs better for the transient-state by almost cancelling the fluid radial acceleration. In other words, as the rotor starts up, the fluid tends to slosh and plaster towards the ring outer wall in the same direction than the ring displacement, thus adding and unbalance load. The rotating basket rocks due to this added unbalance and the entire washing system can describe large excursion, such that the tub collides with the cabinet structure. This transient behavior is alleviated if the fluid radial acceleration is cancelled at the machine start-up by employing a forward blade. The use of a forward blade worsens the system steady-state though. Since the forward blade accelerates too much the fluid in this case because it follows the rigid body rotation, then a large fluid force develops and for instance a dynamic moment that causes alternating displacements or vibration. On the contrary, the aim of a backward blade is to enhance the system response above its first natural frequency, i.e. in the steady-state. The backward blade reduces the radial acceleration of the fluid because the curvature of such blade is

opposing the rigid body rotation. This is good for the dynamics of the system as the centrifugal force is reduced, also the dynamic flexural moment around the system **C.G.**, and hence the rotor vibrations in the steady-state are reduced. Nonetheless, the backward blade does little to improve the system response in the transient-state.

An improved design should merge the advantages of both kinds of blades (forward and backward), while minimizing its disadvantages. The hypothesis for arriving to a better bladed balance ring version is to alternate the forward and backward blades to be placed inside the ring cavity. A balance ring accounting with combined blades should minimize displacements in the transient and steady state. The approach should focus on obtaining the best possible combination of forward and backward blades. Note that the blades should not account with profile since it is not in the best options for neither, the transient not the steady-state.

Improved design

Figure 47(a) shows an isometric ghost view of the inner geometry of a forward blade [12]. The forward blade originates at the inner wall of smallest diameter and extends following the curve L_a to the inner wall of greatest diameter leaving a radial gap between the blade and the inner wall of greatest diameter for the fluid circumferential flow. Figure 47(b) shows that there is also a vertical gap allowing the axial fluid wave component to flow into the chambers delimited by the baffles [12].

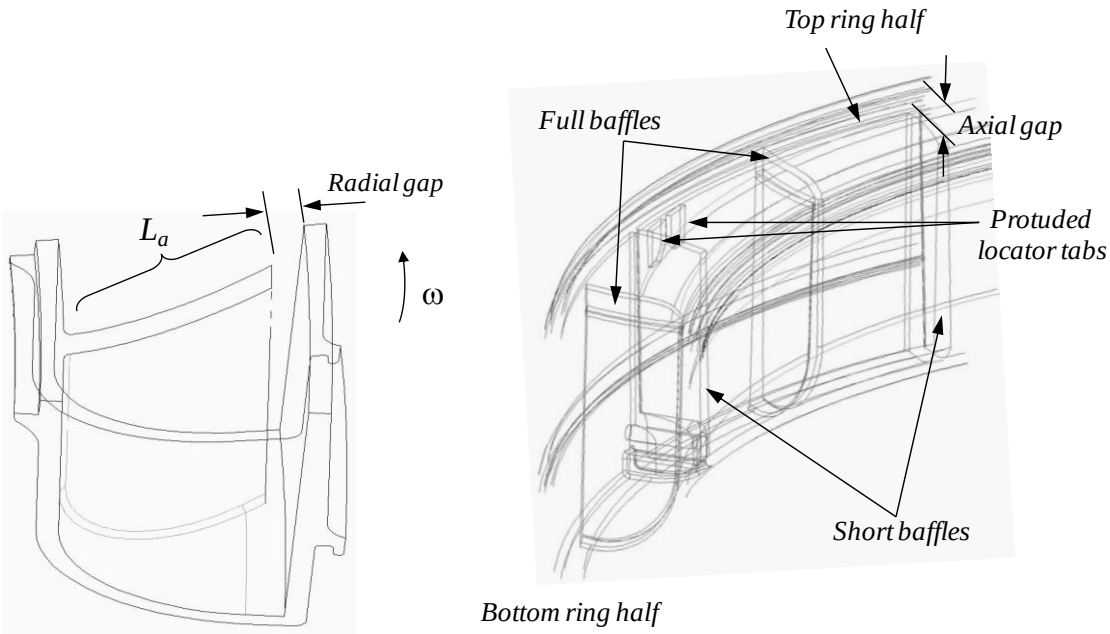

Figure 47. Isometric ghost view of; (a) inner geometry of a forward blade, and (b) alternated baffles of different height, (courtesy of *mabe S.A. de C.V.*).

However, full blades extending from the bottom to the top part of the ring cavity have been also introduced to weaken this axial fluid component. In doing this, the fluid balancing force is expected to increase because the unbalance response phase lag introduced by the fluid backward traveling wave (Fig. 29) will be minimized. In one example embodiment of the invention [12], the raised blade is shaped by a bottom blade portion. The full blade is complemented with a protuberance formed on the inner side of the top half of the ring, so the top side of the blade connects with the bottom side of the blade complementing a full blade; see Fig. 47(b).

In an alternative embodiment, the blade complement may be shorter, allowing thereby the passage of the working liquid to flow in its axial component. The same effect, or a very similar one, may be obtained by constructing blades of at least two diverse sizes, or by constructing the blade complement in at least two diverse sizes. The blades substantially block the circumferential component of the flow of the working liquid, understanding that in an alternative embodiment the full blades do allow the flow of working liquid to have a circumferential component by having an opening between the full blade and the inner wall (inner radial gap), or between the blade complement (outer radial gap). The decision on whether the axial gap is used or not into the balance ring design, will depend on the aim of the balance ring, whether as a balancing device with no axial gap (Chapter VI) or as a stability mechanism with axial gap (Chapter VIII).

To ease the assembly of the bottom ring half with the top ring half, a locator was devised that, in a descriptive but not limitative manner in order to describe better the optimum way to execute the invention [12], consists of a pair of protruded tabs extending down from the inner side of the upper half, which can be seen in Fig. 47(b). Because the tabs fit only on short blades, they allow the localization and guidance of the upper part of blade in a poka-yoke kind of assembly. This permits the ring top half always to keep a correct position with the bottom half at the time of assembling, thus avoiding localization mistakes that may cause a malfunction of the balance ring.

Figure 48 is useful to identify the different types of bladed balance rings designed from the lessons learned in the theoretical and experimental analysis. Since the bottom ring half may house different types of blades, two different designs have been developed, namely; an arrangement of 12 forward blades combined with 12 backward blades and another arrangement of 12 forward blades combined with 12 straight baffle boards [12].

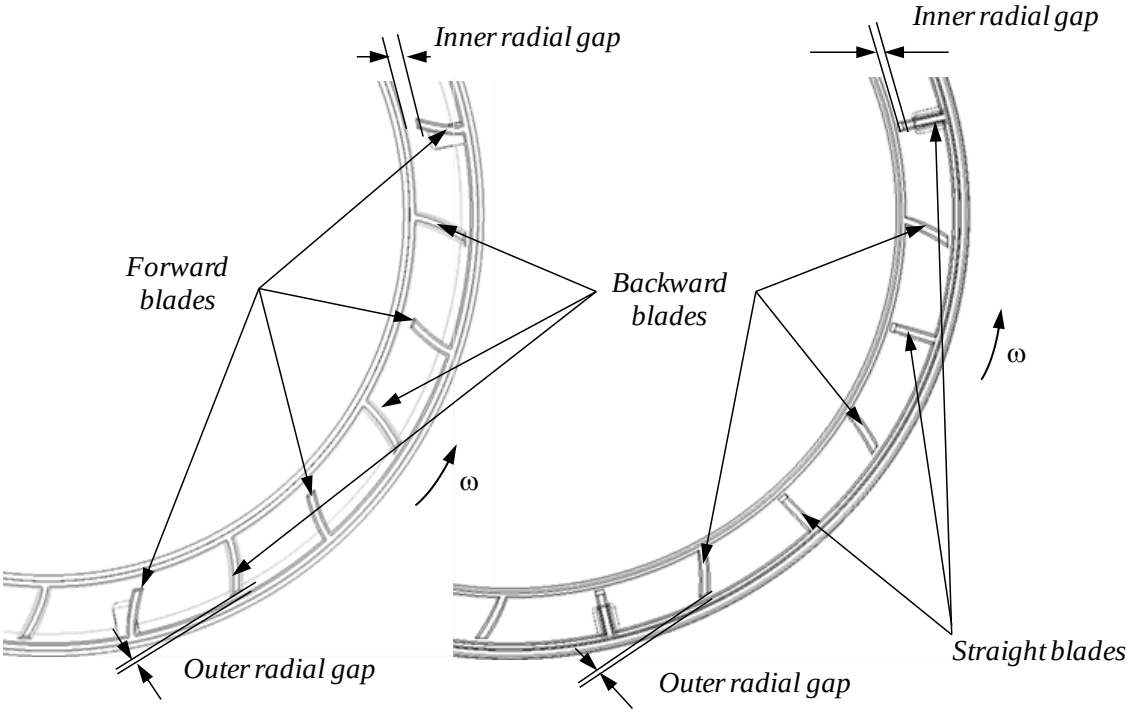

Figure 48. Improved designs arrangements; (a) forward and backward blades (BR1), and (b) forward blades and straight baffles (BR2), (courtesy of *mabe S.A. de C.V.*).

Hereinafter, the first design will be named as bladed ring 1 (BR1), while the second design will be regarded as bladed ring 2 (BR2). In both cases, the blades accounting with inner radial gap, also have an axial gap with the top ring half.

Conversely, the blades having an outer radial gap are of full type, i.e. extend fully from the bottom to the upper half, and therefore account with no axial gap. Both rings were machined from High-Density Polyethylene (HDPE) thermoplastic.

Confirmatory results

The washing machine was installed in a flat mosaic floor for performing the vibration experiments. This time, in an effort to have closer reference to what the user may feel or perceive, the vibration effects of the different balance rings designs on the structure were measured. This provides the ulterior perception of the user about the product as shown on Fig. 49. Furthermore, given that the new machined balance ring prototypes (BR1 an BR2) can be assembled in the washing machine without need of modifications to the tub, the unit was able to run at a speed of 880 rpm with no tub-basket rubbing.

Figure 49. Experimental array for measurements of vibration on the cabinet structure.

The vibration was measured on the front and left side of the structure at the corresponding height of the balance ring location as projected on the cabinet. This location was chosen for two main reasons. Firstly, it is easier to directly measure a collision of the wash unit against the cabinet. Secondly, get rid as much as possible of the membrane behavior of the cabinet thin sheet metal. Banner LG® series laser short-range precision displacement transducers with a resolution of 10 μm were employed. The laser transducers were supported by the nylamid rack (described on Chapter III) designed to surround the rigid frame shown on Fig. 49. The transducers were installed 0.1 m away from the target surface. A NI PXI 4472 DAQ system used to collect data

during the experiments. The signals provided by the laser transducers are displayed on Fig. 50 and 51 for the front and left side, respectively.

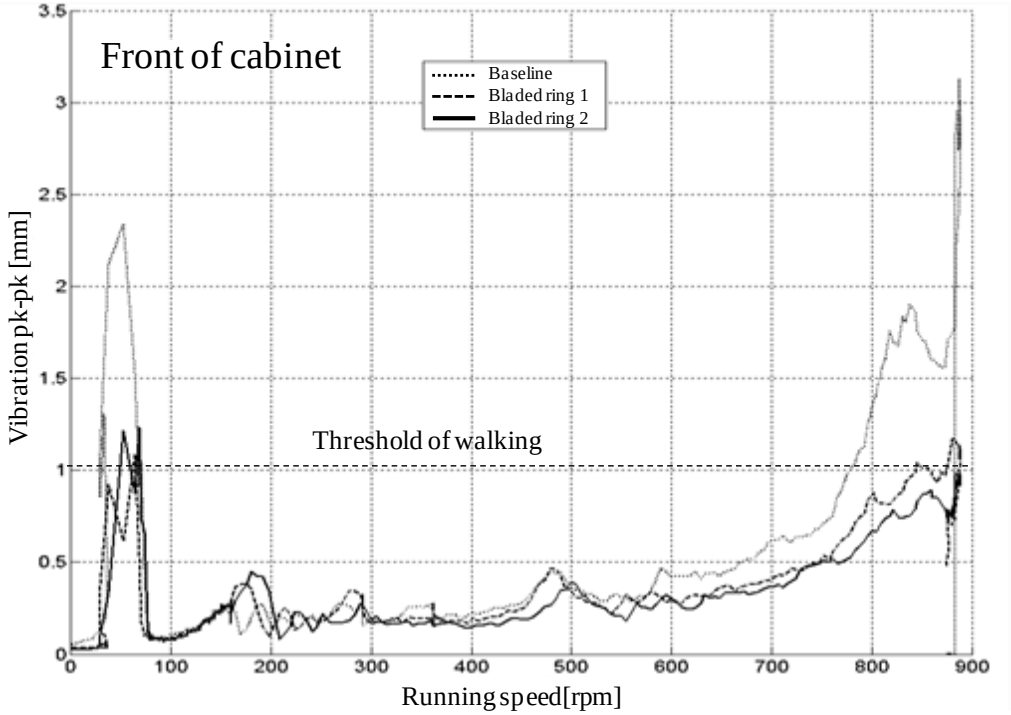

Figure 50. Measurement of vibration on the front of the cabinet structure.

Experiments were carried out with a load of 2 kg, which is considered a very high unbalance load. Figure 50 shows the vibration measured on the front part of the cabinet for three different cases, baseline, BR1 and BR2. In this graph, the threshold for detecting walking is close to 1 mm, that is, for a given angular velocity, if the peak-to-peak vibration is over 1 mm, the washing machine will tend to randomly move in some direction and walk. The curve represented by the points is the baseline, i.e. a conventional balance ring, which employs straight radial baffles. Notice that below 100

rpm, there is a sudden peak greater than 2 mm due to the start up and consequent fluid sloshing. Afterwards, in between 100 and 600 rpm, all curves are close one another. Note that the washing machine natural frequency is traversed just below 200 rpm. Later, above 600 rpm the baseline vibration curve separates from the others, this indicates that the design of a conventional balance ring does not withstand high rpm. As the chart shows, above 800 rpm, the baseline curve has a difference of approximately 1 mm from the other two curves. Also, when reaching 900 rpm, there is a peak greater than 3 mm. Thereby, demonstrating the inability of this type of balance ring to compensate loads at high rotating basket spin velocities.

On the other hand, the curve BR1 represented by the dotted line has an arrangement of twelve forward blades alternated with twelve backward blades [12]. This arrangement lowers noticeably the vibration when compared to the baseline. The vibrations are of less amplitude (close to 1 mm), so an acceptable behavior is achieved between 600 and 850 rpm. This also appears in the curve of BR2, represented by the solid line, and corresponds to the preferred configuration of balance ring with twelve forward blades and twelve straight radial baffles [12].

Note that both designs, BR1 and BR2, account with 12 forward blades improving the balance ring performance in the transient-state, thus confirming the theory established in Chapter IX. Moreover, the design with backward blades (BR1), helps improving in a remarkable manner the steady state response, but its difference respect to

the design with 12 straight baffles (BR2) is minimal. BR2 renders overall lower vibrations as can be therefore regarded as a preferred choice. The blades interaction will need further theoretical model to explain this situation.

Figure 51 shows more vibration measurements for the left lateral side of the washing machine. For these measurements, the walking threshold is close to 1.4 mm of vibration peak to peak. As depicted on Fig. 51, the three curves baseline, BR1 and BR2 have a similar behavior from 0 to 550 rpm. Above this running speed, the baseline curve begins to be greater than the ones corresponding to BR1 and BR2, and increases all the way up to 800 rpm, reaching a magnitude greater than 3.5 mm close to 900 rpm, that is about 2 mm more than BR1 or BR2.

Also, an analysis of the aforementioned vibration graph, allows inferring that a conventional balance ring of straight radial blades is not suitable for high rpm, because as the rpm increased, their balancing ability is seriously degraded, which is not the case with the configurations BR1 and BR2 proposed herein. Again, BR2 evidences overall lower vibrations as can be therefore regarded as the choice of preference.

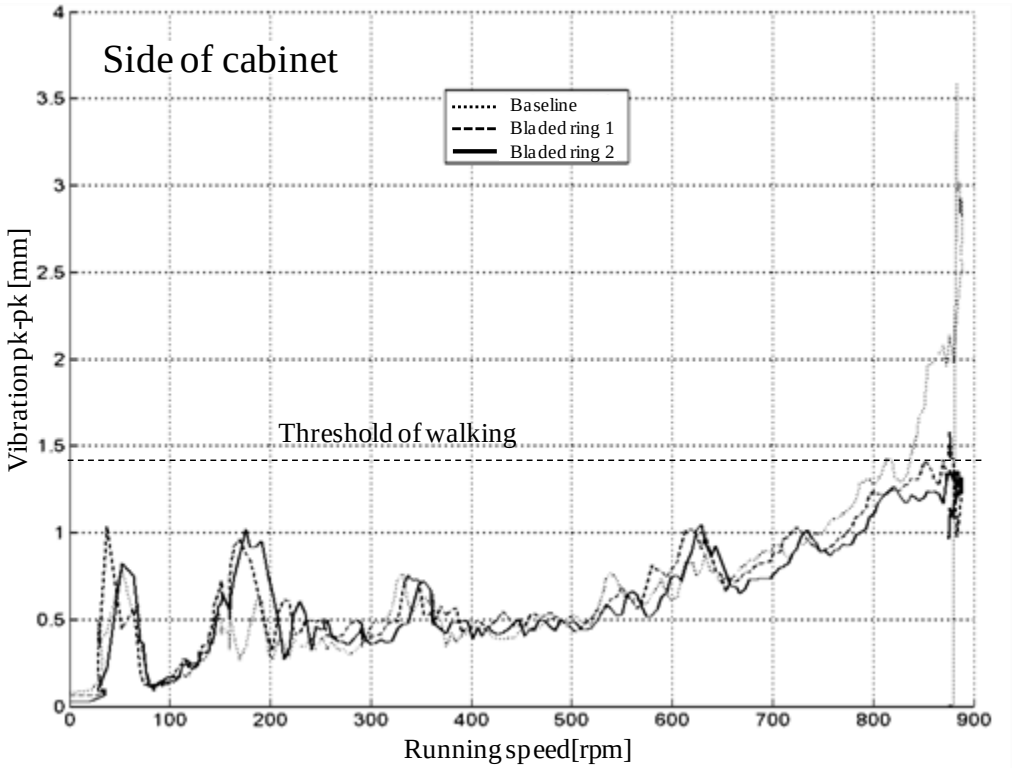

Figure 51. Measurement of vibration on the left side of the cabinet structure.

CHAPTER XI

TWO-PLANE HYBRID BALANCING SYSTEM

Proposal for the washing machine

As discussed in Chapter I, the self-balancing state-of-the-art technology in vertical-axis washing machines has evolved from employing a liquid balance ring situated on the lower part of the basket [2], to using the same device but on the to the top of the basket [5]. This solved space constraint for using larger baskets. Such baskets with larger volumetric capacity are nowadays profusely marketed and appreciated by users because more garments can be put into them. In this later arrangement, the liquid balancing force is exerted in a distant plane with regards to the unbalance force plane of action. As a consequence, this couple of forces induces alternating moments of importance for the dynamics of the system. Other self-balancing devices, like the ball-balance ring type have been suggested [28] to be employed on the top of the basket. A multiple autobalancing device combining together a liquid and a ball-balancing device has also been introduced [30] as an attempt to reduce vibrations and improve the system dynamics. Nonetheless, all these arrangements fail to cancel the dynamic moments simply because the garments unbalance force and the balancing force form the self-balancing device although canceling each other, are not coplanar, therefore a moment arises. This moment is of dynamic nature due the basket rotation. An efficient two-plane ball-balancing arrangement has been introduced in the market for front load washing machines [31]. This ingenious arrangement consists of identical ball-balancing devices

located at both ends of the rotating drum, thus self-adapting to cancel the garments unbalance force without generating a dynamic moment. Although, very attractive from the technology standpoint, this kind of balancing system is very expensive because the stainless steel balls are many times costlier than the water based brine solution employed in the liquid balancer counterpart. A cost-effective washing machine balancing arrangement should meet the following high-level specifications.

1. Require minimum space to accommodate in washing machines with large baskets.
2. Compensate effectively unbalance forces without generating dynamic moments.
3. Affordable production costs.

The proposal of an improved balancing arrangement is shown on Fig. 52, which has been filed as a patent application [43], and consists on

1. A textile vertical-axis washing machine having a rotating basket balanced in both its planes with a first liquid balance ring that crowns the basket, and a second ball-balance ring structured in the lower part of the basket.

2. The top balance ring being either of conventional straight baffle boards or of bladed (forward and backward) balance ring type as the one introduced in Chapter X.
3. The polypropylene basket bottom comprising; a) channel or track that is an integral part of the bottom of the basket, b) a viscous drag fluid lodged in the track, c) a plurality of steel balls situated in the channel or track, immersed in the viscous drag fluid, and d) a top cover that seals hermetically against the track, the top cover comprises at least one radial rib in order to provide structural strength to the bottom of the basket, in order to prevent the bottom of the basket from weakening due to the presence of the track or channel, see Fig. 53. The plastic top cover is to be welded by hot-plate, ultrasound or the like plastic welding technology. This cover accounts with a hole for dispatching lubricating oil inside the track, a plastic plug is to be spin welded to the top cover to close such hole.

This invention [43] introduces the use of a ball-balancing device to be integrally formed in the bottom of the rotating basket at low cost and minimum axial space requirements. Thus, it is less expensive than employing two ball-balancing devices [31], while it makes feasible employing baskets with larger volumetric capacity than the liquid balance ring counterpart [2].

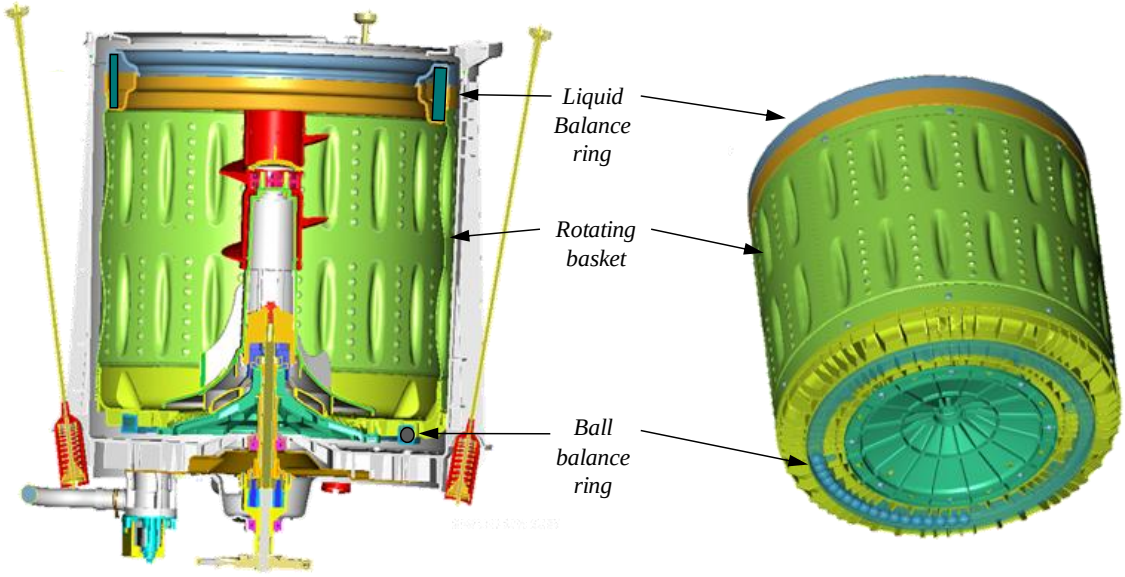

Figure 52. Two-plane balancing system; (a) cross-section, and (b) basket assembly (courtesy of *mabe S.A. de C.V.*).

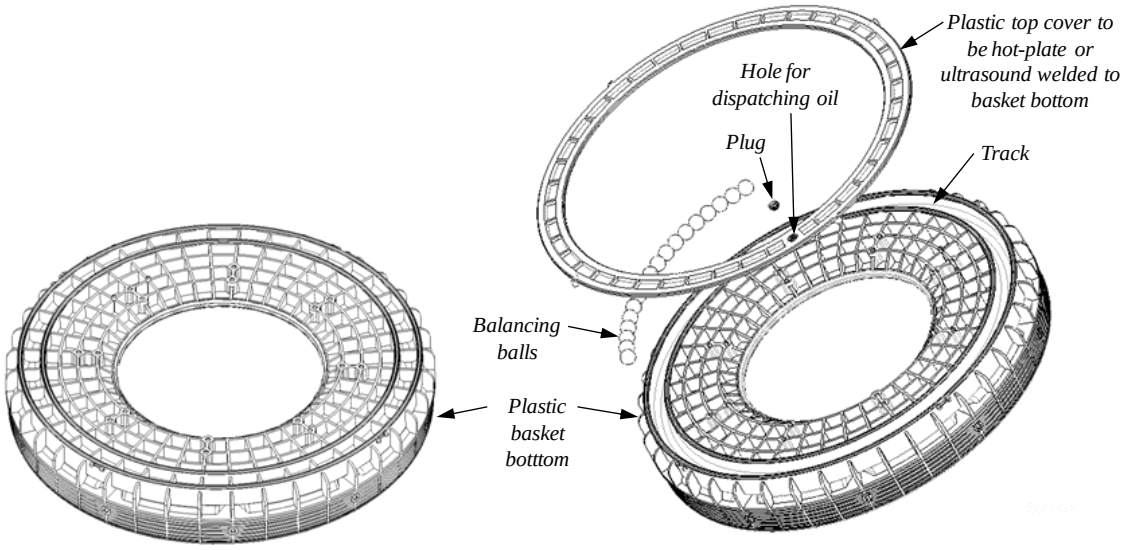

(a) (b)

Figure 53. Basket bottom; (a) conventional technology, and (b) basket bottom with integral ball-balancing device, (courtesy of *mabe S.A. de C.V.*).

Note that the steel balls run submerged in a fluid that has a specific viscosity; the specific function of the fluid is to lubricate and drag the balls to traverse the transient-state more smoothly, so that they do not slip within the track and reach the position contrary to the unbalanced load in a quicker manner. This also helps mitigating the noise generated by the balls rolling action and the collision among them.

The drag fluid to be introduced has a viscosity between 200 and 300 cSt at 40 °C, with a inflammability temperature higher than 300 °C. The acidity in the drag fluid should also be taken care of, namely, that the acidity could age or damage the steel balls, or it could ruin the manufacturing material of the basket bottom. Being that the plastic basket bottom containing the lubricating oil is submerged in water, and that the possibility of leaking and garments contamination exists, the oil should also meet the Restriction of Hazardous Substances (RoHS) [44] regulation and comply with the applicable environment legislation or standards of the specific country for the washing machine to be sold in.

Free-body diagram (static approach)

A hybrid two-plane balancing system was introduced in a washing machine [43]. The upper balancer being a conventional liquid balance ring placed on top of the rotating basket, whereas a balancer of the ball-type was fitted to the bottom of such basket. This configuration, as will be demonstrated, enables an effective reduction of moments and forces in the rotating system.

Although the system bounces vertically and also describes a planar motion, it is accurate enough to address only the governing planar motion, which is usually 3 to 5 and 6 to 8 times larger than the vertical one in the transient-state and steady-state, respectively. On the other hand, to further simplify the problem, given the rotor symmetry and the orbits of closely circular shape, it is valid enough to consider the system to be symmetric with no loss of accuracy.

A static approach was followed employing the fluid force Eq. (2), and using expressions to calculate the centrifugal force of the ball-balancing device. The radius of the center of gravity of a set of balls B located inside the track with mean radius r_t is given by Eq. (95)

$$r_{CG} = \left(-0.0025 \cdot B^2 - 0.0047 * B + 8.2392\right)\ 2.54/100 \tag{95}$$

The balancing force of the set B of balls is obtained from

$$F_b = m_B B\left(r_{CG} + z\right)\omega^2 \tag{96}$$

The unbalance force in turn is computed from

$$U = m_u\left(r_b + z\right)\omega^2 \tag{97}$$

Where m_B, m_u, are the set of balls and unbalance mass, respectively. On the other hand, z is the basket excursion or mean orbit radius, and r_b is the basket diameter. Figure 54 shows a free body diagram of the washing machine.

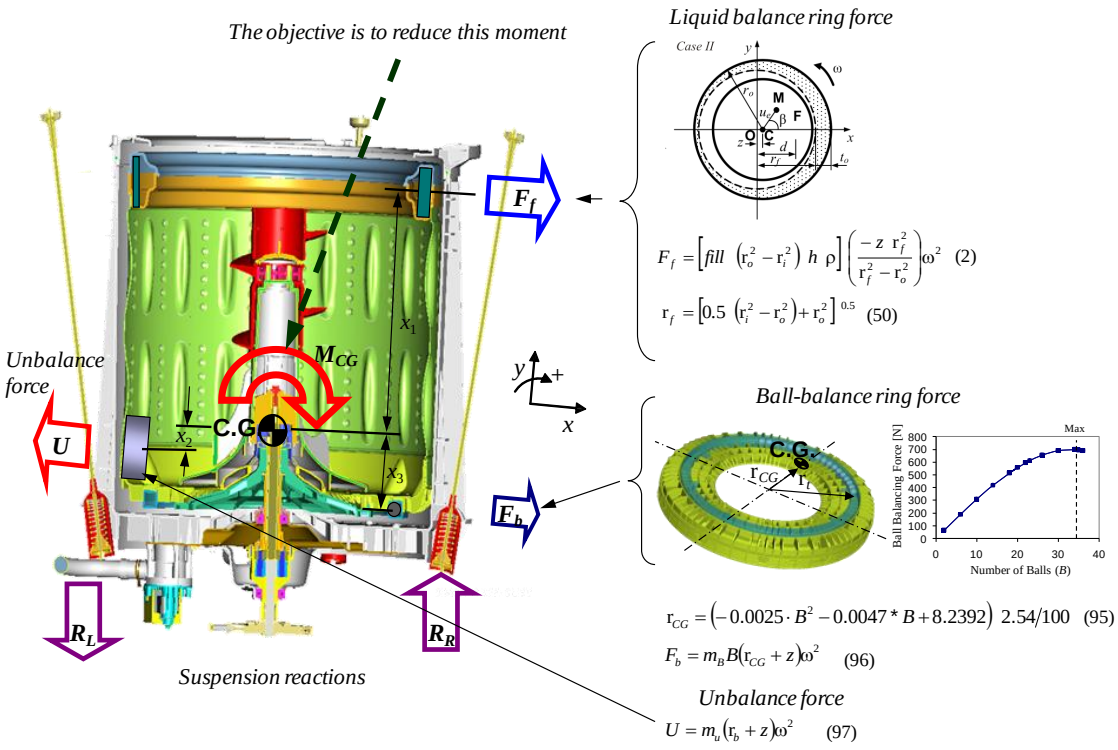

Figure 54. Free body diagram of a washing machine with a two-plane balancing system (courtesy of *mabe S.A. de C.V.*).

Both balance rings work together, that is the unbalance force U caused by the unbalance mass m_B acting at a distance x_2 from the center of gravity **C.G.**, provokes a moment M_{CG}, this moment is increased by the product of the fluid force F_f times the distance x_1, which also causes a moment around the center of gravity **C.G.** in the same direction (clockwise) as shown on Fig. 54. However, the lower ball-balance ring also

imposes a resulting force F_B acting at a distance x_3, which also induces a moment around the center of gravity **C.G.** with negative sign, i.e. counterclockwise. Thereby, the ball balancing induced moment counteracts the unbalance moment and the moment due the liquid force. In an ideal situation, the addition of moments around the center of gravity **C.G.** are zero, herewith Eq. (98) provides the equation of moments that is obtained around the **C.G.**

$$M_{CG} = F_f \times x_1 + m_u \times x_2 - F_b \times x_3 \tag{98}$$

and

$$F_{net} = F_f + F_b - U \tag{99}$$

Where F_{net} is the total force resulting in the rotating basket.

Note that without the lower ball-balance ring, the resulting moment would always be positive, causing a conical vibration mode, therefore the lower ball balance ring reduces the magnitude of the resulting moment. Consequently, the forces transmitted to the shaft, bearings, tub and suspension should also all be reduced.

Analysis for optimum amount of balls

The optimum amount of balls to use within the balancer is analyzed in this section. Figure 55 illustrates the forces acting on the system at the ball-balancer plane. In building this graph, the following values have been used; x_1 = 0.258 m, x_2 = 0.108 m, x_3 = 0.248 m, F_f is computed from Eq. (2) as 606 N, and finally the unbalance force U is provided in Fig. 29 and amounts to 1381 N for m_u = 1 kg.

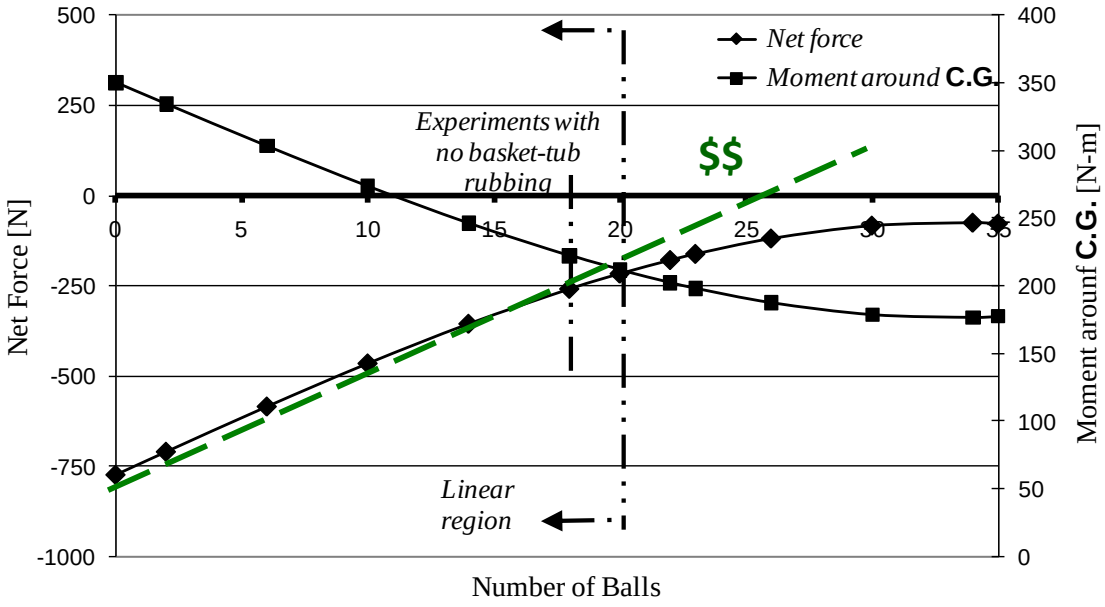

Figure 55. Net Force and Moment around **C.G.** for different amount of balls.

It can be appreciated that as the number of balls increases, the associated centrifugal balancing force augments. The maximum amount of balls that can be accommodated in the balancer track is such that half of its circumference is filled and is equal to 34. However, as shown schematically on Fig. 56, as half of the track saturates,

those balls close to the vertical axis have a strong vertical force component, which does not help balancing. On the contrary, the horizontal force component exerted by those balls close to the vertical, do help achieving balancing but is of very low magnitude. Therefore, it is expected that there should be an optimum amount of balls from a cost-effective standpoint to maximize the benefit in performance. Furthermore, it is known that for a pin-joint, the equivalent loaded area under normal stress is one projected pin diameter over the plate circumference times the thickness of the plate. Then, establishing an analogy with such pin-joint, see Figure 57, the amount of balls (B_{perf}), actually performing an effective balancing force on the system, can be approximated as those filling one projected diameter over the mean circumference of the track as provided by Eq. (100)

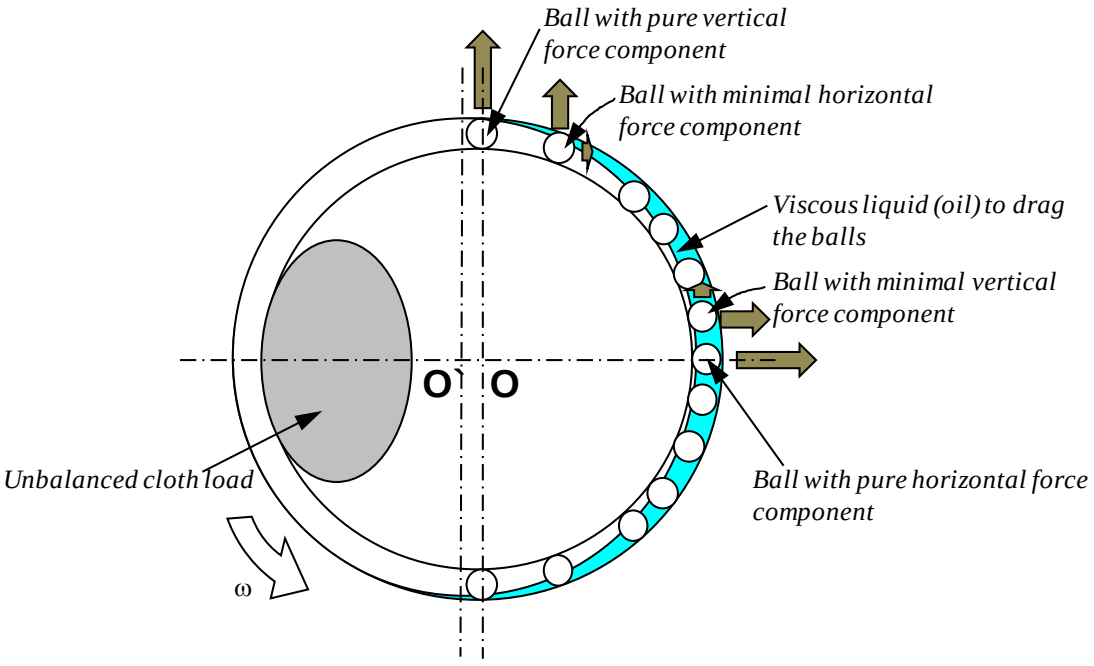

Figure 56. Ball force components.

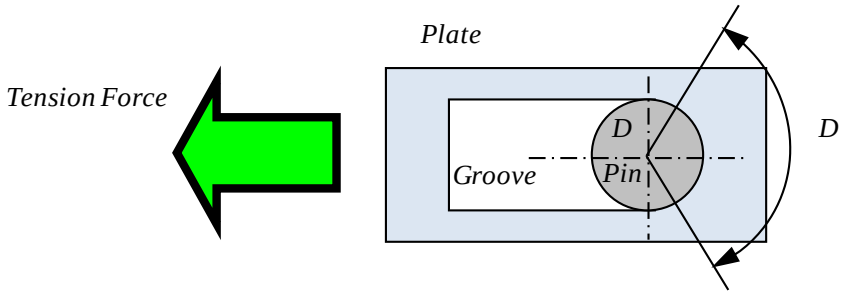

Figure 57. Analogy with a pin-joint.

$$B_{perf} = \frac{2 \times r_t}{\phi_b} = \frac{2 \times 0.219\ \text{m}}{0.019\ \text{m}} = 23.05 \approx 23 \tag{100}$$

Other considerations about the number of balls follow:

- Amount of balls to fill half circumference ($B_{full\ half}$) = $\pi \times r_t / \phi_b$ = 34
- Effective amount of balls (B_{perf}) = 23, from Eq. (100)
- Amount of balls for optimum benefit vs cost ($B_{cost\text{-}effective}$) = 20 (linear zone on Fig. 55)
- Amount of balls available for testing (B_{tested}) = 18

Tests were performed with 18 balls due to availability for building a prototype. However, the best possible choice seems to be 20 since beyond that number, the obtained benefit in reducing the net forces and dynamic moment is less worth the cost.

Experimental set up

A basket accounting with a conventional liquid balance ring on its upper part was modified to include a lower balance ring of the ball type. Figure 58 shows a bottom view of such basket.

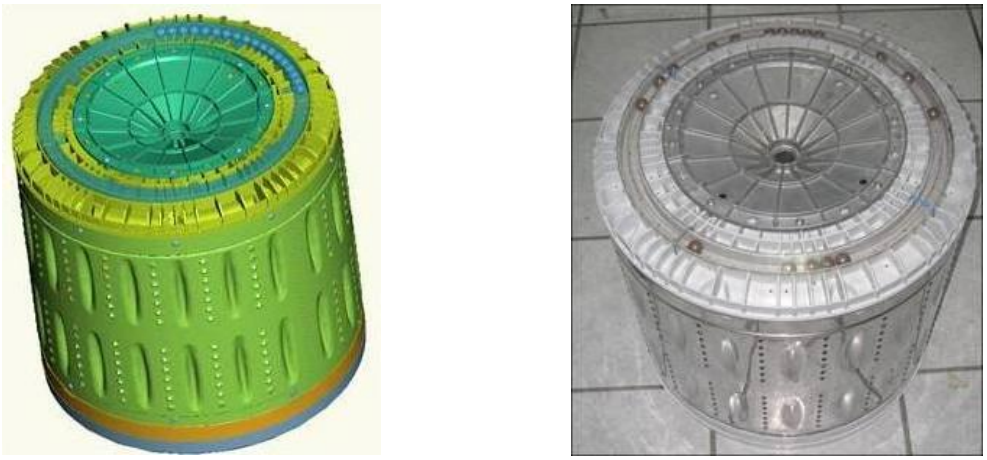

(a) (b)

Figure 58. Bottom view of basket; (a) Pro-E model, and (b) Prototype (courtesy of *mabe S.A. de C.V.*).

The characteristics of the prototype are listed following

- Ball weight = 30 grs.
- Amount of balls = 18
- Total balls weigth = 0.540 kg
- Ball diameter = 19.05 mm (3/4”)
- Mean track diameter = 0.219 m
- Cavity cross-section dimensions = 20.3 mm x 20.3 mm

The washing unit is mounted on a rigid frame for performing the vibration experiments. The orthogonal components of the vibration were measured at the balance ring and tub with Banner LG® series laser short-range precision displacement transducers with a resolution of 10 μm. The laser transducers were supported by a versatile Nylamid rack designed to surround the rigid frame. Although the rack has the ability of accommodating laser transducers at two different planes, displacement measurements were only performed on the top plane. The position of the transducers with respect to the washing unit is shown in Figure 59. The transducers were installed 0.1 m away from the target surface.

A NI PXI 4472 DAQ system used to collect data during the experiments. The signals provided by the laser transducers placed at orthogonal directions were coupled to observe the general patterns of the orbit described by the rotating basket whirling motion. The system was operated at a speed of 670 rpm by a variable frequency motor that could drive the rotor at any given acceleration rate or maintain any steady rotational speed up to 1000 rpm. General purpose Visay® strain gage rosettes in rectangular array were attached to the metallic support of the drive system to measure experimental stresses. The grid resistance of the strain gages is 120±0.2% Ohms. Pepperl & Fuchs ultrasound UC300-F43-2KIR2-V17 with a resolution of 0.2E–03 m were employed for displacement measurement. Force transducers HBM VDI/VDE with integrated lateral force compensation and with a resolution of 0.2 N were used to measure transmitted force to cabinet.

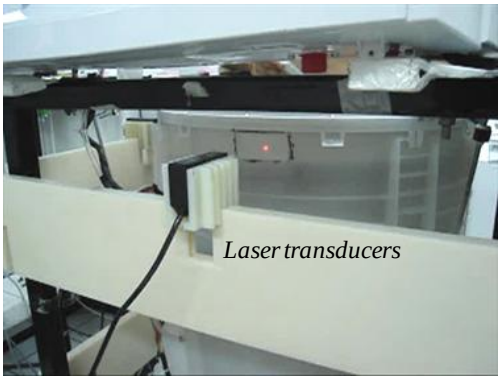

(a)

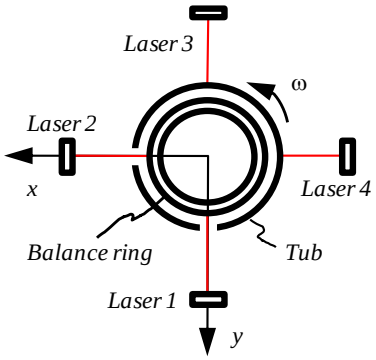

(b)

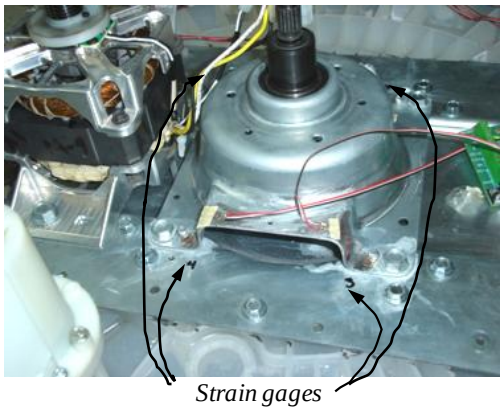

(c)

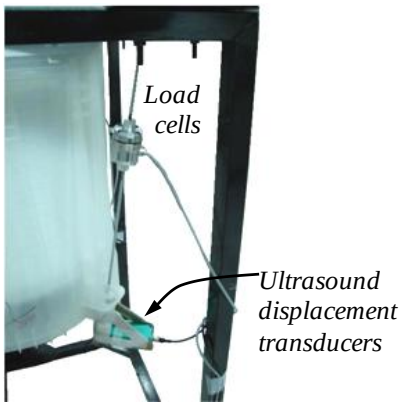

(d)

Figure 59. Experimental array; (a) Laser transducer through window on tub, (b) Laser transducer arrangement, (c) strain gages location on drive system, and (d) load cells and ultrasound transducers on suspension.

Experimental results

Experiments were made to validate the theory and verify the effectiveness of the hybrid two-plane balancing system as shown on Figure 60. The tub and basket orbits were built by coupling the orthogonal displacement signals of the laser transducers as

shown in Fig. 59(b). Before turning on the machine in spin mode, the unbalance location was aligned with the *x*-ayis at 0 deg. A reflecting aluminum foil was attached to the balance ring also aligned with the unbalance load. A photocell supported by a microphone extensible arm was pointing downwards at 0 deg, this instrument provided a one-per-revolution reading that allowed signals correct superposition to build the orbits. Figure 60(a) shows the initial point, at rest, of the tub, basket, and their relative motion (RM). As the rotating motion begins, and the basket completes a quarter of revolution, i.e. de unbalance moves 90 deg around, the tub and basket describe a partial orbit trace, see Fig. 60(b). Later, once a full basket revolution is completed, the tub and basket describe a full orbit as depicted on Fig. 60(c). The orbits provide useful information in the analysis of the system dynamics as will be discussed next.

An important parameter will be introduced for the analysis, namely; the mean orbit eccentricity. This parameter refers to the maximum radius minus the minimum radius of an orbit. In other words, the orbit eccentricity is a parameter that tells how elliptic or circular an orbit is. The larger this value, the more elliptic the orbit is, whereas an eccentricity of cero corresponds to a circular orbit. A similar rationale was applied for the transmitted force to cabinet and for the stresses on the drive system. The force eccentricity means how large is the difference in the transmitted force by the four suspension assemblies connected to the cabinet. Similarly, the stress eccentricity relates to the difference in the stresses measured by the four strain gage rosettes.

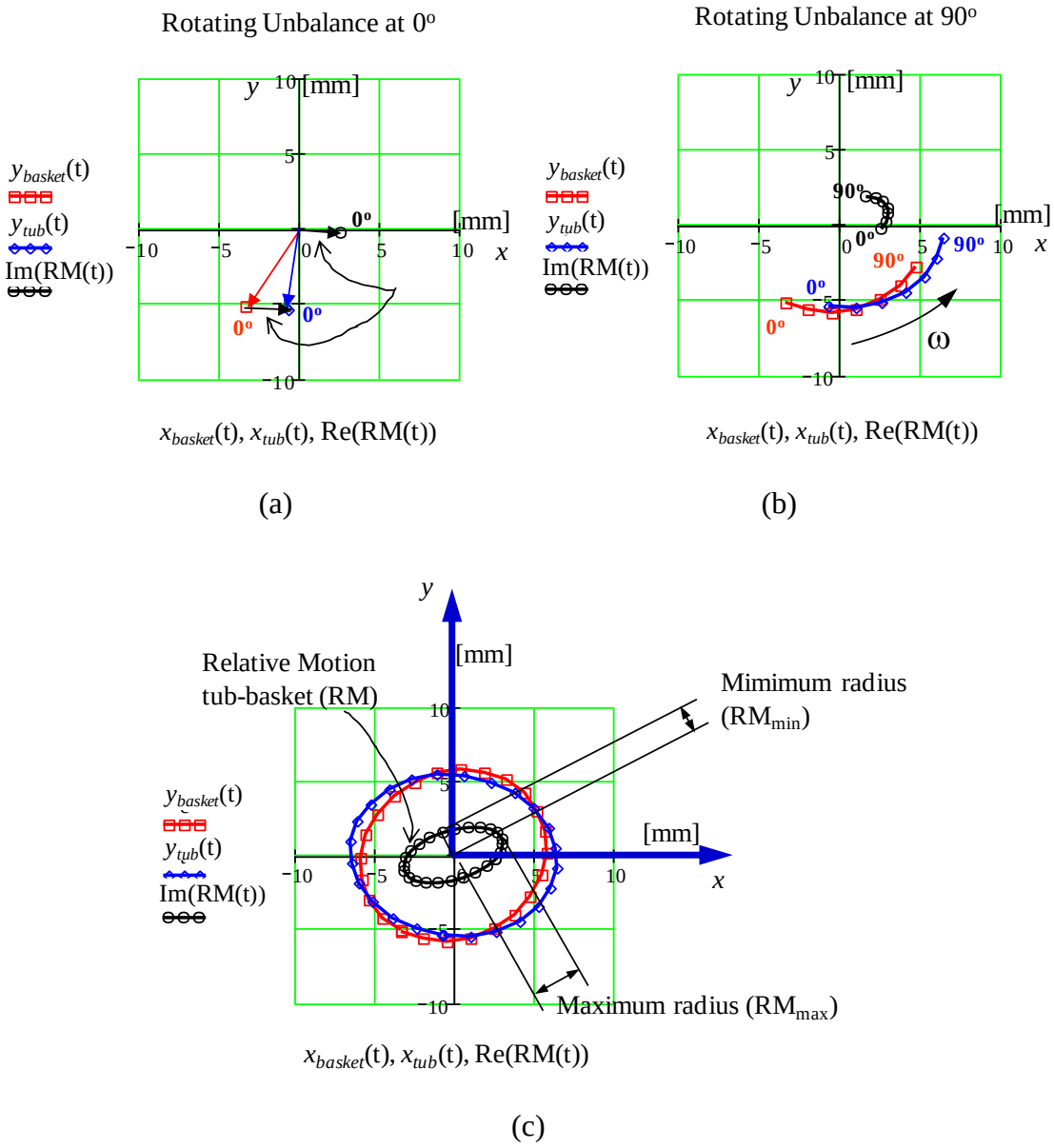

Figure 60. Orbit construction from orthogonal laser displacement transducers; (a) initial position, at rest, with unbalance at 0 deg, (b) partial orbit trace with unbalance at 90 deg, and (c) full orbit trace with unbalance again at 0 deg.

On the other hand, the relative motion (RM) between tub and basket was computed from the difference in the point-to-point *x* and *y* displacements as given by Eq. (101).

$$\mathrm{RM}(\mathrm{t}) = \left[x_{tube}(\mathrm{t}) + jy_{tube}(\mathrm{t})\right] - \left[x_{basket}(\mathrm{t}) + jy_{basket}(\mathrm{t})\right] \tag{101}$$

The instantaneous relative motion radius at the time t_i is defined by Eq. (102)

$$\mathrm{RM}(\mathrm{t})_i = \left[\mathrm{Re}\left(\mathrm{RM}(\mathrm{t}_i)\right)^2 + \mathrm{Im}\left[\mathrm{RM}(\mathrm{t}_i)\right]^2\right]^{0.5} \tag{102}$$

An important parameter is the difference between the maximum relative motion (RM_{max}) and minimum value of relative motion (RM_{min}). Lets define this parameter as the relative motion eccentricity (RM_{ecc}) given by Eq. (103). If RM_{ecc} tends to zero, then the tub-basket gap tends to be more homogeneous. In contrast, the largest the difference between RM_{max} and RM_{min}, the more uneven the gap between the tub and basket becomes and the likelihood of rubbing increases.

$$\mathrm{RM}_{ecc} = \mathrm{RM}_{max} - \mathrm{RM}_{min} \tag{103}$$

Finally, the tension (P) and compression (Q) stresses were computed according to Eq. (104) and Eq. (105), respectively. Their eccentricities were also studied and displayed on Fig. 61(d).

$$P = \frac{\sigma_1 + \sigma_3}{2} \tag{104}$$

$$Q = \frac{\sigma_1 - \sigma_3}{2} \tag{105}$$

Figure 61 depicts all these parameters for analysis as measured on a 15 kg model washer. This model was introduced as a derivative of the 14 kg washer shown on Fig. 54. The rotating basket height had to be increased by about 0.0254 m (1 in) to accommodate the increased load. This increased height as small as it seems, caused tub-basket rubbing in the early reliability tests. In the graphs, the term 15 kg modified, corresponds to the new washing machine with the following modifications; a) longer screws attaching the basket to its hub, and b) increased area of radial contact between the hub and the shaft, both as fixes to avoid rubbing. The 15 kg TPBS stands for the 15 kg derivative model accounting with a two-plane balancing system. Five replicates were obtained for each case of interest, the maximum and minimum values found are indicated by the intervals of each case, namely; 14 kg included as benchmark case, 15 kg as the baseline case, 15 kg modified with the conventional fixes case, and 15 kg TPBS as the new technology case [43].

The two-place balancing system (15 kg TPBS case) enables a basket orbit eccentricity reduction of 31% when compared to the 15 kg baseline case, indicating that the tub-basket gap is distributed more homogeneously around the circumference of the

bodies. The mean basket orbit radius seems to increase for the 15 kg TPBS case, for both, the tub and the basket. However, this is not necessarily disadvantageous as the tub orbit becomes more circular than the 15 kg baseline case, and more importantly of more circular relative motion (RM) than the 15 kg baseline case as depicted on Fig. 62.

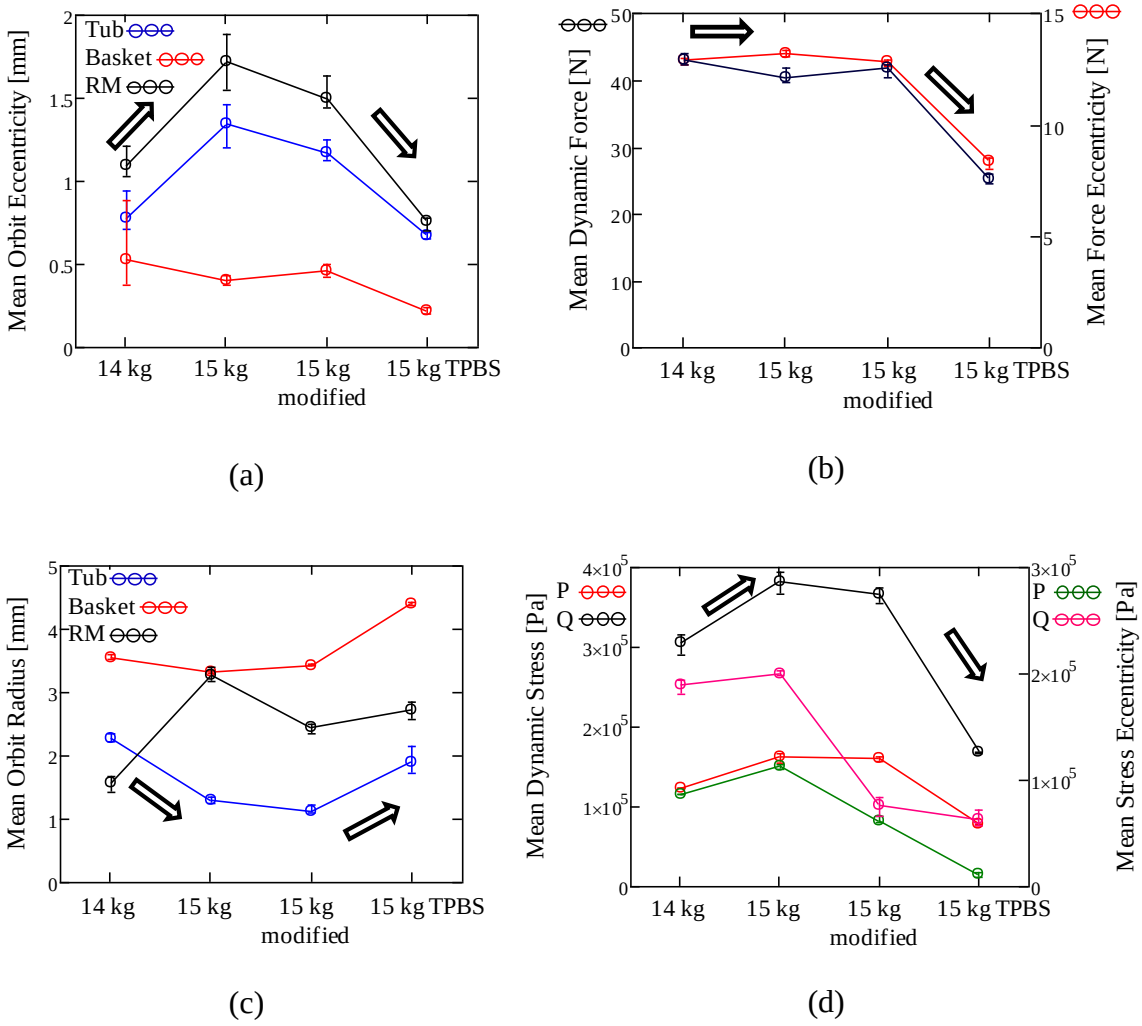

Figure 61. Experimental results with a two-plane balancing system; (a) mean orbit eccentricity, (b) mean dynamic force and eccentricity, (c) mean orbit radius, and (d) mean dynamic stress and eccentricity.

Coming back to Fig. 61, when comparing the 15 kg TPBS case against the 15 kg baseline case, the force transmitted to the four suspension assemblies is more homogeneous by 42% with the two-plane balancing system. On the other hand, the evenness of P-Q stresses sustained by the transmission support improves by 87% and 67%, respectively.

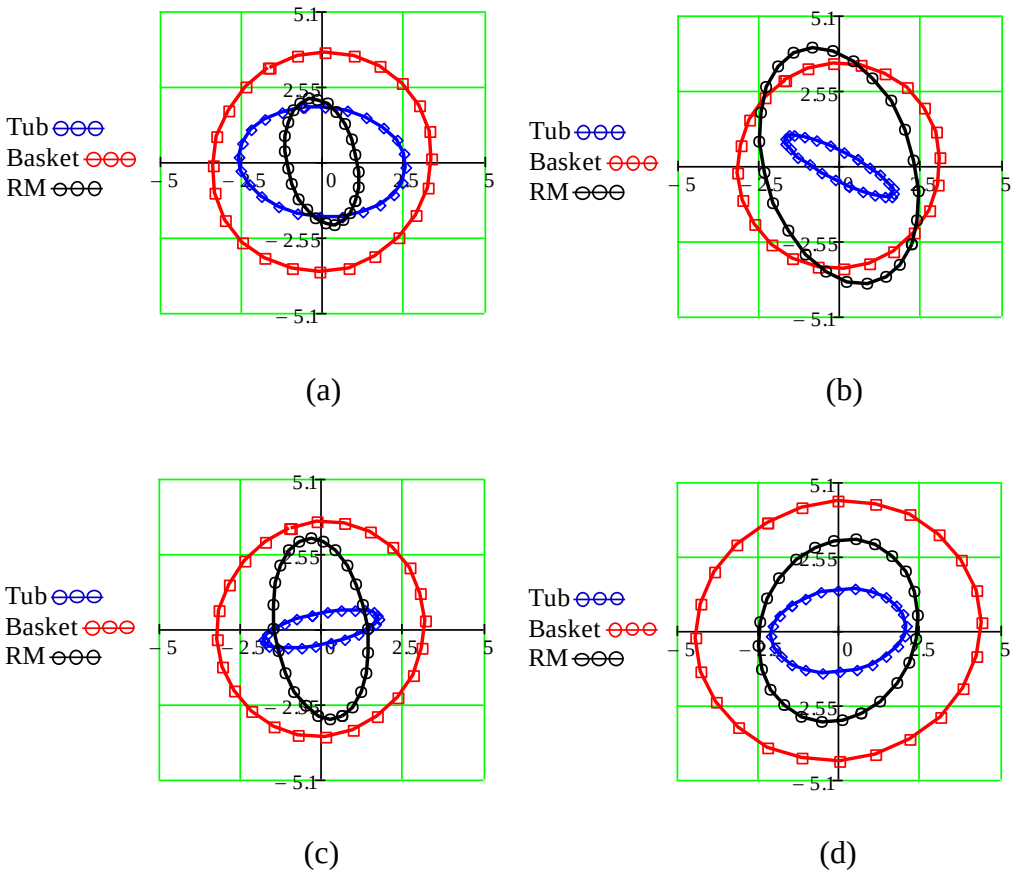

Figure 62. Orbits for; (a) 14 kg benchmark case, (b) 15 kg baseline, (c) 15 kg modified with conventional fixes, and (d) 15 kg TPBS.

Figure 62 shows the tub, basket, and relative motion orbits for the different cases studied. Note that although the tub and basket are of larger size for the 15 kg TPBS than the 15 kg baseline case, the forces transmitted to cabined as well as the stresses on the drive system supports are of much less magnitude for the 15 kg TPBS than the 15 kg baseline case. This is precisely due to the larger excursions described by the washing unit. That is, since the suspended bodies execute larger orbits, more kinetic energy is required to maintain this motion, hence less energy is transmitted from the rotating basket, to the supports, tub, suspension and cabinet structure. It sometimes is convenient to split the total kinetic energy of a body into the sum of the body's center-of-mass translational kinetic energy and the energy of rotation around the center of mass (rotational energy) as stated in Eq. (106)

$$E_k = E_{translational} + E_{rotational} \tag{106}$$

Where

E_k is the total kinetic energy

$E_{translational}$ is the translational kinetic energy

$E_{rotational}$ is the rotational or angular kinetic energy in the fixed frame

Thus, the basket possesses kinetic energy due to its rotation and translation. However, the kinetic energy of the tub is due only to its translational motion because it

does not rotate. The rotational energy (E_r) around the basket axis of rotation, depends on the moment of inertia of the basket and its angular velocity as shown on Eq. (107)

$$E_{rotational} = \frac{1}{2} I_b \omega^2 \tag{107}$$

Where

ω is the angular speed, and

I_b is the basket moment of inertia around the axis of rotation.

On the other hand, the system translational kinetic energy is provided by Eq. (108).

$$E_{translational} = \frac{1}{2} m_t v_t^{\,2} + \frac{1}{2} m_b v_b^{\,2} \tag{108}$$

Where

v_t is the tangential speed of the tub

v_b is the tangential speed of the basket

m_t is the tube mass, and

m_b is the basket mass

As the excursion of the tub and basket augments, the tangential velocity of both bodies increases as well. Therefore, according to Eq. (108), the required translational kinetic energy to execute such larger excursions increases. This makes the damping mechanisms available in the system to work better, such like the suspension dashpot assemblies supporting the tub, and the suspension knuckle joints resting on the cabinet structure. In this way, less forces and stresses are imposed to the mechanical components and a better performance is achieved.

Note that the average basket mean orbit radius for the 15 kg TPBS case is 4.4 mm, whereas the basket mean orbit radius for the 14 kg benchmark case is 3.6 mm, the ratio of one to another is 1.22. That is, the 15 kg TPBS orbit is 22% larger than the 14 kg benchmark case. However, the average tub mean radius for the 15 kg TPBS and 14 kg benchmark cases are 1.9 mm, and 2.28, respectively. The later indicates that the tub orbit in the 15 kg TPBS case is 17% smaller than the 14 kg benchmark case. Hence, the risk of collision between tub and the cabinet structure reduces. In other words, a washing machine accounting with a two-plane balancing system can tolerate larger unbalances without experiencing striking of the wash unit against the cabinet.

Correlation

The classic formula for determining the alternating bending stress in a beam under simple bending is given by Eq.(109)

$$\sigma_a = \frac{Mc}{\mathrm{I}} \tag{109}$$

Where

σ_a is the bending stress

M is the dynamic moment about the neutral axis

c is the distance from the extreme fiber to the neutral axis

I is the second moment of area about the neutral axis

From Eq. (109) it can be easily deduced that since c and I are constants, the alternating stress is directly proportional to the dynamic moment M. Therefore, the theoretical reduction of M_{CG} when using a two-plane balancing system, will be compared to the measured tension (P) and compression (Q) stresses in the support systems, which are also a lineal effect of the actual dynamic moment present in the system. Confrontation of theoretical predictions and experiments is presented in Table 7. A good correlation between the static approach and the measurements is evident.

Table 7. Theoretical alternating stress vs measured P-Q stresses.

Theoretical Stress	**Estimated reduction [%]**	**Experimental Stress**	**Measured reduction [%]**
σ_a	37	P	34
		Q	45
Dimensionless		Average	39.5

CHAPTER XII

CONCLUSIONS

Concluding remarks

The lack of baffles renders uneven distribution of the fluid inside the cavity with strong unstable behavior. On the contrary, the addition of eight baffles helps develop a synchronous fluid tangential velocity with rotor running speed. A number of eight baffles excite the fluid fourth circumferential mode of vibration and the eighth axial mode of vibration. The fluid is found to develop a backward inertia wave relative to the rigid body motion. The effective mass traveling backwards amounts to 0.33 of fluid total mass. This backward wave acts as a damping force 90^o phase lagged with respect to rotor motion, thereby causing the phase angle between the unbalance and the fluid center of mass location to change from 180 to 150^o.

Built-up rotors are prone to instability due to internal damping. The assembly interface causes internal friction to arise. Some turbomachines account with shrink-fit aluminum wheels that may be potential sources of instability. In many other cases separating steel wheels and sleeves in between stages also interference fitted can add internal rotor damping. This research presents for the first time the stabilizing capabilities of the LeBlanc balancer. Hollow rotors with fluid trapped inside, suspension segregation centrifuges, liquid-cooled gas turbines, spin-stabilized satellites, spinning rockets containing liquid fuel, home appliances such as washer machines, liquid-filled

flywheel apparatus for motorcycles, automobiles, trailers and heavy vehicles tires self-balancing are just few examples of machines for which this kind of balancer is applicable not only to balance the rotating system but also to achieve much higher stable rotational speeds.

Several solutions to the unbalance problem in washing machines have been developed, the previous art shows the use of balance rings, which are hollow rings placed on the top part of the washing basket. This ring partly acts as a counterweight to the load of clothes because inside the ring, there is either some type of liquid or solid balls that adopt an antagonist position to the centrifugal forces created by the position adopted by the objects to wash, thus balancing the rotating basket. Nonetheless, the alternative of designing curved baffles like blades has never been explored before until now. This research work introduces for the first time a balance ring with curved (forward and backward) blades that remarkably enhance the unbalance transient and steady-state response of the washing machine, having a cabinet vibration reduction up to 2 times less, by improving the fluid-solid interaction.

Among the objects of the first invention are to produce a bladed balance ring that does not employ an expensive fluid, it is easy to manufacture, reduces the vibration generated during the transient-state, operates at high velocities, and that can be adapted to different types of washing baskets of vertical-axis washing machines in a preferred choice, but without excluding horizontal-axis washer appliances.

A second invention consists on ball-balance ring is structurally formed at the lower part of the basket or bottom of basket in order to balance the lower plane of the rotary basket along with a liquid balance ring placed at the upper part of the basket to conform a two-plane balancing system.

This two-place balancing system enables a basket orbit eccentricity reduction of 31%, indicating that the tub-basket gap is distributed more homogeneously around the circumference of the bodies reducing the likelihood of rubbing between the bodies. The mean basket orbit radius seems to increase, particularly for the tub. However, this is not necessarily disadvantageous as the orbits are more circular and actually of smaller size than the baseline ones of elliptical shape. On the other hand,, the force transmitted to the four suspension assemblies is more homogeneous by 42%. On the other hand, the evenness of P-Q stresses sustained by the transmission support improves by 87% and 67%, respectively.

Finally, the tub orbit in a washing machine accounting with a two-plane balancing reduces by 17% when compared to the benchmark case. Hence, the risk of collision between tub and the cabinet structure reduces. In other words, a washing machine accounting with a two-plane balancing system can tolerate larger unbalances without experiencing striking of the wash unit against the cabinet.

Products and contributions of this research

The published results of this research are available in the archival literature as follows:

Journal papers

[1] **Urbiola-Soto**, L., and Lopez-Parra, M., 2011, "Dynamic Performance Of The LeBlanc Balancer For Automatic Washing Machines," *ASME Journal of Vibration and Acoustics,* **133-4** (2011).

Chapter VI is mainly written from this paper, its contributions may be summarized as follows:

- Dynamic 4-dof model aimed as a design tool to predict the unbalance response across a frequency range.
- Employ the above model to understand the liquid fill ratio in the ring cavity to reduce unbalance response (0.5) and to minimize transmitted force (0.8).

[2] **Urbiola-Soto**, L., and Lopez-Parra, M., 2011, "Liquid Self-Balancing Device Effects on Flexible Rotor Stability," *Submitted to Journal of Shock and Vibration,* review completed, recommended for publication with corrections.

Chapters IV, VII, and VIII contain portions of this publication aimed to:

- Develop the theory to explain the hollow-rotor stability improvement when trapped fluids interact with baffle boards, and provide examples for turbomachiney potential applications.

Conference peer-reviewed papers

[3] **Urbiola-Soto**, L., and Lopez-Parra, M., 2011, "Stability of Flexible Rotors with a LeBlanc Balancer," ASME paper GT2011-46848, *Proceedings of AME Turbo Expo 2011,* Vancouver, Canada, June 6-10.

Chapters VII and VIII have been prepared in accordance with this paper with the following contributions:

- Rotordynamics model to explain how a liquid balance ring contributes to raise the threshold speed of instability for aerodynamic cross-coupling and rotor internal friction damping.

[4] **Urbiola-Soto, L.**, Lopez-Parra, M., 2010, "Experimental and Analytical Investigation on a Liquid Balance Ring for Automatic Washing Machines", *Proceedings of the ASME 2010 10th Biennial Conference on Engineering Systems Design and Analysis (ESDA 2010),* Istanbul, Turkey, July 12-14.

Chapters II, IV, and V have been partially written from this research intended to:

- Experimental investigation to evidence the fluid backwards traveling wave existing in a liquid balance ring.
- Explain the effects of the backwards traveling wave on the unbalance response phase lag.
- Model such phase lag effect as a "fluid damping mass" for predicting the unbalance response.
- Identify the effects of the baffle boards in raising the fluid modes of vibration.

Patents

[5] **Urbiola, L.** et. al., 2009, "Hydrodynamic Balance Ring for Centrifugal Rotation Machines," Canadian Intellectual Property Office CA 2646745, Jun 19, also 2009, US Patent and Trademark Office Application 2009/0158783 A1, June 25. http://ip.com/patapp/US20090158783

Chapters IX and X have been partially written from this patent, which contributes to extend the sate-of-the-art by:

- Modeling the fluid particle differential equation of motion.
- Claiming a high-performance bladed geometry for the baffle boards of a liquid balance ring.

[6] **Urbiola, L.** et. al., 2010, "Balance Ring System on Two Planes for a Spin Rotary Machine," Canadian Intellectual Property Office CA 2693639, Aug. 27, also 2011, US Patent and Trademark Office Application 2011/0048081 A1, March 3. http://ip.com/patapp/US20110048081

Chapter XI is extracted from this patent, which contributes to extend the sate-of-the-art by:

- Introducing a hybrid two-plane balancing system comprised by a liquid and a ball balance ring.
- Claiming a feasible design that is manufacturable by conventional means and at low cost.

Recommendations for future research

Although the liquid balancing devices are over a century old, while the dynamics of rotating fluids first studies date back half a century ago, there is still a hole in the knowledge on the dynamics of rotating cylinders partially filled with liquid and incorporating radial baffles. Nonetheless, these devices are widely used by home appliance manufacturers since the 40's. In the author's opinion, the underlying reasons for this lack of knowledge are as follows; the high sense of competitiveness among appliance manufactures, which hold a restrictive policy for the publication of the available technology for designing this type of component, the absence of attention from academics and researchers, and plainly because there is not much developed insight into this kind of device yet. Therefore, in answering existing questions, all research endeavors in this subject naturally open new ones, among the topics to further in knowledge are:

- A relationship between the number and shape of blades and the amount of damping added by the backward traveling wave. That would require to update the "fluid damping mass" equation provided by Eq. (5). Some work has been advanced already at mabe, however given that this is sensitive information for the company, it will not be disclosed in this dissertation.

- A model that could explain the technical compromise between the liquid balance ring capability and its stability characteristics reported in this research.

- A fluid dynamics model that could explain the interactions of forward and backward blades.

- To advance a dynamic model that considers the balance ring axial motion of the fluid, such that a 3D blade geometry could be studied and developed.

- To develop new means to improve the fluid-solid interaction in the transient-state such like anti-sloshing barriers or middle axial plates accounting passages for controlling the axial fluid waves.

- A dynamic model coupling the top liquid balance ring along with the bottom ball-balance ring for; a) the conventional LeBlanc balancer, and b) the bladed balance ring introduced in this dissertation.

REFERENCES

[1] LeBlanc, M., 1914, “Automatic Balancer for Rotating Bodies,” US Patent 1,159,052.

[2] Dyer, J., 1945,“Domestic Appliance,” US Patent 2,375,635.

[3] De Remer, J. G., 1950,“Blancing of Rotatable Bodies,” US Patent 2,525,781.

[4] Van Kirk, J. y Burmeister, L., "An automatic balancer design for a vertical-axis clothes washing machine," ASME Paper No. 76-DE-24, 1976.

[5] Hayashi, G., Yamamoto, K., Yamamoto, Y., 1977, “Balancing Ring of Centrifugal Extractor ,” US Patent 4,044,626.

[6] Conrad, D.C., 1994, “On The Fundamentals of Automatic Washing Machine Design Based Upon Dynamic Constraints”, Ph.D. Thesis, Purdue University.

[7] Hoon, H. S., Young. L. J., Suzuki, S., and Gu, H. W., 2001, “A Study on the Dynamic Behaviour of an Automatic Washing Machine”, *Korea ADAMS User Conference*, **11 (8-9)**, 1-6.

[8] Morio, M., and Yutaka, N., 2002, “Washing Machine Dehydration Dynamics Analysis,” *Nihon Kikai Gakkai Nenji Taikai Koen Ronbunshu*, **5**, 209-216.

[9] Bae, S. Lee, J. M., Kang, J. S. and Yun, J.R., 2002, “Dynamic Analysis of an Automatic Washing Machine with a Hydraulic Balancer,” *Journal of Sound and Vibration*, **257**, 3-18.

[10] Urbiola, L., 2005, “Cálculo de los Efectos Inerciales (Radiales y Tangenciales) del Fluido del Aro de Balance,” Internal Research Report, mabe TyP.

[11] Jung. C.-H., Kim, C.-S., and Choi, Y.-H., 2008, "A Dynamic Model and Numerical Study on The Liquid Balancer Used in an Automatic Washing Machine," *Journal of Mechanical Science and Technology*, **22**, 1843-1852.

[12] Urbiola, L., et. al., 2009, "Hydrodynamic Balance Ring for Centrifugal Rotation Machines," US Patent and Trademark Office Application 20090158783 A1.

[13] Newkirk, B. L., 1924, "Shaft Whipping," General Electric Review, **27(3)**, 169-178.

[14] Kimball, A. L. Jr., 1924, "Internal Friction Theory of Shaft Whirling," General Electric Review, **27(4)**, 244-251.

[15] Gunter, E. J., 1966, "Dynamic Stability of Rotor-Bearing Systems," NASA Technical Report, SP-113.

[16] Black, H.F., 1976, "The Stabilizing Capacity of Bearings for Flexible Rotors with Hysteresis," *ASME Journal of Engineering for Industry*, **2**, 87-91.

[17] Lund, J. W., 1986, "Destabilization of Rotors from Friction in Internal Joints with Micro-slip," International Conference in Rotordynamics, JSME, 487-491.

[18] Srinivasan, A., 2003, "The Influence of Internal Friction on Rotordynamic Instability," M.S. Thesis, Texas A&M University, May.

[19] Kollmann, F. G., 1962, "Experimentelle und Theoretische Untersuchungen Uber die Kritischen Drehzahlen Flussigkeitsgefullter Hohlkorper," Forsch. Geb. Ingenieurwes, **28**, pp. 115–123; 1962, Forsch. Geb. Ingenieurwes, **28**, pp. 147–153.

[20] Ehrich, E. F., 1967, “The Influence of Trapped Fluids on High Speed Rotor Vibration,” *ASME J. Eng. Ind*., **89**, pp. 806–812.

[21] Kirk, R. G., Mondy, M. E., and Murphy, R. C., 1984, “Theory and Guidelines to Proper Coupling Design for Rotor Dynamic Considerations,” *ASME J. Vib. Acoust., Stress, Reliab. Des.*, **106**, pp. 129–138.

[22] Thearle E., 1932, “A New Type of Dynamic-Balancing Machine,” *Trans. ASME* **54**, APM-54-12, pp. 131-141.

[23] Sperling, L., Ryzhik, B. y Duckstein, H., 2001, “Two-Plane Automatic Balancing,” Machine Dynamics Problems, Proceedings of 7th Polish German Workshop on Dynamical Problems in Mechanical Systems, pp. 139-152.

[24] Sperling, L., Ryzhik, B., Linz, C., and Duckstein, H., 2002, “Simulation of Two-Plane Automatic Balancing of a Rigid Rotor”, Mathemathics and Computers in Simulation, **58**, pp. 351-365.

[25] Green, K., Champneys, A. R., y Lieven N. J., 2006, ”Bifurcation Analysis of an Automatic Dynamic Balancing Mechanism for Eccentric Rotors,” *Journal of Sound and Vibration*, **291**, pp. 861-881.

[26] Green, K., Champneys, A. R., y Friswell M. I., 2006, “Analysis of the Transient Response of an Automatic Dynamic Balancer for Eccentric Rotors,” International *Journal of Mechanical Sciences*, **48**, pp. 274-293.

[27] Horvath, R., Flowers, G., Fausz, J., 2006, “Passive Balancing for Rotor Systems,” Ph.D. thesis, Auburn University, Alabama.

[28] Tatsumi, H., and Ito, M., 1984, "Balancer For Use in Centrifugal Rotary Machine," US Patent 4,433,592.

[29] Lee, J. Y., 1998, "Equilibrador de Esfera para Máquina de Lavar," República Federativa de Brasil, PI9703376-6A.

[30] Southworth, D.W. , 2003, "Dynamic Balancer for An Automatic Washer," US Patent 6,658,902 B2.

[31] Kim, J.-S., 1998, "Balancing Device for Drum Washing Machine," US Patent 5,802,885.

[32] Adrian, R. J., 2005, "Twenty Years of Particle Image Velocimetry," *Journal of Experiments in Fluids*, **39 (2)**, pp. 159-169.

[33] Urbiola-Soto, L., Lopez-Parra, M., 2010, "Experimental and Analytical Investigation on a Liquid Balance Ring for Automatic Washing Machines", Proceedings of the ASME 2010 10th Biennial Conference on Engineering Systems Design and Analysis (ESDA 2010), Istanbul, Turkey, July 12-14.

[34] Ehrich, F., and Childs, D., 1984, "Identification and Avoidance of Instabilities in High Performance Turbomachinery," *Mechanical Engineering*, pp. 66-79.

[35] Miles, J. W., and Troesch, B. A., 1961, "Surface Oscillations of a Rotating Liquid," *Journal of Applied Mechanics*, **28**, pp. 491–496.

[36] Timoshenko, S., Young, D. H., and Weaver, W. Jr., 1974, "Vibrations Problems in Engineering," *John Wiley & Sons*.

[37] Urbiola-Soto, L., and Lopez-Parra, M., 2011, "Dynamic Performance Of The LeBlanc Balancer For Automatic Washing Machines," ASME Journal of Vibration and Acoustics, 133-4 (2011).

[38]. Urbiola-Soto, L., and Lopez-Parra, M., 2011, "Stability of Flexible Rotors with a LeBlanc Balancer," ASME paper GT2011-46848, *Proceedings of AME Turbo Expo 2011*, Vancouver, Canada, June 6-10.

[39] Barret, L. E., Gunter, E. J., and Allaire, P. E., 1978, "Optimum Bearing and Support Damping for Unbalance Response and Stability of Rotating Machinery," *ASME Journal of Engineering for Power*, **2**, pp. 89-94.

[40] Childs, D., 1993, "Turbomachinery Rotordynamics: Phenomena, Modeling, and Analysis," John Wiley and Sons, New York, pp. 432-434.

[41] Greenberg, M. D., 1998, "Advanced Engineering Mathematics," Prentice Hall, Second Edition, pp. 86-88.

[42] Riley, William F., and Sturges, Leroy D., 1993, "Engineering Mechanics, Dynamics," John Wiley & Sons, Inc., pp. 105-109.

[43] Urbiola, L., et. al., 2011, "Balance Ring System on Two Planes for a Spin Rotary Machine," US Patent and Trademark Office Application 2011/0048081 A1.

[44] European Parliament and Council, "Directive on the restriction of the use of certain hazardous substances in electrical and electronic equipment 2002/95/EC," Official Journal L37, 13 February 2003, pp.19–23.

APPENDIX A

DERIVATION OF DISTANCE FROM FLUID C.G. TO POINTS C AND O

Assuming the fluid center of gravity **F** to be coincident with its centroid, the distance of the former to **C** is obtained according to

$$d = \frac{\Sigma C_n A_n}{\Sigma A_n} = \frac{(0)\pi \mathrm{r}_o^2 - (-z)\pi \mathrm{r}_f^2}{\pi(\mathrm{r}_o^2 - \mathrm{r}_f^2)} = z\frac{\mathrm{r}_f^2}{\mathrm{r}_o^2 - \mathrm{r}_f^2}$$

Where n stands for the n-esim area A_n which centroid is at a distance C_n to the point **C**. Similarly, the distance of the fluid center of gravity to **O** is given by

$$\bar{z} = \frac{\Sigma C_n A_n}{\Sigma A_n} = \frac{z_i \pi \mathrm{r}_o^2 - (0)\pi \mathrm{r}_f^2}{\pi(\mathrm{r}_o^2 - \mathrm{r}_f^2)} = z\frac{\mathrm{r}_o^2}{\mathrm{r}_o^2 - \mathrm{r}_f^2}$$

Note that by employing d and $\bar{z}$ as expressed above, Eqs. (33) and (43) are put in terms solely of z and its derivatives, such that easily solvable second order ordinary linear differential equations with constant coefficients are obtained. The terms d and $\bar{z}$ are further useful substitution to simplify both, the unbalance response solution shown in Eqs. (21, 27, 34, and 36), and the characteristic polynomial stated in Eq. (46).

APPENDIX B

SIMPLIFICATION OF EQUATION OF MOTION

The differential equations of motion of a Jeffcott rotor mounted on symmetric flexible bearings are given by Eqs. (3) and (4).

Dividing Eq. (31) by m_r and since $\omega_{cr}^2 = k_r/m_r$

$$\ddot{\boldsymbol{z}} + \omega_{cr}^2\left(\boldsymbol{z} - \boldsymbol{z}_1\right) + \mathrm{M}\bar{\boldsymbol{z}}\omega^2 + 2\mathrm{M}_b\dot{\boldsymbol{d}}\omega = u_e\omega^2 e^{j\omega t} \tag{B1}$$

Similarly, Eq. (32) renders Eq. (B2).

$$\frac{k_1}{m_r}\boldsymbol{z}_1 + \omega_{cr}^2\left(\boldsymbol{z}_1 - \boldsymbol{z}\right) + \frac{c_1}{m_r}\dot{\boldsymbol{z}}_1 = 0 \tag{B2}$$

Since $\mathrm{K} = k_1/k_r$ and $\xi_1 = c_1/2m_r\omega_{cr}$

$$2\omega_{cr}\xi_1\dot{\boldsymbol{z}}_1 + \mathrm{K}\omega_{cr}^2\boldsymbol{z}_1 + \omega_{cr}^2\left(\boldsymbol{z}_1 - \boldsymbol{z}\right) = 0$$

Assuming particular function solutions of the form $\boldsymbol{z} = ze^{j\omega t}$ and $\boldsymbol{z}_1 = z_1e^{j\omega t}$ and dividing by ω_{cr}^2

$$2j\xi_1 z_1 \mathrm{f} + \mathrm{K}z_1 + z_1 - z = 0$$

Rearranging and solving for $\boldsymbol{z}_1$ in terms of $\boldsymbol{z}$.

$$z_1 = \frac{z}{\left[\mathrm{K} + 1 + 2j\xi_1 \mathrm{f}\right]}$$

Multiplying by the complex conjugate in the numerator and denominator

$$z_1 = z\frac{\mathrm{K} + 1 - 2j\xi_1 \mathrm{f}}{(\mathrm{K}+1)^2 + (2\xi_1 \mathrm{f})^2}$$

Let $\mathrm{D} = (\mathrm{K}+1)^2 + (2\xi_1 \mathrm{f})^2$, then

$$\boldsymbol{z}_1 = \frac{\mathrm{K}+1}{\mathrm{D}}\boldsymbol{z} - \frac{2\xi_1}{\mathrm{D}\omega_{cr}}\dot{\boldsymbol{z}} \tag{B3}$$

Substitution of Eq. (B3) into Eq. (B1) delivers

$$\ddot{\boldsymbol{z}} + \omega_{cr}^2\left[\boldsymbol{z} - \frac{\mathrm{K}+1}{\mathrm{D}}\boldsymbol{z} + \frac{2\xi_1}{\mathrm{D}\omega_{cr}}\dot{\boldsymbol{z}}\right] + \mathrm{M}\bar{\boldsymbol{z}}\omega^2 + 2\mathrm{M}_b\dot{\boldsymbol{d}}\omega = u\omega^2 e^{j\omega t}$$

$$\ddot{\boldsymbol{z}} + 2\omega_{cr}\frac{\xi_1}{\mathrm{D}}\dot{\boldsymbol{z}} + \omega_{cr}^2\left[1 - \frac{\mathrm{K}+1}{\mathrm{D}}\right]\boldsymbol{z} + \mathrm{M}\bar{\boldsymbol{z}}\omega^2 + 2\mathrm{M}_b\dot{\boldsymbol{d}}\omega^2 = u\omega^2 e^{j\omega t}$$

Which with further algebraic manipulation reduces to

$$\ddot{\boldsymbol{z}} + 2\omega_{cr}\xi_e\dot{\boldsymbol{z}} + 2\mathrm{M}_b\dot{\boldsymbol{d}}\omega + \Omega^2\boldsymbol{z} + \mathrm{M}\bar{\boldsymbol{z}}\omega^2 = u\omega^2 e^{j\omega t}$$

The latest has the form of Eq. (33)

APPENDIX C

INTERNAL FRICTION DAMPING MECHANISM

Figure C1 is taken from Harris C.M., and Piersol, A.G, "Harris' Shock And Vibration Handbook,"5th ed., McGraw-Hill, 2002:

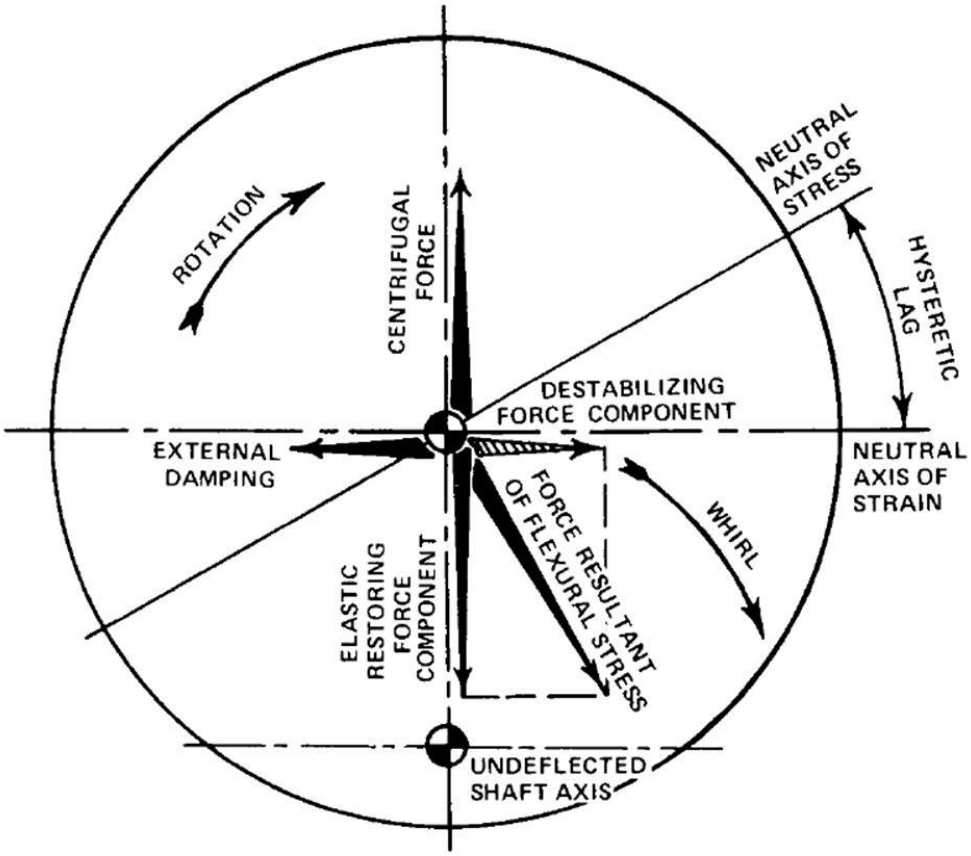

Figure C1. Internal friction damping.

With some nominal radial deflection of the shaft, the flexure of the shaft would induce a neutral strain axis normal to the deflection direction. From first-order

considerations of elastic-beam theory, the neutral axis of stress would be coincident with the neutral axis of strain. The net elastic restoring force would then be perpendicular to the neutral stress axis, i.e., parallel to and opposing the deflection. In actual fact, hysteresis, or internal friction, in the rotating shaft will cause a phase shift in the development of stress as the shaft fibers rotate around through peak strain to the neutral strain axis. The net effect is that the neutral stress axis is displaced in angle orientation from the neutral strain axis, and the resultant force is not parallel to the deflection. In particular, the resultant force has a tangential component *normal to the* deflection, which is the fundamental precondition for whirl. This tangential force component is in the direction of rotation and induces a *forward whirling motion* which increases centrifugal force on the deflected rotor, thereby increasing its deflection. As a consequence, induced stresses are increased, thereby increasing the whirl inducing force component.

Figures C3-C5 provide and explanation of the subsynchronous whirl phenomenon and the internal friction damping mechanisms in shafts and shrink-fit rotor assemblies.

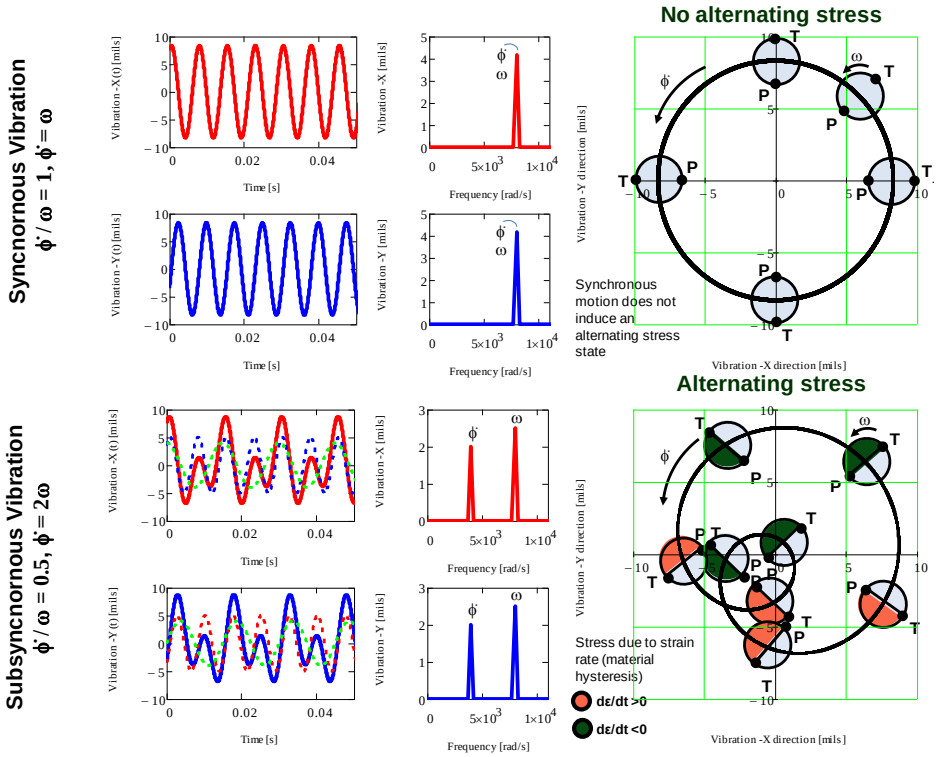

Figure C2. Non-alternating stress vs alternating stress in a shaft.

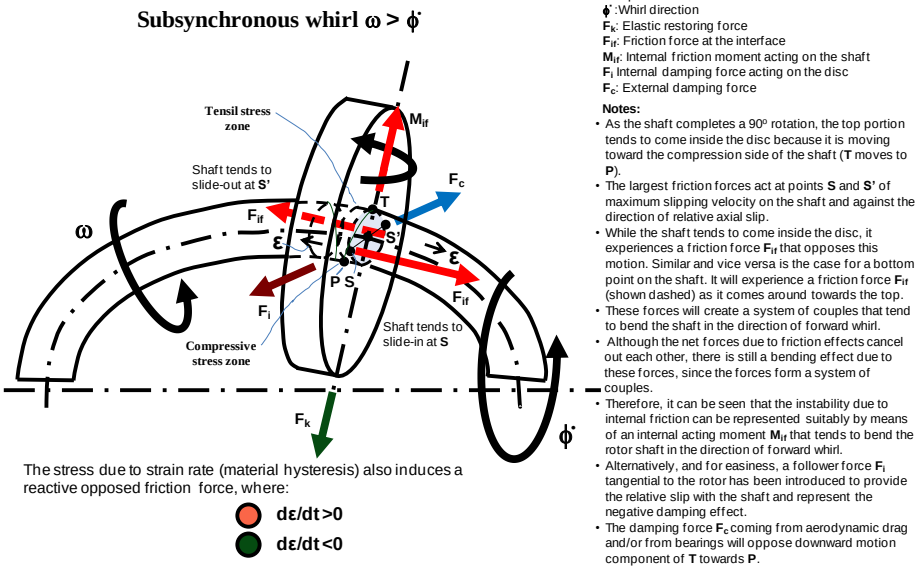

Figure C3. Negative damping in a shrink-fit rotor assembly.

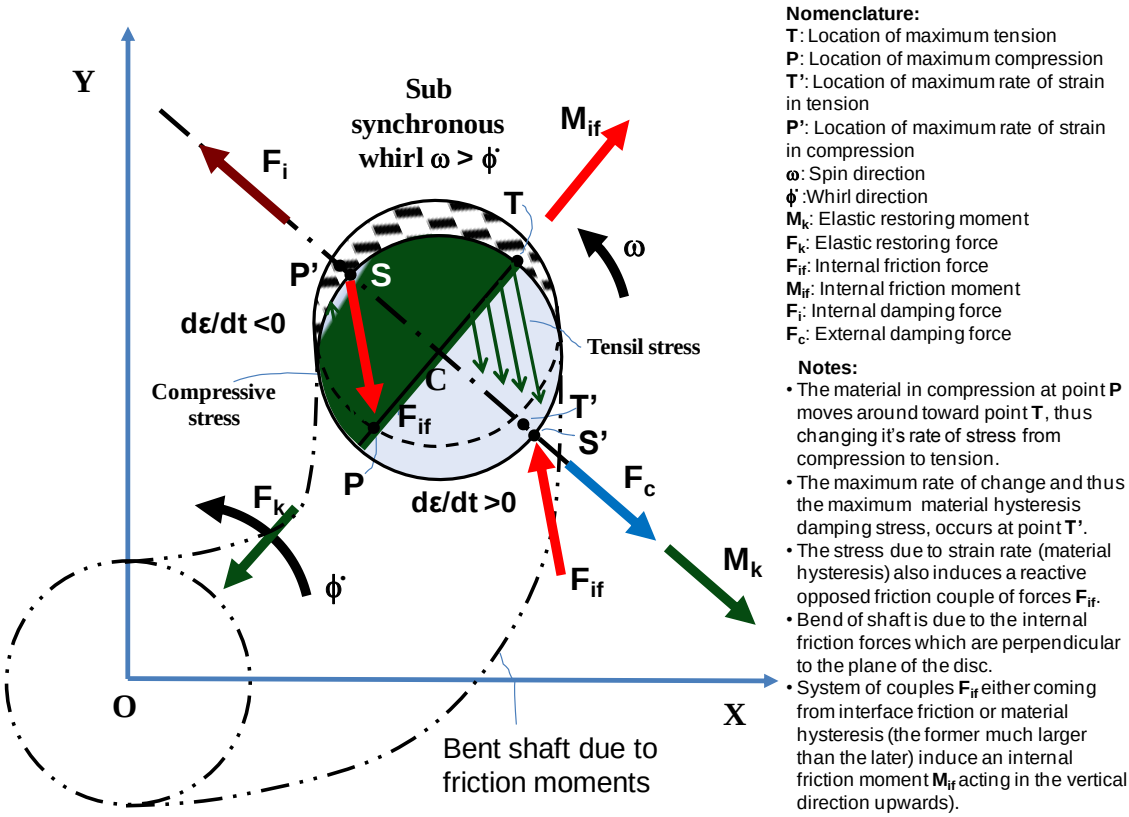

Nomenclature:
T: Location of maximum tension
P: Location of maximum compression
T': Location of maximum rate of strain in tension
P': Location of maximum rate of strain in compression
ω: Spin direction
ϕ̇ :Whirl direction
M_k: Elastic restoring moment
F_k: Elastic restoring force
F_{if}: Internal friction force
M_{if}: Internal friction moment
F_i: Internal damping force
F_c: External damping force

Notes:
- The material in compression at point **P** moves around toward point **T**, thus changing it's rate of stress from compression to tension.
- The maximum rate of change and thus the maximum material hysteresis damping stress, occurs at point **T'**.
- The stress due to strain rate (material hysteresis) also induces a reactive opposed friction couple of forces F_{if}.
- Bend of shaft is due to the internal friction forces which are perpendicular to the plane of the disc.
- System of couples F_{if} either coming from interface friction or material hysteresis (the former much larger than the later) induce an internal friction moment M_{if} acting in the vertical direction upwards).

Figure C4. Negative hysteretic shaft damping.

APPENDIX D

BACKWARD BLADE ANALYSIS

In terms of the rotating coordinate system, the differential equation of motion in terms of the relative position angle θ on Fig. 40 is given by [39]

$$\mathbf{a}_{\mathrm{P}} = \mathbf{a}_{\mathrm{O'}} + \dot{\boldsymbol{\omega}} \times \mathbf{r}_{\mathrm{P/O'}} + \boldsymbol{\omega} \times (\boldsymbol{\omega} \times \mathbf{r}_{\mathrm{P/O'}}) + \mathbf{a}_{\mathrm{P\,rel}} + 2\boldsymbol{\omega} \times \mathbf{v}_{\mathrm{P\,rel}} \tag{D1}$$

Where $\mathbf{a}_{\mathrm{O'}}$, $\mathbf{a}_{\mathrm{P}}$, $\boldsymbol{\omega}$, and $\dot{\boldsymbol{\omega}}$ are all measured relative to the fixed *R*-Θ coordinate system; $\mathbf{r}_{\mathrm{P/O'}}$, $\mathbf{v}_{\mathrm{Prel}}$, and $\mathbf{a}_{\mathrm{Prel}}$ are measured relative to the rotating *r*-θ coordinate system. The vectors in Eq. (70) must be expressed in a common reference system before the vectors sums and products can be performed. The acceleration of **O'** in the *R*-Θ coordinate system is described by

$$\mathbf{a}_{\mathrm{O'}} = (\mathbf{a}_{\mathrm{O'}})_R + (\mathbf{a}_{\mathrm{O'}})_\Theta = \mathrm{r}_o\omega^2\hat{e}_R + \mathrm{r}_o\dot{\omega}\hat{e}_\Theta \tag{D2}$$

Translating $\mathbf{a}_{\mathrm{O'}}$ to the rotating coordinate system *r*-θ in accordance with Fig. 41(a), and knowing that $\dot{\omega} \neq 0$ at the machine start-up

$$\mathbf{a}_{\mathrm{O'}} = \mathrm{r}_o\omega^2(\cos\theta\hat{e}_r - \sin\theta\hat{e}_\theta) + \mathrm{r}_o\dot{\omega}(\sin\theta\hat{e}_r + \cos\theta\hat{e}_\theta) \tag{D3}$$

Also

$$\dot{\boldsymbol{\omega}} \times \mathbf{r}_{P/O'} = -\dot{\omega}\hat{e}_k \times r_p \hat{e}_r = -r_p \dot{\omega}\hat{e}_\theta \tag{D4}$$

Now the third term of Eq. (D1) is

$$\boldsymbol{\omega} \times (\boldsymbol{\omega} \times \mathbf{r}_{P/O'}) = -\omega\hat{e}_k \times (-\omega\hat{e}_k \times r_p \hat{e}_r)$$

$$\boldsymbol{\omega} \times (\boldsymbol{\omega} \times \mathbf{r}_{P/O'}) = -\omega\hat{e}_k \times (-r_p \omega\hat{e}_\theta)$$

$$\boldsymbol{\omega} \times (\boldsymbol{\omega} \times \mathbf{r}_{P/O'}) = -r_p \omega^2 \hat{e}_r \tag{D5}$$

The relative velocity and acceleration are defined as

$$\mathbf{a}_{P\,rel} = (\mathbf{a}_P)_r + (\mathbf{a}_P)_\theta = -r_p \dot{\theta}^2 \hat{e}_r + r_p \ddot{\theta}\hat{e}_\theta \tag{D6}$$

$$\mathbf{v}_{P\,rel} = \dot{r}_p \hat{e}_r + r_p \dot{\theta}\hat{e}_\theta \tag{D7}$$

So the fifth term of Eq. (D1) is

$$2\boldsymbol{\omega} \times \mathbf{v}_{P\,rel} = -2\omega\hat{e}_k \times (\dot{r}_p \hat{e}_r + r_p \dot{\theta}\hat{e}_\theta)$$

$$2\boldsymbol{\omega} \times \mathbf{v}_{P\,rel} = -2\dot{r}_p \omega\hat{e}_\theta - 2r_p \omega\dot{\theta}\hat{e}_r \tag{D8}$$

Substituting Eqs. (D3-D6) and Eq. (D8) into Eq. (D2) renders

$$\mathbf{a}_P = (r_o\omega^2\cos\theta - r_p\omega^2 - r_p\dot{\theta}^2 - 2r_p\omega\dot{\theta} + r_o\dot{\omega}\sin\theta)\hat{e}_r$$
$$+(r_p\ddot{\theta} - r_o\omega^2\sin\theta + 2\dot{r}_p\omega - r_p\dot{\omega} + r_o\dot{\omega}\cos\theta)\hat{e}_\theta \qquad \text{(D9)}$$

Since there is no force in the $\boldsymbol{e}_\theta$-direction $(\mathbf{a}_P)_\theta = 0$. Hence

$$r_p\ddot{\theta} - r_o\omega^2\sin\theta + 2\dot{r}_p\omega - r_p\dot{\omega} + r_o\dot{\omega}\cos\theta = 0$$

$$\ddot{\theta} = \frac{r_o}{r_p}\omega^2\sin\theta - 2\frac{\dot{r}_p}{r_p}\omega r_p + \dot{\omega} - \frac{r_o}{r_p}\dot{\omega}\cos\theta \qquad \text{(D10)}$$

Inspection of Fig. 41(b) lets state that at t = 0; θ_i = atan(r_i / r_o), r = r_i, and $\dot{\theta}(\theta_i) = 0$. Given that the angular acceleration is known as a function of angular position instead of time, then using the chain rule of differentiation delivers

$$\ddot{\theta}(\theta) = \frac{d\dot{\theta}}{dt} = \frac{d\dot{\theta}}{d\theta}\frac{d\theta}{dt} = \dot{\theta}\frac{d\dot{\theta}}{d\theta}$$

Then, Eq. (D10) becomes

$$\ddot{\theta} = \dot{\theta}\frac{d\dot{\theta}}{d\theta} = \frac{r_o}{r_p}\omega^2\sin\theta - 2\frac{\dot{r}_p}{r_p}\omega + \dot{\omega} - \frac{r_o}{r_p}\dot{\omega}\cos\theta$$

Integrating between boundary conditions

$$\int_0^{\dot{\theta}} \dot{\theta} d\dot{\theta} = \int_{\theta_i}^{\theta} \left[\frac{r_o}{r_p} \omega^2 \sin\theta - 2\frac{\dot{r}_p}{r_p}\omega + \dot{\omega} - \frac{r_o}{r_p}\dot{\omega}\cos\theta \right] d\theta$$

$$\frac{1}{2}\dot{\theta}^2 = \frac{r_o}{r_p}\omega^2\left(\cos\theta_i - \cos\theta\right) - 2\frac{\dot{r}_p}{r_p}\omega\left(\theta_i - \theta\right) + \dot{\omega}\left(\theta_i - \theta\right) - \frac{r_o}{r_p}\dot{\omega}\left(\sin\theta_i - \sin\theta\right)$$

$$\cos\theta = \cos\theta_i - \frac{r_p}{r_o\omega^2}\left\{ \frac{1}{2}\dot{\theta}^2 + \left[2\omega\frac{\dot{r}_p}{r_p} - \dot{\omega} \right]\left(\theta_i - \theta\right) + \frac{r_o}{r_p}\dot{\omega}\left(\sin\theta_i - \sin\theta\right) \right\}$$

But

$$\cos\theta_i = \cos\left(\operatorname{atan}\frac{r_i}{r_o} \right) = \left(\left(\frac{r_i}{r_o} \right)^2 + 1 \right)^{-0.5}$$

Then

$$\cos\theta = \left[\left(\frac{r_i}{r_o} \right)^2 + 1 \right]^{-0.5} - \frac{r_p}{r_o\omega^2}\left\{ \frac{1}{2}\dot{\theta}^2 + \left[2\omega\frac{\dot{r}_p}{r_p} - \dot{\omega} \right]\left(\theta_i - \theta\right) + \frac{r_o}{r_p}\dot{\omega}\left(\sin\theta_i - \sin\theta\right) \right\}$$

On the other hand, the force F_{bw} of the particle **P** of mass m_p impelled by a backward blade is

$$\mathbf{F}_{bw} = F_r \hat{e}_r = m_p \mathbf{a}_r$$

Taking $\mathbf{a}_r$ from Eq. (D9)

$$F_{fw} = m_p a_r = m_p\left[r_o\omega^2\cos\theta - r_p\omega^2 - r_p\dot{\theta}^2 - 2r_p\omega\dot{\theta} + r_o\dot{\omega}\sin\theta \right]$$

At $\theta = \theta_i$; $r_p = r_{pi}$, $\dot{\theta} = 0$, and $\dot{\omega} = \ddot{\Theta}$, then

$$\cos\theta_i = \left[\left(\frac{r_i}{r_o}\right)^2 + 1\right]^{-0.5} \tag{D11}$$

which leads back to the trigonometric identity, confirming that the initial conditions are well established

On the other hand, at $\theta = \theta_o$; $r_p = r_{po}$, $\dot{\theta} = \omega$, $\dot{\omega} = \ddot{\Theta}$, and $\dot{r}_p = \dot{r}_{po}$. Consequently

$$\cos\theta_o = \left[\left(\frac{r_i}{r_o}\right)^2 + 1\right]^{-0.5} - \left\{\frac{r_{po}}{2r_o} + \left[\frac{2\dot{r}_{po}}{r_o\omega} - \frac{r_{po}}{r_o\omega^2}\ddot{\Theta}\right](\theta_i - \theta_o) + \frac{\ddot{\Theta}}{\omega^2}(\sin\theta_i - \sin\theta_o)\right\} \tag{D12}$$

Also, from trigonometric identities

$$\sin\theta_i = \sin\left(\operatorname{atan}\frac{r_i}{r_o}\right) = \frac{r_i}{r_o}\left(\left(\frac{r_i}{r_o}\right)^2 + 1\right)^{-0.5}$$

Therefore

$$F_{bwi} = m_p a_{ri} = m_p\left[\left(\frac{r_i}{r_o}\right)^2 + 1\right]^{-0.5}\left(r_o\omega^2 + r_i\dot{\omega}\right) \tag{D13}$$

$$F_{bwo} = m_p a_{ro} = m_p \left\{ r_o \omega^2 \left[\left[\left(\frac{r_i}{r_o} \right)^2 + 1 \right]^{-0.5} - \left[\frac{r_{po}}{2r_o} + \left(\frac{2\dot{r}_{po}}{r_o \omega} + \frac{r_{po}}{r_o \omega^2} \ddot{\Theta} \right) (\theta_i - \theta_o) \right. \right. \right. \quad \text{(D14)}$$

$$\left. \left. \left. + \frac{\ddot{\Theta}}{\omega^2} (\sin\theta_i - \sin\theta_o) \right] \right]^2 + r_o \ddot{\Theta} \sin\theta_o \right\}$$

Using Fig. 41(b), r_{pi} is easily obtained from Pythagoras theorem, whereas r_{po} is obtained by the law of cosines as follows

$$r_{pi} = \left(r_o^2 - r_i^2 \right)^{0.5} = \left[(0.259\ \text{m})^2 - (0.215\ \text{m})^2 \right]^{0.5} = 0.337\ \text{m} \quad \text{(D15)}$$

$$r_{po} = \left[2r_o^2 - 2r_o^2 \cos\left(\frac{\pi}{2} - \Theta_o \right) \right]^{0.5} = \left[2(0.259\ \text{m})^2 - 2(0.259\ \text{m})^2 \cos\left(\frac{\pi}{2} - 0.36 \right) \right]^{0.5}$$

$$r_{po} = \left[2r_o^2 - 2r_o^2 \cos\left(\frac{\pi}{2} - \Theta_o \right) \right]^{0.5} = 0.235\ \text{m} \quad \text{(D16)}$$

Also, the θ_i and θ_o can be computed as

$$\theta_i = \text{atan}\left(\frac{r_i}{r_o} \right) = 0.693\ \text{rad} = 39.7\ \text{deg} \quad \text{(D17)}$$

$$\theta_o = \text{acos}\left(\frac{r_p^2}{2 r_o r_{po}} \right) = 1.1\ \text{rad} = 63\ \text{deg} \quad \text{(D18)}$$

According to Fig. 42, the absolute velocity vectors in the *R*-Θ coordinate system are related by $\dot{r} = \dot{\mathbf{r}}_{O'} + \dot{\mathbf{r}}_{P/O'}$ .Then, at $\theta = \theta_o$; $\dot{\boldsymbol{r}}_o = \dot{\mathbf{r}}_{O'} + \dot{\mathbf{r}}_{po}$, knowing that $\dot{r}_{O'} = 0$, then $\dot{\boldsymbol{r}}_o$ $\dot{\mathbf{r}}_{po} = \dot{\boldsymbol{r}}_o$ when the particle reaches the outer ring wall.

The velocity of the particle **P** at θ_o can be calculated according to Eq. (59) delivering

$$\dot{r}_{\boldsymbol{po}} = r_i \omega \sinh(0) = 0.215 \text{ m} \times 70.162 \text{ rad/s} \times \sinh(0.63) = 10.14 \text{ m/s} \qquad \text{(D19)}$$

Substituting Eq. (84) into Eq. (82) yields the particle force at the beginning of its motion

$$F_{fwi} = 984 \text{ m/s}^2 \text{ m}_p \qquad \text{(D20)}$$

Also, substituting Eqs. (D16-D19) into Eq. (D14) delivers the particle force when it reaches r_o as Eq. (D21)

$$F_{fwo} = 982 \text{ m/s}^2 \text{ m}_p \qquad \text{(D21)}$$